

**Forschungsbericht 2026-10**

# **Experimental Investigation on Primary and Secondary Vortices in the Wake of a Hovering Rotor**

Alexander Heintz

Deutsches Zentrum für Luft- und Raumfahrt  
Institut für Aerodynamik und  
Strömungstechnik  
Göttingen



DLR

Deutsches Zentrum  
für Luft- und Raumfahrt

# **Forschungsbericht 2026-10**

## **Experimental Investigation on Primary and Secondary Vortices in the Wake of a Hovering Rotor**

Alexander Heintz

Deutsches Zentrum für Luft- und Raumfahrt  
Institut für Aerodynamik und  
Strömungstechnik  
Göttingen

141 Seiten  
65 Bilder  
10 Tabellen  
143 Literaturstellen



DLR Deutsches Zentrum  
für Luft- und Raumfahrt



*Herausgeber:*

Deutsches Zentrum  
für Luft- und Raumfahrt e. V.  
Wissenschaftliche Information  
Linder Höhe  
D-51147 Köln

ISSN 1434-8454  
ISRN DLR-FB-2026-10  
Erscheinungsjahr 2026  
DOI: [10.57676/m1qx-5726](https://doi.org/10.57676/m1qx-5726)

### **Erklärung des Herausgebers**

Dieses Werk – ausgenommen anderweitig gekennzeichnete Teile – ist lizenziert unter den Bedingungen der Creative Commons Lizenz vom Typ Namensnennung 4.0 International (CC BY 4.0), abrufbar über <https://creativecommons.org/licenses/by/4.0/legalcode>

### **Lizenz**



Creative Commons Attribution 4.0 International

Alexander HEINTZ

DLR, Institut für Aerodynamik und Strömungstechnik, Göttingen

***Experimentelle Untersuchung an primären und sekundären Blattspitzenwirbeln im Nachlauf eines Rotors im Schwebeflug***

Dissertation, Leibniz Universität Hannover

Die Blattspitzenwirbel von Drehflüglern haben einen erheblichen Einfluss auf die Aerodynamik des Rotornachlaufes und stellen die Konstruktion von Drehflüglern vor Herausforderungen. Sie tragen zur Lärmemission bei, wenn ein Rotorblatt mit einem Wirbel interagiert. Solche Blatt-Wirbel-Interaktionen (BVI) führen zudem zu instationären Belastungen der Rotorblätter, wodurch sich Vibrationen ergeben. Darüber hinaus können Fragmente zerfallener Wirbel beim Start und bei der Landung starke Geschwindigkeitsschwankungen in der Umgebung erzeugen, was eine potenzielle Gefährdung für das Bodenpersonal darstellt.

Aufgrund der Komplexität dieser Strömungsfelder bleibt die numerische Simulation, insbesondere im Schwebeflug, anspruchsvoll. Jüngste Simulationen haben zusätzliche S-förmige Wirbelstrukturen zwischen den Blattspitzenwirbeln identifiziert, deren Existenz inzwischen durch mehrere Experimente für ausgewählte Konfigurationen bestätigt wurde. Um ihren Einfluss auf den Wirbelzerfall weiter zu bewerten, ist eine umfassende experimentelle Validierung unerlässlich.

Eine grundlegende Voraussetzung für das Verständnis der Sekundärwirbeldynamik ist die zuverlässige Charakterisierung der Primärwirbel. Zu diesem Zweck wurden vier Konfigurationen mithilfe hochauflösender PIV-Messungen an primären Wirbeln untersucht und die Ergebnisse mit analytischen Wirbelmodellen verglichen. Neben der räumlichen Auflösung zeichnen sich die Messungen durch ein maximales erfasstes Wirbelalter von bis zu  $2000^\circ$  aus, welches in der Literatur nur selten untersucht wurde und somit eine wertvolle Datenbasis für die Validierung von Wirbelmodellen und numerischen Simulationen bietet.

Es wird gezeigt, dass das laminare Lamb-Oseen Wirbelmodell in der Lage ist, die maximale Tangentialgeschwindigkeit in den untersuchten Fällen genau vorherzusagen und dass ein leicht erweitertes Anathan-Leishman Modell auch die Entwicklung der Wirbelkernradien erfasst. Allerdings hängt die Gesamtgeschwindigkeitsverteilung stark von der Nachlaufschicht ab, wodurch sich die Genauigkeit bei größeren radialen Abständen verringert. In einem Fallbeispiel wird ein möglicher Einfluss des Nachlaufes demonstriert: Die Zerlegung des Geschwindigkeitsfeldes in das mittlere und das momentane Strömungsfeld verbessert die Übereinstimmung mit dem Lamb-Oseen Modell erheblich.

Der Einfluss der Sekundärwirbel auf den gesamten Wirbelzerfall wurde in mehr als 30 verschiedenen Konfigurationen untersucht. Die Ergebnisse zeigen, dass sowohl die spezifische Blattbelastung als auch die Blattfolgefrequenz (BPF) die Entstehung von Sekundärwirbeln beeinflussen. Während der Einfluss der spezifischen Blattbelastung vergleichsweise gering ist, erweist sich die BPF als der dominante Einflussfaktor. Es wird eine nahezu lineare Abhängigkeit der Anzahl der Sekundärwirbel und der Zirkulation von der BPF beobachtet, und dieser Trend wird auch von den verfügbaren CFD-Daten reproduziert. Allerdings lässt sich weder in den CFD-Ergebnissen noch in den Experimenten ein direkter Zusammenhang zwischen dem Auftreten von Sekundärwirbeln und dem Zerfall oder der Interaktion mit den Primärwirbeln feststellen.

Alexander HEINTZ

German Aerospace Center (DLR), Institute of Aerodynamics and Flow Technology, Göttingen

***Experimental Investigation on Primary and Secondary Vortices in the Wake of a Hovering Rotor***

Dissertation, Leibniz University Hanover

The blade tip vortices of rotorcraft strongly influence the aerodynamics of the rotor wake and pose several challenges for rotorcraft design. They contribute to noise emission when a blade interacts with a vortex, these interactions generate noise and induce unsteady loads on the rotor blades, resulting in vibrations. In addition, fragments of decayed vortices can generate strong velocity fluctuations near rotorcraft during takeoff and landing, representing a potential hazard for personnel in the immediate vicinity.

Due to the complexity of these flow fields, numerical simulation remains challenging, particularly in hover. Recent simulations have revealed additional S-shaped vortex structures in between the blade tip vortices. Their existence was subsequently confirmed by several experiments for sample cases. To further assess their influence on vortex decay, comprehensive experimental validation is essential.

A prerequisite for understanding secondary vortex dynamics is a robust characterization of the primary vortices. To this end, four configurations were investigated using high-resolution PIV on primary vortices, and their results are employed to benchmark analytical vortex models. Beyond its spatial resolution, the maximum vortex age of up to  $2000^\circ$  is rarely reported in literature and provides a valuable database for the validation of vortex models and numerical simulations.

It is shown that the laminar Lamb-Oseen vortex model is able to accurately predict maximum swirl velocity and that a slightly extended Ananthan-Leishman model also captures the development of vortex core radii. However, the overall velocity distribution is strongly influenced by the wake shear layer, reducing the accuracy at a larger radial distance. In one sample case a potential influence of wake shear layer is demonstrated: decomposing the velocity field into the mean slipstream and the instantaneous flow field, improves the agreement with the Lamb-Oseen model significantly.

The influence of secondary vortices on the overall blade tip vortex decay was investigated in more than 30 different configurations. The results demonstrate that the blade loading and the blade passing frequency (BPF) both affect secondary vortex emergence. While the effect of blade loading remains rather small, the BPF emerges as the key influencing factor. A nearly linear dependence of secondary vortex number and circulation on BPF is observed, and this trend is also reproduced by the available CFD data. However, no direct correlation between secondary vortex occurrence and primary blade tip vortex decay or interaction is found in either the CFD results or the experiments.

# **Experimental Investigation on Primary and Secondary Vortices in the Wake of a Hovering Rotor**

Von der Fakultät für Maschinenbau  
der Gottfried Wilhelm Leibniz Universität Hannover  
zur Erlangung des akademischen Grades  
Doktor-Ingenieur  
Dr.-Ing.  
genehmigte Dissertation

von  
Alexander Heintz, M.Sc.

2026

Referent: Prof. Dr.-Ing. Markus Raffel  
Korreferent: Prof. Dr. rer. nat. Andreas Schröder

Tag der Promotion: 08.04.2026

# Abstract

The blade tip vortices of rotorcraft strongly influence the aerodynamics of the rotor wake and pose several challenges for rotorcraft design. They contribute to noise emission when a blade interacts with a vortex, these interactions generate noise and induce unsteady loads on the rotor blades, resulting in vibrations. In addition, fragments of decayed vortices can generate strong velocity fluctuations near rotorcraft during takeoff and landing, representing a potential hazard for personnel in the immediate vicinity.

Due to the complexity of these flow fields, numerical simulation remains challenging, particularly in hover. Recent simulations have revealed additional S-shaped vortex structures in between the blade tip vortices. Their existence was subsequently confirmed by several experiments for sample cases. To further assess their influence on vortex decay, comprehensive experimental validation is essential.

A prerequisite for understanding secondary vortex dynamics is a robust characterization of the primary vortices. To this end, four configurations were investigated using high-resolution PIV on primary vortices, and their results are employed to benchmark analytical vortex models. Beyond its spatial resolution, the maximum vortex age of up to  $2000^\circ$  is rarely reported in literature and provides a valuable database for the validation of vortex models and numerical simulations.

It is shown that the laminar Lamb-Oseen vortex model is able to accurately predict maximum swirl velocity and that a slightly extended Ananthan-Leishman model also captures the development of vortex core radii. However, the overall velocity distribution is strongly influenced by the wake shear layer, reducing the accuracy at a larger radial distance. In one sample case a potential influence of wake shear layer is demonstrated: decomposing the velocity field into the mean slipstream and the instantaneous flow field, improves the agreement with the Lamb-Oseen model significantly.

The influence of secondary vortices on the overall blade tip vortex decay was investigated in more than 30 different configurations. The results demonstrate that the blade loading and the blade passing frequency (BPF) both affect secondary vortex emergence. While the effect of blade loading remains rather small, the BPF emerges as the key influencing factor. A nearly linear dependence of secondary vortex number and circulation on BPF is observed, and this trend is also reproduced by the available CFD data. However, no direct correlation between secondary vortex occurrence and primary blade tip vortex decay or interaction is found in either the CFD results or the experiments.

**Keywords:** Blade tip vortices, Rotor aerodynamics, PIV



# Kurzfassung

Die Blattspitzenwirbel von Drehflüglern haben einen erheblichen Einfluss auf die Aerodynamik des Rotornachlaufes und stellen die Konstruktion von Drehflüglern vor Herausforderungen. Sie tragen zur Lärmemission bei, wenn ein Rotorblatt mit einem Wirbel interagiert. Solche Blatt-Wirbel-Interaktionen (BVI) führen zudem zu instationären Belastungen der Rotorblätter, wodurch sich Vibrationen ergeben. Darüber hinaus können Fragmente zerfallener Wirbel beim Start und bei der Landung starke Geschwindigkeitsschwankungen in der Umgebung erzeugen, was eine potenzielle Gefährdung für das Bodenpersonal darstellt.

Aufgrund der Komplexität dieser Strömungsfelder bleibt die numerische Simulation, insbesondere im Schwebeflug, anspruchsvoll. Jüngste Simulationen haben zusätzliche S-förmige Wirbelstrukturen zwischen den Blattspitzenwirbeln identifiziert, deren Existenz inzwischen durch mehrere Experimente für ausgewählte Konfigurationen bestätigt wurde. Um ihren Einfluss auf den Wirbelzerfall weiter zu bewerten, ist eine umfassende experimentelle Validierung unerlässlich.

Eine grundlegende Voraussetzung für das Verständnis der Sekundärwirbeldynamik ist die zuverlässige Charakterisierung der Primärwirbel. Zu diesem Zweck wurden vier Konfigurationen mithilfe hochauflösender PIV-Messungen an primären Wirbeln untersucht und die Ergebnisse mit analytischen Wirbelmodellen verglichen. Neben der räumlichen Auflösung zeichnen sich die Messungen durch ein maximales erfasstes Wirbelalter von bis zu  $2000^\circ$  aus, welches in der Literatur nur selten untersucht wurde und somit eine wertvolle Datenbasis für die Validierung von Wirbelmodellen und numerischen Simulationen bietet.

Es wird gezeigt, dass das laminare Lamb-Oseen Wirbelmodell in der Lage ist, die maximale Tangentialgeschwindigkeit in den untersuchten Fällen genau vorherzusagen und dass ein leicht erweitertes Ananthan-Leishman Modell auch die Entwicklung der Wirbelkernradien erfasst. Allerdings hängt die Gesamtgeschwindigkeitsverteilung stark von der Nachlaufschicht ab, wodurch sich die Genauigkeit bei größeren radialen Abständen verringert. In einem Fallbeispiel wird ein möglicher Einfluss des Nachlaufes demonstriert: Die Zerlegung des Geschwindigkeitsfeldes in das mittlere und das momentane Strömungsfeld verbessert die Übereinstimmung mit dem Lamb-Oseen Modell erheblich.

Der Einfluss der Sekundärwirbel auf den gesamten Wirbelzerfall wurde in mehr als 30 verschiedenen Konfigurationen untersucht. Die Ergebnisse zeigen, dass sowohl die spezifische Blattbelastung als auch die Blattfolgefrequenz (BPF) die Entstehung von Sekundärwirbeln beeinflussen. Während der Einfluss der spezifischen Blattbelastung vergleichsweise gering

ist, erweist sich die BPF als der dominante Einflussfaktor. Es wird eine nahezu lineare Abhängigkeit der Anzahl der Sekundärwirbel und der Zirkulation von der BPF beobachtet, und dieser Trend wird auch von den verfügbaren CFD-Daten reproduziert. Allerdings lässt sich weder in den CFD-Ergebnissen noch in den Experimenten ein direkter Zusammenhang zwischen dem Auftreten von Sekundärwirbeln und dem Zerfall oder der Interaktion mit den Primärwirbeln feststellen.

**Stichwörter:** Blattspitzenwirbel, Rotor aerodynamik, PIV

# Acknowledgements

First, I express my deepest appreciation to my doctoral advisor, Prof. Dr. Markus Raffel, for giving me the opportunity to pursue my doctoral research in his department and for his unconditional support, even in difficult times.

I also want to express my sincere gratitude to Prof. Dr. Andreas Schröder (Brandenburg University of Technology Cottbus-Senftenberg) and Prof. Dr. Matthias Becker (Leibniz University Hanover) for their contribution as members of the dissertation committee.

I am also deeply thankful to the great research group in which I was privileged to work during the past years:

- Dr. habil. C. Christian Wolf, for his continuous supervision, meticulous proofreading of this thesis, and many valuable discussions and support, which provided the best scientific guidance a Ph.D. student could hope for,
- Dr. Clemens Schwarz, for preparing the test stand and for his extensive contributions to the measurements and initial evaluations,
- Hauke T. Bartzsch, for the many fruitful discussions on vortex models, vortex decay, and vortex interactions,
- Dr. habil. Antony D. Gardner, for his outstanding leadership of the team and department and for sharing his extensive knowledge of rotorcraft aerodynamics,
- Dr. Johannes Braukmann, for his scientific advice and contributions to the test stand,
- Dr. Felix Löbke, Dr. Anna Kostek and Julien Schwalbe for their support, many discussions, and for being the best office mates, and
- Markus Krebs and Florian Renneke, for their contribution to the test stand.

Furthermore, I am grateful to our DFG project partners, Prof. Dr. Manuel Keßler and Filippo Gajo from the Institute of Gas Dynamics (University of Stuttgart), for providing the CFD simulations and the many interesting discussions on numerics and experiments.

I would also like to express my deepest gratitude to my mother, Anke, for her invaluable assistance with English grammar.

Last but certainly not least, I would like to express my heartfelt gratitude to thank my wife, Leonie, for her endless love, patience, and support. Her understanding during long working hours, her encouragement in difficult moments, and her ability to keep me grounded and motivated made this work possible.

This research project was funded by the German Research Foundation through the project “Wirbelzerfall im rotierenden System” (Project ID: 490853673)

Parts of this thesis were published in Heintz et al. (2023) and Heintz et al. (2025).

Artificial intelligence namely ChatGPT and DeepL were used to improve grammar, language, and readability of this thesis.

# Publications

- Gajo, F., Heintz, A., Kessler, M.: A Comparison of Numerical and Experimental Data from Wake Decay in Hovering Rotors, CEAS Aeronautical Journal (submitted)
- Longobardo, G., Heintz, A., Braukmann, J., Wolf, C.C., Raddatz, J., Astarita, T., De Gregorio, F., Gardner, A.D. and Raffel, M.: Experimental Investigation of Vortex Ring State for Multicopters, 51<sup>st</sup> European Rotorcraft Forum 2025, Venice, Italy, 2025.
- Willert, C. E., Klinner, J., Heintz, A. and Raffel, M.: High-Speed Schlieren Imaging Using Event-Based Vision Cameras, 21<sup>st</sup> International Symposium on Flow Visualization 2025, Tokyo, Japan, 2025.
- Heintz, A., Schwarz, C., Wolf, C. C., and Raffel, M.: Influence of Configurational and Operational Parameters on the Vortex System of a Rotor, AIAA Journal, Vol. 63, No. 6, 2025, pp. 2412-2427
- Wolf, C. C., Schanz, D., Schwarz, C., Heintz, A., Bosbach, J., Strübing, T. and Schröder, A.: Volumetric Wake Investigation of a Free-Flying Quadcopter Using Shake-The-Box Lagrangian Particle Tracking, Experiments in Fluids, Vol. 65, No. 10, 152, 2024.
- Raffel, M., Heintz, A., Braukmann, J.N. and Wolf, C.C.: In-Line PIV Using a Schlieren System, 21<sup>st</sup> International Symposium on Applications of Laser and Imaging Techniques to Fluid Mechanics, Lisbon, Portugal, 2024.
- Schanz, D., Schröder, A., Bosbach, J., Strübing, T., Wolf, C. C., Schwarz, C. and Heintz, A.: Scanning Lagrangian Particle Tracking to Measure 3D Large Scale Aerodynamics of Quadcopter Flight, 21<sup>st</sup> International Symposium on Applications of Laser and Imaging Techniques to Fluid Mechanics, Lisbon, Portugal, 2024.
- Höschler, C. M., Schanz, D., Wolf, C. C., Heintz, A., Schröder, A., Schwarz, C., Bosbach, J. and Strübing, T.: Three-Dimensional Investigation of Rotor Wakes of a Free-Flying Model Helicopter, Annual Motar Meeting 2024: Measurement and Observation Techniques for Aerospace Research, Göttingen, Germany, 2024.
- Wolf, C. C., Schanz, D., Schwarz, C., Heintz, A., Bosbach, J., Strübing, T. and Schröder, A.: Volumetric Wake Investigation of a Free-Flying Quadcopter Using Shake-The-Box Lagrangian Particle Tracking, 80<sup>th</sup> Annual Forum of the Vertical Flight Society, Montreal, Canada, 2024.

- Heintz, A., Schwarz, C., Wolf, C. C. and Raffel, M.: Influence of Configurational Parameters on the Vortex System of a Rotor in Hover, AIAA Scitech, Orlando, USA, 2024.
- Schanz, D., Schröder, A., Bosbach, J., Strübing, T., Wolf, C. C., Schwarz, C., Heintz, A.: Quadcopter and Helicopter Wakes Measured by Large-Volume and High-Resolution Scanning Lagrangian Particle Tracking, 16<sup>th</sup> International Conference on Fluid Control, Measurements, and Visualization, Beijing, China, 2023.
- Schröder, A., Schanz, D., Bosbach, J., Schwarz, C. and Heintz, A.: The 3D flow around a Quadcopter Drone. Annual Motar Meeting 2023, Meudon, France, 2023
- Heintz, A., Schwarz, C., Wolf, C. C. and Raffel, M.: Analysis of Configurational Parameters on the Vortex System of a Rotor, STAB Workshop, Göttingen, Germany, 2023.
- Heintz, A. and Scholz, P.: Measurements on the Effect of Steps on the Transition of Laminar Boundary Layers, Experiments in Fluids, Vol. 64, No. 4, 76, 2023.

# Contents

<b>Nomenclature</b>	<b>xiii</b>
<b>1. Introduction</b>	<b>1</b>
1.1. State of the Art . . . . .	2
1.2. Thesis Organization . . . . .	4
<b>2. Theory of Blade Tip Vortices</b>	<b>5</b>
2.1. Vortex Fundamentals . . . . .	5
2.2. Blade Tip Vortices . . . . .	9
2.3. Vortex Models . . . . .	10
2.4. Vortex Detection Criteria . . . . .	13
2.5. Vortex Disturbances and Interactions . . . . .	18
2.5.1. Vortex Pairs and Arrays . . . . .	19
2.5.2. Perturbation and Instabilities of Blade Tip Vortices . . . . .	20
2.6. Streamwise Vortices in Non-Helical Vortex Systems . . . . .	21
<b>3. Experimental Setup</b>	<b>25</b>
3.1. Measurement Methods . . . . .	25
3.1.1. Development of Measurement Techniques for Rotor Aerodynamics . . . . .	25
3.1.2. Particle Image Velocimetry (PIV) . . . . .	28
3.2. Hover Test Stand . . . . .	35
3.2.1. Test Rotor and Parameters . . . . .	36
3.2.2. Validation of Thrust Measurements . . . . .	38
3.2.3. PIV Setups . . . . .	39
3.3. Validation and Uncertainty Analysis of the PIV Measurements . . . . .	43
3.3.1. Equipment Related Errors . . . . .	44
3.3.2. Particle Behavior . . . . .	45
3.3.3. Sampling Uncertainty . . . . .	47
3.3.4. Image Processing Errors . . . . .	48
<b>4. Data Processing</b>	<b>51</b>
4.1. Vertical Field of Views . . . . .	51
4.1.1. Overview Vertical PIV . . . . .	52
4.1.2. High-Resolution Vertical PIV . . . . .	58
4.2. Horizontal Field of View . . . . .	64

<b>5. Blade Tip Vortex Measurements</b>	<b>71</b>
5.1. Application of Vortex Models on Measurement Data . . . . .	71
5.2. Application of Vortex Models on the Fluctuating Flow Field . . . . .	80
5.3. Behavior of Vortex Voids . . . . .	83
<b>6. Combined Vortex Investigations</b>	<b>85</b>
6.1. Numerical Methods . . . . .	85
6.2. Configurational Parameter Study . . . . .	86
6.2.1. Influence of the Blade Number . . . . .	86
6.2.2. Influence of the Blade Pitch Offset . . . . .	91
6.2.3. Influence of Vortex Pairing . . . . .	93
6.2.4. Influence of the Blade Loading . . . . .	97
6.2.5. Influence of the Blade Geometry . . . . .	99
6.2.6. Influence of the Blade Passing Frequency . . . . .	102
6.3. Validation of Evaluation Parameters . . . . .	104
<b>7. Conclusions and Outlook</b>	<b>107</b>
<b>A. PIV Parameter Study</b>	<b>111</b>
<b>References</b>	<b>113</b>
<b>Curriculum Vitae</b>	<b>123</b>

# Nomenclature

## Abbreviations

std( <i>a</i> )	Standard deviation
2D2C	Two-dimensional, two-component PIV measurement
BPF	Blade Passing Frequency
CFD	Computational Fluid Dynamics
DDES	Delayed Detached Eddy Simulation
DFG	Deutsche Forschungsgemeinschaft (German Research Foundation)
DLR	Deutsches Zentrum für Luft- und Raumfahrt (German Aerospace Center)
DNS	Direct Numerical Simulation
FFT	Fast Fourier Transformation
FOV	Field of view
IAG	Institute of Aerodynamics and Gas Dynamics, University of Stuttgart
LDV	Laser Doppler Velocimetry
LES	Large Eddy Simulation
NASA	National Aeronautics and Space Administration
PIV	Particle Image Velocimetry
ppp	Particles per pixel
PTV	Particle Tracking Velocimetry
RANS	Reynolds-Averaged Navier-Stokes equations
rms	Root mean square
UPM	Unsteady Panel Method

## Greek Letters

$\alpha_L$	Lamb-Oseen constant	–
$\beta$	Vatistas turbulence parameter	–

$\delta$	Effective diffusion constant for vortex models	–
$\delta_1$	Boundary layer displacement thickness	m
$\varepsilon$	Vortex stretching, $\varepsilon = \frac{\Delta l}{l}$	–
$\varepsilon_{ij}$	Strain tensor component	–
$\Gamma$	Circulation	$\text{m}^2 \text{s}^{-1}$
$\Gamma_b$	Bound circulation	$\text{m}^2 \text{s}^{-1}$
$\Gamma_v$	Vortex circulation	$\text{m}^2 \text{s}^{-1}$
$\lambda$	Wavelength	m
$\lambda_2$	$\lambda_2$ vortex criterion	$\text{s}^{-2}$
$\lambda_{\text{ci}}$	Swirling strength	$\text{s}^{-1}$
$\nu$	Kinematic viscosity	$\text{m}^2 \text{s}^{-1}$
$\Omega$	Angular velocity of the rotor	$\text{s}^{-1}$
$\omega$	Vorticity	$\text{s}^{-1}$
$\Omega$	Vorticity tensor	–
$\omega_z$	Vorticity normal to the $x, y$ -plane	$\text{s}^{-1}$
$\psi$	Rotor azimuth position	°
$\psi_v$	Vortex age	°
$\rho$	Density	$\text{kg m}^{-3}$
$\sigma$	Rotor solidity, $\sigma = N_b c / \pi R$	–
$\sigma_{\text{Gaussian}}$	Standard deviation for the Gaussian filter kernel	–
$\sigma_s$	Standard deviation	–
$\theta$	Blade pitch angle	°
$\Delta\theta$	Blade-to-blade pitch angle offset	°

### Indices

$\infty$	Ambient condition
c	Vortex core
cal	Calibration
CFD	CFD result
Exp.	Experimental result
LS	Light sheet

max	Maximum value
mean	Mean value
min	Minimum value
p	Particle
v	Vortex

### Latin Letters

$a$	Amplitude of the vortex track perturbation	m
$\mathbf{A}$	Velocity gradient tensor	–
$a_1$	Turbulent viscosity constant (vortex models)	–
$a_L$	Lamb constant, usually $\alpha_L = 1.121$	–
$a_n$	Ramasamy-Leishman coefficient	–
$b$	Span width	m
$b_n$	Ramasamy-Leishman coefficient	–
$c$	Blade chord length	m
$c_{\text{tip}}$	Chord length at the blade tip	m
$C_T$	Thrust coefficient, $C_T = T/(\rho\pi\Omega^2 R^4)$	–
$C_T/\sigma$	Blade loading	–
$d$	Diameter	m
$\mathbf{D}$	Particle displacement vector	m
$d_p$	Particle diameter	m
$d_{\text{diff}}$	Diffraction limit	m
$E_{\text{kin}}$	Kinetic energy	$\text{kg m}^2 \text{s}^{-2}$
$E_{\eta,P}$	Confidence bound of parameter P, and confidence level $\eta$	–
$f$	Rotation frequency	Hz
$f_{\#}$	Lens f-number	–
$F_i$	In-plane loss-of-correlation	–
$F_o$	Out-of-plane loss-of-correlation	–
$h$	Blade tip vortex spacing	m
$k$	Perturbation wave number of a vortex track	–
$L$	Lift	N

$M$	Magnification factor, $M = z_0/Z_0$	–
$n$	Exponent Vatisas vortex models	–
$N_i$	Image particle density	–
$N_b$	Number of blades	–
$n_{v, \text{mean}}$	Mean secondary vortex number per $360^\circ$ azimuth	–
$p$	Pressure	Pa
$p_p$	Normalized particle diameter	–
$Q$	$Q$ vortex criterion	$\text{s}^{-2}$
$q_1$	Particle size distribution of length	–
$q_2$	Particle size distribution of area	–
$q_3$	Particle size distribution of volume	–
$R$	Rotor radius, $R = 0.76 \text{ m}$	m
$r$	Radial coordinate	m
$\bar{r}$	Dimensionless vortex radius $\bar{r} = r/r_c$	–
$r_0$	Rankine vortex core radius	m
$r_c$	Vortex core radius	m
$Re$	Reynolds number, $Re = \frac{V_c}{\nu}$	–
$Re_v$	Vortex Reynolds number, $Re = \frac{\Gamma_v}{\nu}$	–
$S$	Vortex stretching factor	–
$\mathbf{S}$	Velocity gradient tensor	–
$T$	Rotor thrust	N
$t$	Time	s
$\Delta t$	Time delay between the PIV double-frames	s
$t^*$	Non-dimensional time, $t^* = t\Gamma/2\pi^2h^2$	–
$u, v, w$	Velocity components in $x, y, z$ -directions	$\text{m s}^{-1}$
$\mathbf{V}$	Velocity vector,	$\text{m s}^{-1}$
$V_\infty$	Free stream velocity	$\text{m s}^{-1}$
$V_{\text{tip}}$	Blade tip velocity, $V_{\text{tip}} = \Omega R$	$\text{m s}^{-1}$
$V_\Theta$	Swirl velocity around vortex center	$\text{m s}^{-1}$
$V_g$	Particle sink velocity	$\text{m s}^{-1}$

$V_s$	Particle velocity lag	$\text{m s}^{-1}$
$v_h$	Hover induced velocity, $v_h = V_{\text{tip}} \sqrt{\frac{C_T}{2}}$	$\text{m s}^{-1}$
$x, y, z$	Cartesian coordinates in the reference frame	m
$y^+$	Non-dimensional wall distance	–
$z_{\text{LS}}$	Light sheet thickness	m

### **Operators**

$\mathcal{C}$	Integration path for line integrals
$\Im$	Imaginary part of a complex number



# 1. Introduction

Rotorcraft constitute a significant component of modern aviation. Their capability for vertical take-off and landing (VTOL), combined with superior three-dimensional maneuverability compared to fixed-wing aircraft, allows them to perform difficult flight operations within confined spaces. These unique characteristics support a broad spectrum of applications, including search-and-rescue (SAR) missions, law enforcement and military operations, specialized transportation, cargo delivery and agricultural and infrastructure related work. Nonetheless, rotorcraft are subject to several limitations, among which two are particularly prominent. First, their efficiency is generally lower than that of most fixed-wing aircraft. Second, despite substantial technological progress in recent decades, rotorcraft continue to generate very high noise levels. This not only challenges their public acceptance in civil applications but also limits their effectiveness in military missions, where acoustic detectability can compromise operational success.

Significant progress has been made in addressing these challenges, partly due to advances in aerodynamic design. Nevertheless, the inherently greater complexity of rotorcraft aerodynamics, compared with that of fixed-wing aircraft, renders their design considerably more demanding. In addition to unsteady aerodynamic phenomena such as dynamic stall and compressibility effects at the blade tip, the rotor wake itself plays a crucial role, as it not only propagates downstream, but also interacts with the rotor system and the surrounding environment.



**Figure 1.1.:** Vortex system of a BO105, visualized with BOS, from Bauknecht et al. (2014)

The rotor wake is primarily characterized by the helix-shaped trailing blade tip vortices, the blade shear layers, the rotor induced velocity and the external flow conditions. The interaction of these mechanisms leads to a breakdown of the vortex system with its downward propagation. In particular, the blade tip vortices, which are initially well-defined, undergo gradual decay and instability with increasing vortex age, see Fig. 1.1. This vortex decay has been investigated for many years.

Due to its complexity, the numerical simulation of this breakdown is still challenging and therefore subject to ongoing research. The vortex decomposition is influenced by complex vortex-vortex interactions, and it is highly relevant to the efficiency and noise development of rotors, particularly in hover. Accordingly, these effects need to be investigated in detail.

### 1.1. State of the Art

A detailed understanding of blade tip vortex behavior is crucial for predicting the acoustic and loads characteristics of a rotor. In the near wake, the size and strength of the vortices govern unsteady blade loads and impulsive noise generation associated with blade-vortex interactions (BVI), see Ramasamy et al. (2007). In the far wake, the vortices induce pronounced velocity peaks that can develop into powerful gusts, posing a potential hazard to personnel in the vicinity of landing or departing helicopters and promoting the upwash loose of sediment (Brownout).

The state of the art in primary vortex research focuses mainly on velocity profiles, vortex-vortex interaction, and vortex decay. Predicting vortex velocity profiles with reduced-order models remains a central challenge. Several vortex models have been proposed, ranging from fully physical descriptions for laminar vortices, e.g., by Lamb (1932) and Oseen (1912), through semi-empirical formulations (e.g., Ramasamy et al. (2007)), to fully empirical n-vortex models by Vatistas et al. (2015). Despite the large number of models, the state of the art lacks a comprehensive comparative assessment of their predictive performance.

When discussing the interaction and decay of blade tip vortices, a large body of experimental and numerical work has been published. Despite the substantial efforts, detailed comparisons between experiments and simulations continue to reveal significant discrepancies, particularly in predicting vortex decay. To mitigate these discrepancies, researchers have employed higher-order DDES solvers and extremely fine spatial resolutions, down to  $1\%c$  in the background mesh, in an attempt to reduce numerical dissipation. These refined simulations revealed additional small-scale vortex structures, often referred to as “vortex worms,” which rotate perpendicular to the primary vortex and contributing to its decay. Chaderjian et al. (2011) were the first to observe the existence of these vortex worms, see Fig. 1.2a, and discussed whether these structures, also known as secondary vortices, trigger an earlier vortex breakdown. In later studies, the numerical observation of secondary vortices was reproduced under a variety of conditions, e.g., by Hariharan et al. (2014), Potsdam et al. (2014), Öhrle et al. (2018), Jain (2018) or Bodling et al. (2022).

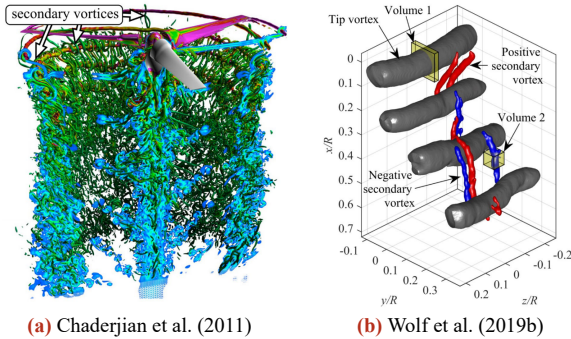


**Figure 1.2.:** Previous numerical and experimental investigations of secondary structures

Despite the numerical evidence, it was debated by Egolf et al. (2017), for example, to what extent these structures are a physical or merely a numerical phenomenon. Moreover, Abras et al. (2019) determined a strong dependency on the numerical parameters, such as time-step width and grid resolution.

In 2019, Wolf et al. (2019b) first proved their existence in an experiment. They were able to visualize the secondary vortices with a three-dimensional Shake-the-Box Lagrangian particle tracking technique (Schanz et al. (2016)), see Fig. 1.2b. In a subsequent experimental study, Schwarz et al. (2022) quantified the appearance of the secondary vortices in a number of horizontal Stereo-Particle Image Velocimetry (PIV) planes and compared it with numerical simulations of the same test case. However, their study focused on only one specific test case. Bodling et al. (2024) then used the same test case to investigate the influence of different parameters on the average amount of secondary structures. Focusing on configurational changes, they explored the relationship between blade tip vortex behavior and the development of secondary vortices in the numerical results. A key finding was a direct correlation between blade tip vortex breakdown and the average amount of secondary structures in the numerical simulation. Additionally, they showed that a slight offset in the pitch angle between the two blades leads to a comparable pairing behavior in the simulation and the corresponding experiment. In conclusion, the pitch offset influences both the vortex breakdown and the number of secondary structures, and it yields a better agreement between simulations and experimental results.

The recent numerical aeroacoustic study by Thurman et al. (2024) indicates that initial secondary vortices also contribute to BVI noise and are therefore important for an accurate noise prediction of a helicopter.

## 1.2. Thesis Organization

This thesis presents the investigation of the development and interaction of primary and secondary vortices generated by a hovering rotor. Chapter 2 introduces the fundamentals of vortex dynamics, their interactions, and defining characteristics. The experimental setup and an uncertainty analysis of the conducted measurements are presented in Chap. 3. The processing of the experimental data is described in Chap. 4. While studies of the near wake of a hovering rotor are available in the literature, investigations of the far wake and high-resolution measurements remain comparatively rare. For this reason, a detailed analysis of primary vortices up to a vortex age of approximately  $2000^\circ$  is presented in Chap. 5. These measurements were performed for selected cases, enabling high-resolution data to accurately determine the maximum swirl velocity and vortex core radius. The experimental results are then compared with common vortex models to assess their ability to capture the underlying vortex physics. Subsequently, Chap. 6 presents a parameter study of primary and secondary blade tip vortices, with selected cases additionally compared against numerical data provided by our project partners.

The central research questions addressed in this thesis are summarized as follows:

- *How accurately do existing vortex models reproduce the measured blade tip vortices?*
- *Which influencing factors govern the occurrence of secondary vortices?*
- *How do secondary vortices contribute to vortex breakdown and interactions?*

## 2. Theory of Blade Tip Vortices

This chapter introduces the theoretical background necessary to understand the development and behavior of blade tip vortices. It begins with an explanation of why wing tip vortices arise on finite wings, followed by a discussion of the general properties of vortices. These fundamentals provide the basis for introducing blade tip vortices and their specific features in Chap. 2.2.

To interpret measured vortex characteristics, analytical descriptions from the literature are required. Several vortex models are therefore presented in Chap. 2.3, and later benchmarked against experimental results in Chap. 5. Because these evaluations rely on the ability to identify vortices within flow fields, Chap. 2.4 outlines the most common vortex detection criteria, emphasizing that the choice of criterion depends strongly on the definition of a vortex.

Real blade tip vortices do not remain idealized structures, but are subject to disturbances and mutual interactions. Chap. 2.5 provides a short overview of theoretical approaches to describe such instabilities. Finally, the occurrence of secondary vortex structures in non-rotor flows is briefly summarized to place the rotor-specific discussion in a broader aerodynamic context.

### 2.1. Vortex Fundamentals

To provide the physical basis for understanding blade tip vortices in rotors, this section first explains why finite span wings generate a three-dimensional flow field, causing a reduction in lift close to the wingtips. This phenomenon arises from the equalization of the pressure difference between upper and lower wing at the wingtip. Green (1995) mentions three explanations for the formation of tip vortices, of which the following two are the most common:

First, the pressure distribution across the span of a finite wing causes streamlines to behave differently on the upper and lower surfaces. On the upper surface, the streamlines curve inward toward the wing root, while those on the lower surface curve outwards towards the wingtips, as shown in Fig. 2.1. The curvature of the streamlines leads to the creation of two counter-rotating wingtip vortices that extend downstream along the wake, as explained by Anderson (2017).

Second, the formation of wingtip vortices can be understood through the vortex laws established by Thomson (1880) and Helmholtz (1858). A finite wing possesses a bound vortex, as part of the circulation which is needed to generate lift and can be described after Kutta-

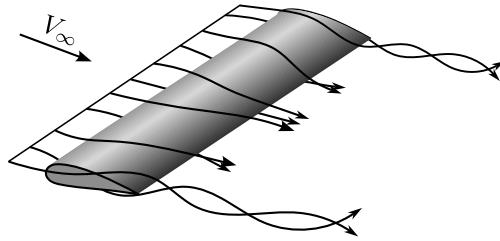


**Figure 2.1.:** Schematic streamlines around a finite wing

Joukowski as

$$L = \rho b V_\infty \Gamma. \quad (2.1)$$

To conserve circulation, vortices are not allowed ending somewhere in the flow field. As a consequence, counter-rotating free vortices at the wing tips must be created. Depending on the application case, these vortices may extend to infinity or connect with a starting vortex, see Prandtl (1919).

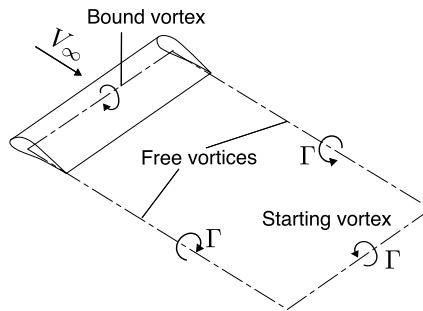


**Figure 2.2.:** Simplified vortex system of a finite wing, after Schlichting et al. (2013)

The model with a single bound vortex on a finite wing result in infinite downwash velocities at the wing tips, which is not physical. To address this, Prandtl (1919) developed a more refined model for high aspect ratio wings: the lifting-line theory. This model represents the wing as a superposition of an infinite number of bound vortices, allowing a spanwise distribution of circulation or lift, and provides a deeper understanding of the physics of wing tip and shear

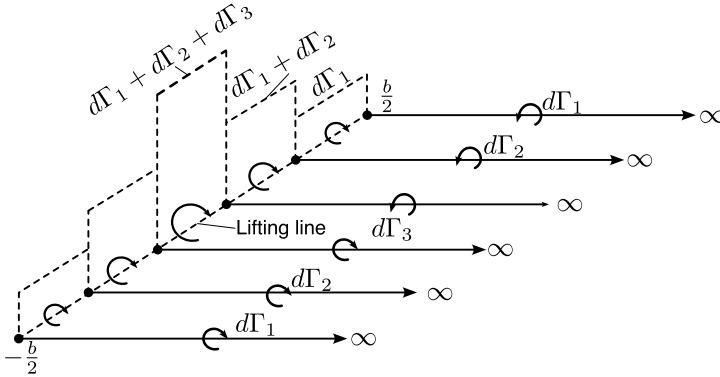


**Figure 2.3.:** Concept of lifting-line theory, after Anderson (2017)

layer formation. For illustration purposes the wing is represented in Fig. 2.3 as three discrete horseshoe vortices. The total circulation is now a result of the superposition of each of these vortices and is a function of the spanwise coordinate  $y$ . According to the laws of Thomson and Helmholtz, each bound vortex generates two trailing vortices. The strength of these vortices must be equal to the change in circulation at the lifting-line ( $d\Gamma/dy$ ). The induced downwash from each of those vortices is defined as

$$dw = -\frac{(d\Gamma/dy)dy}{4\pi(y_0 - y)} \quad (2.2)$$

and is the reason for the existence of induced drag for finite wings, see Anderson (2017).

For vortex formation this means that the vortex is first created over the whole wing, depending on the local circulation gradient  $\frac{d\Gamma}{dy}$ . This results in a sheet of vorticity just behind the wing, which is rolled up into two distinct counter-rotating wing tip vortices. However, this roll-up process is complex and the subject of ongoing research, a detailed description can be found, for example, in Giuni et al. (2013) or Birch et al. (2003).

For heavy transport aircraft, these wingtip vortices are sufficiently strong to cause a hazard to following aircraft and contribute to the necessity of maintaining a significant distance between take-off and following aircraft.

Once an initial roll-up has occurred, the formation of two counter-rotating wing tip vortices can be observed. In order to study their properties, the vortices themselves must first be defined. The most basic vortex is a potential vortex, characterized by concentric streamlines around a common vortex center, and the tangential velocity distribution:

$$V_\theta = \frac{\Gamma_v}{2\pi r} \quad (2.3)$$

For  $r > 0$ , the flow is free of divergence ( $\nabla \cdot \mathbf{V} = 0$ ) and rotation ( $\nabla \times \mathbf{V} = 0$ ), and the vortex circulation is constant. For  $r \rightarrow 0$ , however, a singularity with infinite velocity arises. This is not physical, and is results from the fact that potential flow neglects viscous effects, which dominate in the inner vortex core. The swirl velocity and circulation distribution of a typical “true” vortex are shown in Fig. 2.4.

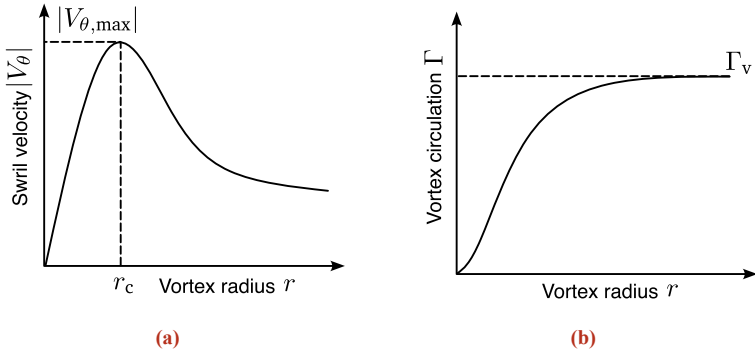


**Figure 2.4.:** Sketch of vortex swirl velocity  $V_\theta$  (a) and circulation  $\Gamma$  (b) distribution over the vortex radius  $r$

To address this singularity, vortices are commonly described as consisting of an inner and an outer part. The inner part, also known as the vortex core, is dominated by viscous flow, which decelerates the swirl velocity to zero at the vortex center  $r = 0$ . The vortex core size is typically defined as the radial position of the maximum swirl velocity of the vortex, while the outer region is well represented by a potential vortex. A more detailed discussion of vortex models is provided in Chap. 2.3.

To measure the vortex strength, the vortex circulation  $\Gamma_v$  is widely used. The formulation of the potential vortex gives the definition at a circumference  $\mathcal{C} = 2\pi r$ :

$$\Gamma_v = \oint_{\mathcal{C}} \mathbf{V} \cdot d\mathbf{s} = -V_\theta(2\pi r) \quad (2.4)$$

For non-potential vortices, the circulation depends on the radial position. However, it converges towards the total vortex circulation for large radii, as shown in Fig. 2.4b.

## 2.2. Blade Tip Vortices

Building on these fundamentals, this section explains why, unlike fixed-wing aircraft, rotors generate primarily co-rotating blade tip vortices in the wake. Prandtl's lifting-line theory, introduced in Chap. 2.1, provides a useful framework for explaining this phenomenon. Although originally developed for fixed wings, it still offers a useful approximation for rotor blades, despite not fully accounting for rotational effects. In general, the circulation is governed by blade geometry, local relative velocity, and air density. For a rectangular fixed wing, these parameters remain constant along the span. In contrast, a rectangular rotor blade experiences a local velocity that increases linearly with radius. Consequently, the drop in circulation near the blade tip is much less pronounced than at the blade root, causing a stronger outer tip vortex compared to the inner tip vortex.

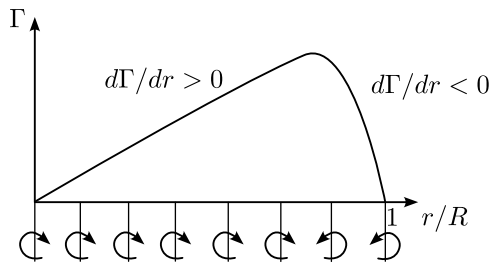


**Figure 2.5.:** Circulation distribution over a rotating blade, after Goertler (2020)

This principle is illustrated in Fig. 2.5. While the outer vortices now roll up to form the helix-shaped blade tip vortices, the inner vortices form a shear layer that is convected downstream. Because the shear layer has a higher convection velocity, it interacts with older blade tip vortices, leading to a second roll-up process between them.

A detailed sketch of the resulting vortex system is provided in Fig. 2.6. Here, the vortex age  $\psi_v$  is introduced as a parameter describing the azimuthal distance a shear layer or vortex has traveled since its formation.

To summarize, a key distinction between fixed wing and rotor vortex systems is that, for rotors, the tip vortices do not simply convect downstream but instead form a helical system. Capturing the structure and dynamics of these vortices is crucial for predicting rotor blade loading and aeroacoustic phenomena such as blade-vortex interactions (BVI).

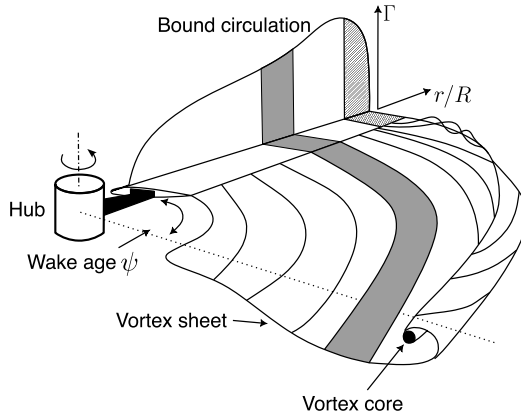


**Figure 2.6.:** Blade tip vortex creation, after Martin et al. (2002)

## 2.3. Vortex Models

To predict and later benchmark vortex behavior against experimental data, vortex models provide analytical approximations for various applications and levels of complexity. The discussed models are plotted for a fixed circulation of  $\Gamma_v = 2\pi r_c$  in Fig. 2.7, demonstrating their different velocity profiles. A very simplified model is the previously discussed potential vortex, where the absence of viscosity in the vortex core leads to a singularity in velocity at  $r = 0$ . Rankine (1858) addressed this problem by proposing a model with a viscous core region. In this model the vortex is divided into two parts: a solid body rotation for  $r \leq r_0$  and an outer region coinciding with the potential vortex for  $r > r_0$ :

$$V_\theta(r) = \frac{\Gamma_v}{2\pi} \begin{cases} r \cdot r_0^{-2}, & r \leq r_0, \\ r^{-1}, & r > r_0, \end{cases} \quad (2.5)$$

In this formulation, the swirl velocity increases linearly from zero at the vortex center to the potential vortex value at  $r = r_0$ , while beyond this radius the  $1/r$  profile of the potential vortex is retained. Although this addresses the issue of viscosity in the inner part of the vortex, the Rankine vortex still contains a discontinuity, leading to an unrealistically high swirl velocity at the “kink,” as noted by Leishman (2002).

A more advanced formulation was later introduced by Oseen (1912) and Lamb (1932), who derived a vortex model from the two-dimensional incompressible Navier-Stokes equations

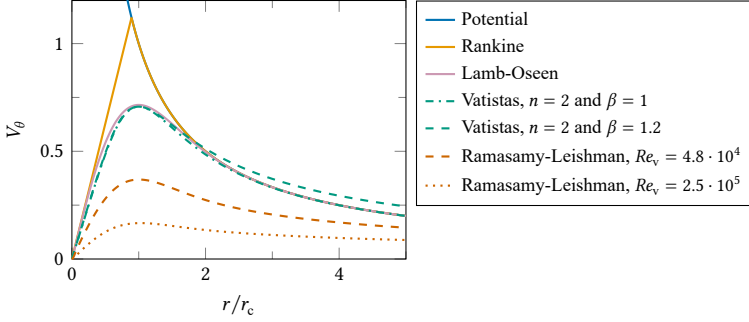


**Figure 2.7.:** Vortex models for a vortex circulation of  $\Gamma_v = 2\pi r_c$

under the assumption of constant viscosity. The Lamb-Oseen vortex model is expressed as:

$$V_\theta(r) = \frac{\Gamma_v}{2\pi r_c \bar{r}} \left(1 - e^{-\alpha_L^2 \bar{r}^2}\right), \quad \bar{r} = \frac{r}{r_c} \quad (2.6)$$

From the radial derivative of this expression, the maximum swirl velocity can be obtained. The radial position of this maximum is commonly the vortex core radius  $r_c$ . For the Lamb-Oseen vortex, this definition gives  $r_c = 1.1209 r_0$ , which corresponds to a Lamb-Oseen constant of  $\alpha_L = 1.1209$ . Especially for PIV measurements, the vortex core radius is easier to derive than the inner vortex slope of the Rankine vortex, due to the lack of data inside the inner vortex. Despite the direct derivation of the Lamb-Oseen vortex model from the two-dimensional Navier-Stokes equations, there are two major limitations. First, the solution is restricted to laminar vortices. Second, it applies only to vortices without axial velocity components. After defining the swirl velocity distribution, the vortex core radius after for the Lamb-Oseen vortex is given as

$$r_c = 2\alpha_L \sqrt{\nu t}. \quad (2.7)$$

A widely used alternative are the purely empirical  $n$ -family vortex models, developed by Vatisas et al. (1991), see Kuenn et al. (2021). The tangential velocity distribution is defined as:

$$V_\theta(\bar{r}) = \frac{\Gamma_v}{2\pi r_c} \frac{\bar{r}}{(1 + \bar{r}^{2n})^{1/n}} \quad (2.8)$$

where  $n$  is an adjustable parameter. For an  $n \rightarrow \infty$  the model converges to the Rankine model. If  $n = 1$ , it corresponds to the Scully-Kaufmann vortex (Scully et al. (1972), Kaufmann (1962)). Vatisas et al. (2015) demonstrated that  $n = 2$  produces very similar solutions to the Lamb-Oseen vortex.

An advantage of the  $n$  family vortex is the possible extension to model the influence of turbulence in vortices. Vatisas et al. (2015) extended the model by adding an empirical equation based on experimental data:

$$V_{\theta}(\bar{r}) = \frac{\Gamma_v}{2\pi r_c} 2^{-\frac{1}{n}} \bar{r} \left( \frac{1 + \beta}{1 + \beta \bar{r}^{2n}} \right)^{\frac{(1+\beta)}{(2n\beta)}} \quad (2.9)$$

The model is now capable of calculating both laminar vortices ( $\beta = 1$ ) and turbulent vortices ( $\beta > 1$ ). As shown in Fig. 2.7,  $\beta$  primarily affects the outer region of the vortex, while the maximum swirl velocity remains constant, as determined by the maximum value in Eq. 2.8:

$$V_{\theta, \max, \text{Vatistas}} = \frac{\Gamma_v}{2\pi r_c} \cdot 2^{-\frac{1}{n}}. \quad (2.10)$$

Consider that the Vatistas model with turbulence ( $\beta > 1$ ) does not ensure a constant circulation for large radii of  $r \gg r_c$  as, predicted by the Lamb-Oseen model. As a consequence, the input circulation for Eq. 2.10 is only achieved at a certain radius and is not valid for the whole vortex.

Ramasamy et al. (2006) and Ramasamy et al. (2007) proposed a more physically based approach to introduce the effect of turbulence into a vortex model. The Ramasamy-Leishman model is given by<sup>1</sup>:

$$V_{\theta}(r) = \frac{\Gamma_v}{2\pi r} \left[ 1 - \sum_{n=1}^3 a_n e^{-b_n r^2} \right]. \quad (2.11)$$

The coefficients for the series expansion represent the impact of turbulence in the vortex. Table 2.1 provides these coefficients, which are based on a curve fit to experimental data from vortex measurements. In addition, the relation

$$\sum_{n=1}^3 a_n = 1 \quad (2.12)$$

must be satisfied to ensure the modeled swirl velocity to be zero in the vortex center. To predict the vortex core growth Squire (1965) and Bhagwat et al. (2002) adapted the Lamb-Oseen vortex growth equation to

$$\sqrt{r_c^2 + 4\alpha_L^2 v \delta t} \quad (2.13)$$

and included an initial core radius  $r_c, \psi=0$  and a factor  $\delta$  to model the influence of turbulence on viscosity.

Vortex perturbations cause local stretching or squeezing of vortex filament, defined as:

$$\varepsilon = \frac{\Delta l}{l}. \quad (2.14)$$

---

<sup>1</sup>Ramasamy et al. (2007) provide a different exponent for  $r$  in their paper, which fails to reproduce the Lamb-Oseen model at  $Re = 1$ . By choosing the corresponding exponents it seems to be convenient to correct  $r$  to  $\bar{r}^2$ , as given in Eq. 2.11

**Table 2.1.:** Coefficients for constants in the series expansion of the Ramasamy-Leishman vortex model as a function of the vortex Reynolds number. Data from Ramasamy et al. (2007)

$Re_v$	$a_1$	$b_1$	$a_2$	$b_2$	$b_3$
1	1.0000	1.256	0.0000	0.0000	0.0000
10,000	0.8247	1.2073	0.1753	0.0263	0.0000
$2.5 \times 10^4$	0.5933	1.3480	0.2678	0.0187	0.2070
$4.8 \times 10^4$	0.4602	1.3660	0.3800	0.0138	0.1674
$2.5 \times 10^5$	0.1838	1.4563	0.6854	0.0083	0.1412
$1 \times 10^6$	0.1231	1.7912	0.7667	0.0145	0.2733

To include this mechanism Ananthan et al. (2004) added a second term to the aforementioned Eq. 2.13, resulting in:

$$r_c(\psi_v, \varepsilon) = \sqrt{r_{c, \psi_v=0}^2 + \frac{4\alpha_L^2 \delta(Re_v) \nu}{\Omega} \int_{\psi_0}^{\psi_v} (1 + \varepsilon(\psi))^{-1} d\psi} \quad (2.15)$$

where  $\psi_v$  is the vortex age and  $\varepsilon$  is the vortex stretching term. This formulation is based on the conservation of mass and momentum inside the vortex, which means that stretching leads to a smaller vortex with higher swirl velocity, whereas compression increases the vortex core and reduces the tangential velocity.

## 2.4. Vortex Detection Criteria

Interpreting experimental or numerical velocity data requires the ability to identify vortices in complex flow fields, making vortex detection criteria essential. Although an idealized vortex, such as the potential vortex discussed earlier, has a clear definition, an exact formulation of a real vortex is more challenging. A widely used definition of a vortex was proposed by Robinson (1990): “A vortex exists when instantaneous streamlines mapped onto a plane normal to the vortex core exhibit a roughly circular or spiral pattern, when viewed from a reference frame moving with the center of the vortex core.”

Detecting vortices in a turbulent flow field is considerably more difficult. The main challenge arises from the superposition with the surrounding background flow, which often distorts the vortex, and the vortex center is not known *a priori*. As a result, numerous vortex criteria have been proposed, each responding to specific local properties of the flow field.

For a local two-dimensional flow field analysis the velocity gradient tensor

$$\mathbf{A} = \begin{bmatrix} \frac{\partial u}{\partial x} & \left(\frac{\partial v}{\partial x} + \frac{\partial u}{\partial y}\right)/2 \\ \left(\frac{\partial u}{\partial y} + \frac{\partial v}{\partial x}\right)/2 & \frac{\partial v}{\partial y} \end{bmatrix} + \begin{bmatrix} 0 & \left(\frac{\partial v}{\partial x} - \frac{\partial u}{\partial y}\right)/2 \\ \left(\frac{\partial u}{\partial y} - \frac{\partial v}{\partial x}\right)/2 & 0 \end{bmatrix} \quad (2.16)$$

$$= \begin{bmatrix} \varepsilon_{xx} & \varepsilon_{xy} \\ \varepsilon_{yx} & \varepsilon_{yy} \end{bmatrix} + \begin{bmatrix} 0 & -\omega_z \\ \omega_z & 0 \end{bmatrix} = \mathbf{S} + \mathbf{\Omega}$$

allows the separate extraction of symmetric and asymmetric parts, see Lugt (1996). The velocity gradient tensor is Galilean invariant, and it also directly corresponds to the vorticity, as shown in Eq. 2.16.

The mathematical properties of this tensor are used by various vortex criteria to detect vortices. An analysis of the eigenvalues helps to classify rotating flow structures. The eigenvalues of a matrix are defined as

$$\det(\mathbf{A} - I\lambda) = 0. \quad (2.17)$$

Solving this equation with the characteristic polynomial gives

$$\lambda^2 - \lambda \operatorname{tr} \mathbf{A} + \det \mathbf{A} = 0, \quad (2.18)$$

where the determinant and the trace of the velocity tensor  $\mathbf{A}$  are

$$\det \mathbf{A} = \frac{\partial u}{\partial x} \frac{\partial v}{\partial y} - \frac{\partial u}{\partial y} \frac{\partial v}{\partial x} \quad (2.19)$$

$$\operatorname{tr} \mathbf{A} = \frac{\partial u}{\partial x} + \frac{\partial v}{\partial y} \quad (2.20)$$

As a result, the solution for  $\lambda_{1,2}$  is given by the quadratic formula:

$$\lambda_{1,2} = \frac{\operatorname{tr} \mathbf{A}}{2} \pm \sqrt{\frac{(\operatorname{tr} \mathbf{A})^2}{4} - \det \mathbf{A}} \quad (2.21)$$

Figure 2.8 shows how the determinant and the trace of the tensor helps to classify physical flow patterns in the flow field. In particular, direct physical statements can be derived from the relationship between the trace and the determinant. The discriminant  $D = (\operatorname{tr} \mathbf{A})^2/4 - \det \mathbf{A}$  in Eq. 2.21 determines whether  $\lambda$  is real or complex conjugate. This case distinction is shown by the parabola in Fig. 2.8.

If  $D < 0$ , or equivalently  $\det \mathbf{A} > (\operatorname{tr} \mathbf{A})^2/4$ , Eq. 2.21 returns complex conjugate eigenvalues, which directly correspond to a rotational motion. For  $\det \mathbf{A} \neq 0$  this results a focus, whereas for

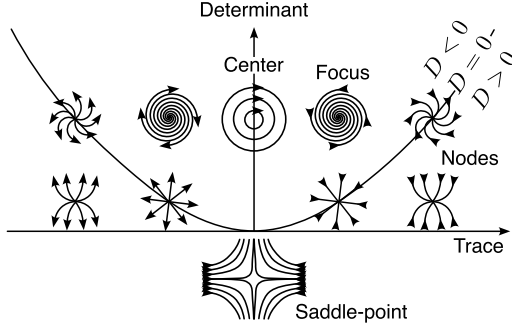


**Figure 2.8.:** Trace-Determinant Diagram, after Vollmers (2001)

$\det \mathbf{A} = 0$ , it corresponds to a center. The  $Q$ -criterion, proposed by Hunt et al. (1988) defines a vortex to be above this parabola by being defined as

$$Q_{\text{Hunt}} = (\text{tr } \mathbf{A})^2 / 4 - \det \mathbf{A} < 0. \quad (2.22)$$

In literature, however, a stricter formulation of  $Q$  has been introduced by Chen et al. (2015), which defines a vortex to be

$$Q_{-} = (\text{tr } \mathbf{A})^2 / 2 - \det \mathbf{A} < 0 \quad (2.23)$$

As illustrated in Fig. 2.8, this formulation imposes a stricter requirement on the spiral shape of a vortex compared to the alternative criterion. The latter only demands the existence of a conjugate complex eigenvalue pair, which can also arise from a slightly curved source or sink and therefore allows for less well-defined spiral structures. In the following, the formulation of Chen et al. (2015) will be referred to as  $Q$  in this thesis. This choice does not question the validity of *Hunt's* original definition, however, for experimental data affected by noise, a stricter criterion such as that of Chen et al. (2015) is more appropriate.

Among the most common vortex identification methods is the  $\lambda_2$  criterion, proposed by Jeong et al. (1995). It is defined as:

$$\lambda_2 = \|\Omega\|^2 + \|\mathbf{S}\|^2 < 0 \quad (2.24)$$

For three-dimensional flows, this criterion involves the analysis of the eigenvalues of the tensor:

$$\lambda_1 \leq \lambda_2 \leq \lambda_3. \quad (2.25)$$

Under ideal adiabatic conditions, a pressure minimum occurs at the vortex center if at least two eigenvalues are negative and a vortex is detected, see Haller (2005). However, the  $\lambda_2$  criterion is not directly applicable to 2D flow fields, leading to several simplified approaches in the

literature. For instance, van der Wall et al. (2006) proposed Eq. 2.29. They argued that one of the following conditions must be satisfied for vortex detection:

$$\lambda_2 = \left(\frac{\partial u}{\partial x}\right)^2 + \frac{\partial u}{\partial y} \frac{\partial v}{\partial x} < 0 \quad \text{or} \quad \lambda_2 = \left(\frac{\partial v}{\partial y}\right)^2 + \frac{\partial u}{\partial y} \frac{\partial v}{\partial x} < 0 \quad (2.26)$$

The average of both values is then used in the formulation of Eq. 2.29. Other formulations consider only one of these two gradients (Schram et al. (2004)), or use a more complex variant (e.g., Chen et al. (2015)). For flows that are nearly incompressible, the first term in  $\lambda_2$  becomes negligible, resulting in agreement between the different formulations. In such cases, the  $\lambda_2$  criterion also coincides with the  $Q$ -criterion, as shown by Günther et al. (2018).

Zhou et al. (1999) introduced the swirling strength  $\lambda_{ci}$  as a vortex criterion. It is also based on the velocity gradient tensor eigenvalues and is defined as the maximum of the imaginary part of the eigenvalues. According to Haimes et al. (1999), for a three-dimensional flow the tensor  $\mathbf{A}$  can have either three real eigenvalues or one real eigenvalue  $\lambda_r$ , together with a pair of complex conjugate eigenvalues  $\lambda_c$ . Fortunately, this can be easily adapted for the two-dimensional case, since a vortex always has a complex conjugated pair of eigenvalues. The resulting form of the swirling strength is defined in Eq. 2.30. For a rigid body like rotation, swirling strength and vorticity return the same values, see Canivete Cuissa et al. (2020).

$$\omega_z = \left(\frac{\partial u}{\partial y} - \frac{\partial v}{\partial x}\right)/2 \quad (2.27)$$

$$Q = \frac{\partial u}{\partial x} \frac{\partial v}{\partial y} - \frac{\partial u}{\partial y} \frac{\partial v}{\partial x} - \frac{1}{2} \left(\frac{\partial u}{\partial x} + \frac{\partial v}{\partial y}\right)^2 \quad (2.28)$$

$$\lambda_2 = \left(\left(\frac{\partial u}{\partial x}\right)^2 + \left(\frac{\partial v}{\partial y}\right)^2\right)/2 + \frac{\partial v}{\partial x} \frac{\partial u}{\partial y} \quad (2.29)$$

$$\lambda_{ci} = \max \left[ \Im \left\{ \left(\frac{\partial u}{\partial x} + \frac{\partial v}{\partial y}\right)/2 + \sqrt{Q} \right\}, \Im \left\{ \left(\frac{\partial u}{\partial x} + \frac{\partial v}{\partial y}\right)/2 - \sqrt{Q} \right\} \right] \quad (2.30)$$

The criteria only differ if the vortex to be detected is strongly superimposed by shear influence. To illustrate this, an artificial velocity field is generated with three Lamb-Oseen vortices and a shear layer with Gaussian velocity distribution, shown in Fig. 2.9a. In the further sub figures of Fig. 2.9 the result of the discussed vortex criteria is shown. The biggest difference in detection is seen when comparing vorticity with the other vortex criteria. While the other vortex criteria show only small deviations due to the shear layer, vorticity, as expected, also shows a deviation due to the shear flow. This could lead to false detections in pure vortex detection. For the other criteria, all vortices are reliably detected, and the difference is limited to the magnitude and the sign. In addition to vortex detection, the swirling strength also provides information about the direction of rotation.

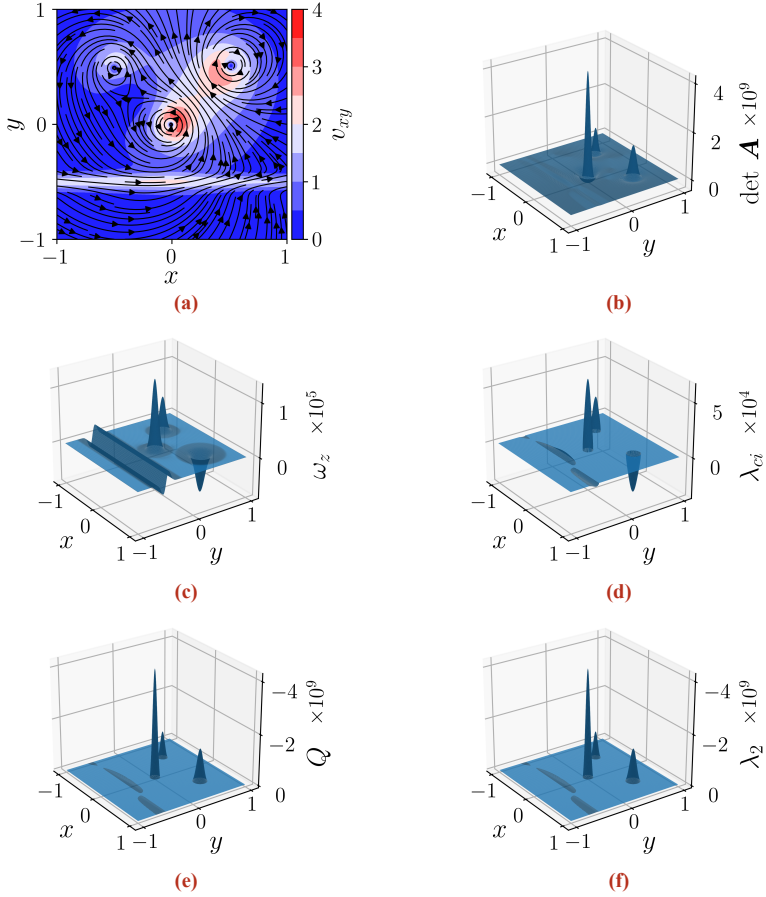


**Figure 2.9.:** Vortex criteria on artificial flow field, similar to Schram et al. (2004). (a) Artificial flow field, (b) Flow field tensor determinant (c) Vorticity  $\omega_z$ , (d) Swirling strength  $\lambda_{ci}$ , (e)  $Q$ -criterion, (f)  $\lambda_2$ -criterion

In the present example, only ideal vortices are considered, limited to tangential velocity components:

$$\frac{\partial u}{\partial x} = 0, \frac{\partial v}{\partial y} = 0 \quad (2.31)$$

As a result, the trace of the velocity gradient tensor must also be zero ( $\text{tr } \mathbf{A} = 0$ ), as illustrated in Fig. 2.8. For such an undisturbed vortex, the square of the vorticity,  $\omega_z^2$ , coincides with the values of  $\det(\mathbf{A})$ ,  $\lambda_2$ ,  $Q$  and  $(2\lambda_{ci})^2$ .

## 2.5. Vortex Disturbances and Interactions

This section introduces the theoretical framework for analyzing disturbances and interactions of blade tip vortices, focusing on stability concepts and simplified models that explain how perturbations grow and influence vortex evolution.

A common approach in fluid dynamics is to decompose the flow into a steady component and an unsteady perturbation. This method, known as Reynolds decomposition, was introduced by Reynolds (1883), who separated the flow components into their time-averaged and fluctuating components. One of the most prominent applications of this concept is Linear Stability Theory (LST), which has been used extensively to predict laminar-turbulent transition in boundary layers. In LST, the amplification of a perturbation indicates the instability of a boundary layer. By employing a Fourier approach to solve the perturbation function, the  $e^N$  method provides an efficient and accurate prediction of the laminar-turbulent transition (see, e.g., Van Ingen (2008)).

Analogous to boundary layers, vortices are also subject to instability-driven disturbances. In the study of vortex decay, a widely used approach is to investigate the displacement of an instantaneous vortex filament relative to its anticipated position. It is customary to categorize the disturbances based on their wavelength. For classification purposes, distinctions are often made between long- and short wave instabilities<sup>2</sup>.

Short-wavelength instabilities develop within vortex cores, with perturbation wavelengths typically on the order of the core diameter. These instabilities result from the resonant amplification of so-called Kelvin modes and interact with the surrounding flow, see Lewke et al. (2014).

Perturbations significantly larger than the vortex core are defined as long-wave instabilities. These perturbations lead to an overall deformation of the vortex system. For helical vortices, vortex pairing is the most common long-wave instability.

---

<sup>2</sup>Breitsamter (2011), for example, additionally defines medium-wavelength crouch instability and ultra-short wavelength vortex merging instabilities for counter-rotating wing tip vortices. Since this distinction was not found for rotors, these categories are not discussed here.

### 2.5.1. Vortex Pairs and Arrays

One of the simplest models for studying vortex interaction is the interaction of a vortex pair. In the following, this model is used to describe the phenomenology of the stability of two vortices. It is crucial to distinguish between co- and counter rotating vortex pairs. While two identical co-rotating vortices start to pair and eventually merge due to the mutual induction of circulation as the vortex age increases, counter-rotating vortices develop a first-order Crow instability, leading to the decay of their structures.

In preparation for the discussion of helical vortex systems later in this section, the following analysis is restricted here to co-rotating vortices. To understand the complex interactions between two co-rotating vortices, Leweke et al. (2014) introduced a streamline representation of co-rotating vortices, see Fig. 2.10. Starting from the vortex center, four distinct regions can be defined: the inner core region, the inner- and outer recirculation region, and the outer region. The inner recirculation region is characterized by a mass flow between and around the vortices. In the outer recirculation region, the flow rotates in the opposite direction to the direction of vortex rotation, see Cerretelli et al. (2003). The outer region is separated from the interaction region of the vortices and their mass flow by a closed streamline.

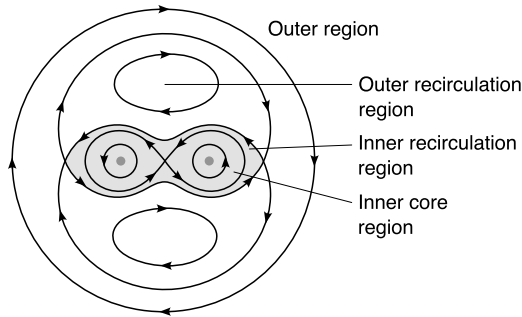


**Figure 2.10.:** Co-rotating vortex pair, after Leweke et al. (2016)

Melander et al. (1988), Leweke et al. (2001) and Cerretelli et al. (2003) have defined four stages of the merging process: In the first stage, known as the diffusive stage, the two vortices begin to pair and exchange vorticity in the inner recirculation region. The second, or convective stage, involves the merging of vorticity from both vortices, followed by the third stage, also known as second diffusive stage. Finally, in the merged diffusive stage, the single merged vortex also disintegrates, see Leweke et al. (2016).

In addition to the long-wave instability caused by vortex merging, short-wave instabilities

also occur in vortex pairs. While the Crow instability (see Crow et al. (1976)) is limited to counter-rotating vortices and will not be discussed further, the elliptical instability occurs in both counter-rotating and co-rotating vortex pairs. As first discussed by Moore et al. (1971), elliptical instabilities arise from an interaction between Kelvin modes superimposed on the axisymmetric vortex and distortions caused by the induced circulation of the other vortex. The relatively small perturbation introduced by the Kelvin mode is amplified by the other vortex, so that the vortex itself deforms into an elliptical shape. The deviation from axisymmetry in turn leads to a stronger periodic influence of the other vortex, resulting in an unstable amplification of the disturbance.

The analysis of vortex pairs provides fundamental insights into the interaction processes of two vortices, many of which are also relevant to rotors. However, a fundamental difference is that rotor vortex systems are influenced by helical curvature instability and additional induction from surrounding vortices, factors not considered in standard vortex pair models.

To account for the effects of surrounding vortices, Abraham et al. (2023) proposed modeling an array of point vortices in a plane to predict the occurrence of vortex pairing. In an axisymmetric generic test case, their model successfully captured the consequences of an asymmetry between the rotor blades. For example, the prediction of the leapfrogging position agrees well to experimental results. As a result, vortex pairing primarily arises from asymmetries, such as differences in vortex circulation, and the interaction caused by Biot-Savart induction.

However, vortex pairing is also observed for very symmetric rotor configurations (see e.g., Bartzsch et al. (2025) or Quaranta et al. (2015)). This shows that the point vortex model has limitations. Possible explanations include the non-inclusion of elliptical instabilities or instabilities arising from the helical flow of the vortex system.

### 2.5.2. Perturbation and Instabilities of Blade Tip Vortices

Blade tip vortices of rotors are organized in helical vortex systems which are dominated by a highly unsteady three-dimensional flow. Technically relevant rotors use at least two rotor blades, resulting in a complex interaction of multiple tip vortex helices. This interaction leads to perturbations and instabilities. Some of these are also valid for vortex pairs and arrays and have already been described in the previous chapter. Others, such as curvature instabilities, appear additionally and their mechanisms are not fully understood, yet, see Blanco-Rodríguez et al. (2016).

Widnall (1972) introduced a model to describe disturbances in helical flows using a generic helical structure superimposed with multiple harmonic perturbations. This model was later extended by Gupta et al. (1974) to account for interactions between multiple helices. These interactions influence the growth rate of the disturbances, depending on their wavenumber. The highest amplification occurs at the wavenumber  $k = N_b \cdot 0.5$  and its odd multiples, see Gupta et al. (1974). In these cases, the maxima and minima of two interacting helices are

aligned in their azimuthal position, resulting in the highest possible amplitude proximity. These models predict vortex pairing, grouping, or merging, all of which have been observed in several experiments (e.g., in Wolf et al. (2022) (pairing), Caradonna (1999) (pairing, merging), Stack et al. (2005) (pairing, grouping)).

A key insight from the basic approximations is that, similar to boundary layer stability theory, a rotor wake presents a stability problem where small perturbations are amplified by orders of magnitude. Quaranta et al. (2015) demonstrated that initial displacements lower than 1% of helix pitch are enough to induce a locking of the rotor wake into an unstable mode. It was also discovered that small asymmetries of the rotors are almost unavoidable, and that only a single-blade rotor is able to provide a trouble-free and precisely reproducible vortex system.

## 2.6. Streamwise Vortices in Non-Helical Vortex Systems

Beyond the study of primary blade tip vortices, this thesis also examines the secondary S-shaped vortex structures that form between adjacent blade tip vortices. Building on the introduction of secondary vortices in rotor wakes given in Chap. 1.1, this chapter discusses the documented occurrence of analogous streamwise vortices in non-helical vortex systems.

Secondary vortices between two primary vortices are not only observed in rotor aerodynamics. In general, co-rotating and counter-rotating vortex pairs can be distinguished, leading to different shapes of secondary structures.

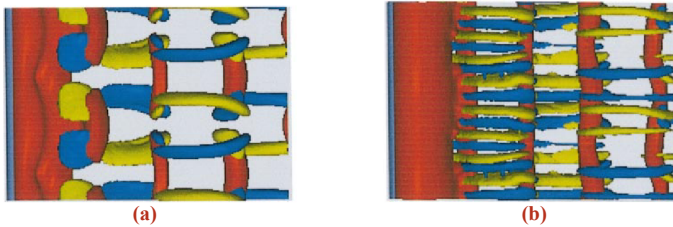


**Figure 2.11.:** DNS of a cylinder wake with streamwise vortices. a) Mode A instabilities ( $Re = 210$ ), b) mode B instabilities ( $Re = 250$ ), from Thompson et al. (2001).

Counter-rotating vortices can be observed, for example, in the wake of a cylinder. A pair of counter-rotating primary vortices (as part of the Kármán vortex street) is surrounded by a secondary vortex loop, as observed by Scarano et al. (2009), Williamson (1988) or Gibeau et al. (2018). Figure 2.11 shows a DNS simulation of a cylinder wake at different Reynolds numbers. Barkley et al. (1996) demonstrated in a Floquet analysis, that the first instability

mode (Mode A instability) occurs at Reynolds numbers of around  $Re = 190$  and his result is shown in Fig. 2.11a. The trailing vortices are interrupted in spanwise direction and each of their intersections are accompanied by a streamwise secondary vortex. The Floquet analysis of Barkley et al. (1996) also reveal the occurrence of a mode B instability at  $Re = 260$ . This is characterized by a continuous vortex in the wake of the cylinder. However, the density of the secondary vortices is significantly higher here, as shown in Fig. 2.11b. The underlying mechanism is not yet understood, see Thompson et al. (2001).

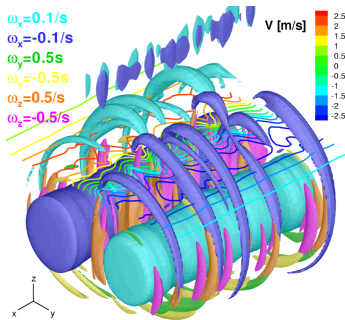


**Figure 2.12.:** Secondary vortices in between counter-rotating vortices in the wake of a transport aircraft, from Holzäpfel (2005)

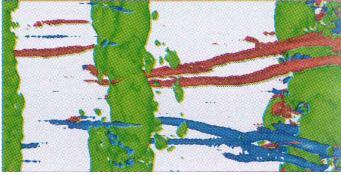
According to the work of Williamson (1988), the streamwise vortices do not arise from Tollmien-Schlichting instabilities on the cylinder, but from the vortices themselves. He observed initial secondary vortices that appear to surround the cylinder. As a consequence, they cannot originate in the boundary layer transition on the cylinder. The amount of the streamwise vortices along the span depends on the Reynolds number and the resulting instability mode. A detailed discussion of this phenomenon is given, for example, by Williamson (1996).

Another well-know example of two counter-rotating vortices is the far wake of a transport airplane in the atmosphere. Experimental and numerical investigations by Holzäpfel et al. (2010), for example, have documented the occurrence of secondary vortices in a similar form as described for the cylinder wake. Large-eddy simulations by Holzäpfel (2005), illustrated in Fig. 2.12, show how secondary vortices form through momentum and mass exchange between the primary vortices, ultimately leading to the rapid turbulent decay of the vortex pair, see Holzäpfel (2005).

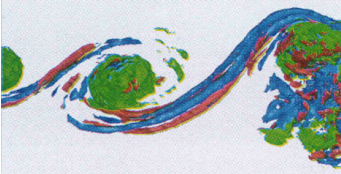
Co-rotating vortices occur, for example, in mixing layers (e.g., described by Bernal et al. (1986)), at cross-flow instabilities during the laminar-turbulent transition (e.g., described by Wassermann et al. (2003)) or between a pair of co-rotating vortices. Bernal et al. (1986) were the first to experimentally observe streamwise vortices between the primary vortices in mixing layers. They suggested that the origin of these vortices was an instability of the initial

shear layer, causing Kelvin-Helmholtz instabilities more downstream. Later, Bell et al. (1992) were able to prove this concept. The LES from Comte et al. (1998) also shows these vortices and gives a deep insight into the small structures. An example is reproduced in Fig. 2.13a. Wassermann et al. (2002) observed similar vortices during the laminar-turbulent transition process of a boundary layer with cross-flow, see Fig. 2.13b. The origin of these vortices is described as a result of the secondary instability mode of linear stability theory (LST).

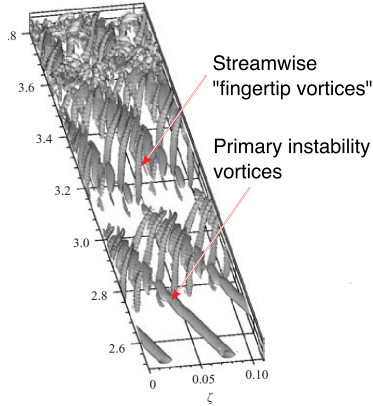
Top View:



Side View:



(a)



(b)

**Figure 2.13.:** Secondary vortices in between co-rotating primary vortices: a) in a mixing layer (LES), adapted from Comte et al. (1998), b) during laminar-turbulent transition in a boundary layer with cross flow (DNS), adapted from Wassermann et al. (2002)

For a co-rotating vortex pair Nybelen et al. (2009) found secondary structures in a high-resolution DNS during the merging process of two co-rotating Lamb-Oseen vortices in an undisturbed environment, see Fig. 2.14. They suggest that these vortices are part of a three-dimensional mass exchange between them, which has already been described for vortex pairs in Chap. 2.5.1. To illustrate, young vortices with an instability characterized by small oscillations around the vortex core are shown in Fig. 2.14a. Figure 2.14b shows a vorticity exchange process between the vortices that starts when the vortex flow becomes turbulent. This exchange is associated with the emergence of secondary vortices. After the non-dimensional time  $t^* = 3.29$  the merging process is completed, and the vorticity is bound in one relaminarized vortex, shown in Fig. 2.14c, see Nybelen et al. (2009). All these cases of co-rotating vortices have in common, that the secondary structures are S-shaped, as observed in rotor aerodynamics.

To summarize, co- and counter rotating vortices exhibit different vortex interaction mecha-

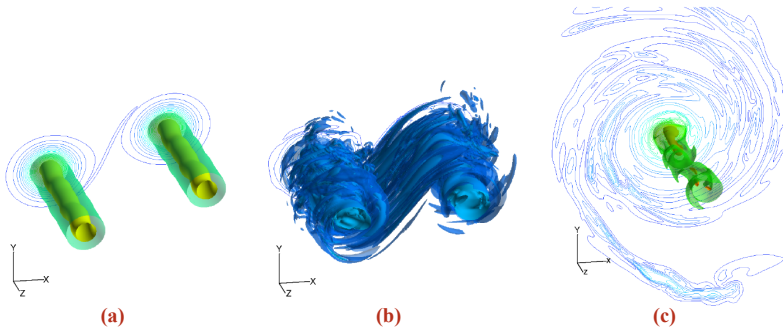


**Figure 2.14.:** Direct numerical simulation of the merging process of a co-rotating Lamb-Oseen vortex pair: a)  $t^* = 1.95$ , b)  $t^* = 2.42$ , c)  $t^* = 3.29$ , reproduced from Nybelen et al. (2009).

nisms. Notably, the inner recirculation region of co-rotating vortices causes the fluid to move around the vortices and strongly influences the instabilities and the flow structure in between, see Leweke et al. (2016).

# 3. Experimental Setup

## 3.1. Measurement Methods

### 3.1.1. Development of Measurement Techniques for Rotor Aerodynamics

The flow field around rotors is dominated by three-dimensional and unsteady aerodynamic effects, which make measurements challenging. However, a detailed understanding of these effects is crucial for further development aiming at increasing efficiency and reducing noise emissions. A brief summary of significant measurement techniques is provided below.

Flow visualizations have historically played a crucial role in understanding rotor flows, particularly rotor wakes, with smoke-based techniques being widely used in the early days of helicopter aerodynamics. The centrifugal forces within vortices shape the smoke patterns, which can be used, to determine vortex position. A well-known example is the development and validation of the prescribed wake model by Landgrebe (1971). Smoke and dye visualizations remain valuable methods for studying vortex interaction effects and are still widely used today (see, e.g., Quaranta et al. (2015) or Serrano-Aguilera et al. (2016)).

Density gradient methods are also widely used vortex visualization tools. Tangler et al. (1973) tracked vortices on a model rotor with a classical Schlieren setup, which poses scalability challenges due to its requirement for large parabolic mirrors. To overcome this limitation, two main alternative measurement techniques have been developed: retroreflective Shadowgraphy and Background-Oriented Schlieren (BOS). Both techniques eliminate the need for parabolic mirrors.

Parthasarathy et al. (1985) demonstrated the feasibility of performing Shadowgraphy measurements with a retroreflective background. This technique was later employed to investigate the blade tip vortices of two S76 rotors ( $R = 0.61$  m), benefiting from its improved scalability. Recent NASA measurements used a slightly adapted method, demonstrating its continued relevance in modern research, see Norman et al. (2023).

Raffel et al. (2000) demonstrated the feasibility of BOS for measuring blade tip vortices of a full-scale helicopter in an airborne experiment. BOS acquires images of a random dot pattern in the background of a helicopter and uses a correlation-based comparison with a reference

image of the same pattern. Using an evaluation similar to PIV gives a displacement field of the pattern due to a density gradient. Measurements by Braukmann et al. (2023) highlighted the scalability of BOS by applying it to the CH-53G, one of the world's largest helicopters.

The most common quantitative methods for rotor investigations include hotwire anemometry, pressure probes, Laser Doppler Velocimetry (LDV) and PIV or Particle Tracking Velocimetry (PTV). While hotwire and LDV measurements provide very high temporal resolutions, their application is restricted to single-point measurements. Before PIV became widely available, and before sufficient laser power was achievable, hotwire and pressure probes were the primary quantitative measurement methods. For turbulence and blade tip vortex investigations, however, a high temporal resolution is required, which was only achievable with hotwire measurements. For example, Tangler et al. (1973) conducted an extensive study on rotor wakes and swirl velocity distributions, combining Schlieren measurements to detect the vortex positions with hotwire anemometry to measure the velocity inside the vortex. However, the vortex wandering made it nearly impossible to measure velocities in the vortex core. Bartzsch et al. (2025) recently showed that, under conditions unsuitable for PIV and with reduced vortex wandering, hotwire anemometry, supplemented by digital data processing and advanced statistics, can still be used to extract key vortex properties.

LDV provides similar results while being non-intrusive, but suffers from the same limitations caused by vortex wandering. Scully et al. (1972) were among the earliest researchers to utilize LDV for rotor wake investigations. They demonstrated the feasibility of non-intrusive quantitative measurements using oil particles as seeding material. A further drawback of LDV, compared with hotwire anemometry, is its non-uniform time base, which makes frequency analysis more challenging.

In the 1990s, PIV significantly enhanced the understanding of helicopter aerodynamics and became one of the key measurement techniques for rotor aerodynamic investigations. The first applications of PIV in this field focused on stall investigations at airfoils, see Raffel et al. (1993). Subsequent studies by Raffel et al. (1996) and Saripalli (1995) were among the first to apply PIV to rotor wakes, benefiting from advancements in progressive scan CCD sensors. These technological improvements enabled the implementation of digital correlation methods, facilitating more sophisticated pre- and post-processing of the data.

In a comparative study with LDV, Raffel et al. (1996) demonstrated that PIV facilitates blade tip vortex measurements by reducing the acquisition time. PIV enables the detection of vortex positions and the calculation of vorticity and swirling strength, providing a more comprehensive flow field analysis. Heineck et al. (2000) presented one of the first detailed discussions on the application of Stereo-PIV to a rotor in a hover test stand. Their analysis began with vortex detection in instantaneous flow fields. As explained in Chap. 2.5.2, vortex positions are influenced by several types of perturbations, leading to challenges in determining average flow fields without artificial vortex diffusion caused by averaging flow fields with different vortex positions. To address this, Heineck et al. (2000) used the instantaneous vortex positions both for quantifying vortex wandering and for transforming the instantaneous field

data into a vortex coordinate system. This approach minimized the effects of vortex wandering in averaged flow fields, allowing for the extraction of vortex properties such as swirl velocity, core radius, and vorticity from the averaged flow field. A more detailed study on the wandering behavior of young vortices was done by Mula et al. (2013), who identified preferred wandering axes orthogonal to the vortex trajectory.

Since conventional Stereo-PIV does not capture derivatives of the out-of-plane velocity components, Ramasamy et al. (2009) used a dual-plane Stereo-PIV approach, allowing for the measurement of all nine components of the velocity gradient tensor. This enabled the investigation of turbulence inside the vortices, revealing significant anisotropy in its components. Despite the valuable insights gained, dual-plane PIV measurements require substantially more effort, compared to Stereo-PIV approaches and have therefore been applied in only a limited number of experiments.

One of the most comprehensive and resource-intensive hover rotor experiments to date was recently conducted by NASA within the U.S. Air Force National Full-Scale Aerodynamics Complex (NFAC) 80- by 120-Foot Wind Tunnel. As part of the Hover Validation and Acoustic Baseline (HVAB) program, a four-bladed rotor with a radius of 1.69 m was tested, with its geometry openly available for reference and comparisons with CFD results. A wide range of measurement techniques was employed to capture key aerodynamic phenomena. One blade was equipped with 187 unsteady pressure transducers, while photogrammetry using retroreflective markers on the lower blade surfaces provided deformation measurements. Infrared thermography was used to detect boundary layer transition, see Norman et al. (2023). The rotor wake was characterized using Shadowgraphy and Stereo-PIV (FOV: approximately  $1.2 R \times 0.5 R$ ), with Shadowgraphy providing precise tip vortex tracking and PIV, offering detailed insights into the wake flow field, including velocity distributions and vortex evolution, see Ramasamy et al. (2024).

Model rotor experiments mostly lack Reynolds number similarity with full-scale helicopters. Consequently, PIV has also been applied to full-scale helicopters. These experiments pose challenges, due to strict legal regulations regarding outdoor laser usage, the need for high laser power to illuminate large FOVs and demanding seeding requirements. As a result, such experiments remain rare, but a few successful applications exist. The first full-scale helicopter PIV application was conducted by Raffel et al. (2001), who applied it to a BO105 helicopter in simulated hover flight in ground effect. Using a two-component PIV setup and a relatively small FOV of approximately  $100 \text{ mm} \times 150 \text{ mm}$ , high-quality vortex velocity measurements were achieved. However, due to the limited FOV, these measurements were restricted to ground-fixed helicopter tests and young vortex ages. Kindler et al. (2009) demonstrated, using a similar setup, that blade tip vortex velocity profiles closely matched with the Vatistas vortex model. An example of PIV measurements on a free-flying helicopter was provided by Schwarz (2020), measuring outwash velocity while the helicopter flew at different blade tip heights between  $0.81 R$  and  $1.21 R$ . PIV measurements captured not only mean outwash but also older vortices. Schwarz (2020) showed that the PIV measured vortex positions were in good agreement with data obtained using Background-Oriented Schlieren (BOS) techniques.

#### 3.1.2. Particle Image Velocimetry (PIV)

The use of optical measurement techniques by tracking particles added to a flow dates back to the early days of fluid dynamics. One of the earliest examples of flow visualization with smoke was conducted by Mach (1896). He used cigarette smoke to qualitatively observe streamlines around a flat plate with airflow perpendicular to the surface. Similarly, Ahlborn (1902) carried out experiments in a water tank, where he moved a flat plate through water seeded with clubmoss flakes.

Ahlborn's work was particularly innovative as he installed a mechanical trigger for the illumination and measured the duration of the light exposure. This allowed him to capture instantaneous flow fields at specific moments and determine velocities by measuring the length of the illuminated light streaks that appeared. Another significant advancement made by Ahlborn (1902) was the selection of distinguishable seeding particles, which enabled quantitative measurements. His work laid the foundation for particle image photography as a method for flow field measurements, although it remained labor-intensive at that time.

The breakthrough in Particle Image Velocimetry (PIV) for a wider field of applications came with the use of powerful lasers and LEDs for flow field illumination, combined with the advent of digital image recording. The integration of these technologies provided a significant advantage: it enabled measurements at two successive points in time, with each image stored separately. This capability allows the measurement of flow fields with reverse flow, as time stamps can be associated with each image. Furthermore, digital post-processing enables automation of the correlation approach for evaluating image data, thereby making the reconstruction of reliable flow fields more efficient. Another key benefit of digital processing is the ability to apply more complex evaluation algorithms, which enhance the accuracy of the measurements, see Raffel et al. (2018).

These advances form the basis of the modern PIV technique. To provide context for the subsequent discussion, the typical working principle of PIV is illustrated in Fig. 3.1. In this method, the flow, seeded with tracer particles, is illuminated by two successive laser light pulses. PIV double pulse lasers usually consist of two individual lasers combined within a single housing, where their beams are merged to form a common output beam. Laser light sheet optics use a cylindrical lens to shape and widen the beam, combined with a spherical telescope to adjust the light sheet thickness.

As the particles are illuminated, they scatter or reflect light, depending on their size. This light is captured by a camera at two distinct time instances,  $t_0$  and  $t_0 + \Delta t$ . The images captured in the image plane are then divided into interrogation windows, typically ranging in size from  $8 \text{ px} \times 8 \text{ px}$  to  $128 \text{ px} \times 128 \text{ px}$ . Cross-correlation is applied between the corresponding interrogation windows from the two time steps to determine the average pixel shift within each window. This shift in the image plane is then multiplied by the optical magnification scale of the camera lenses,  $M$ , yielding the particle displacement  $X$  in the FOV. Dividing by  $\Delta t$  gives the velocity:

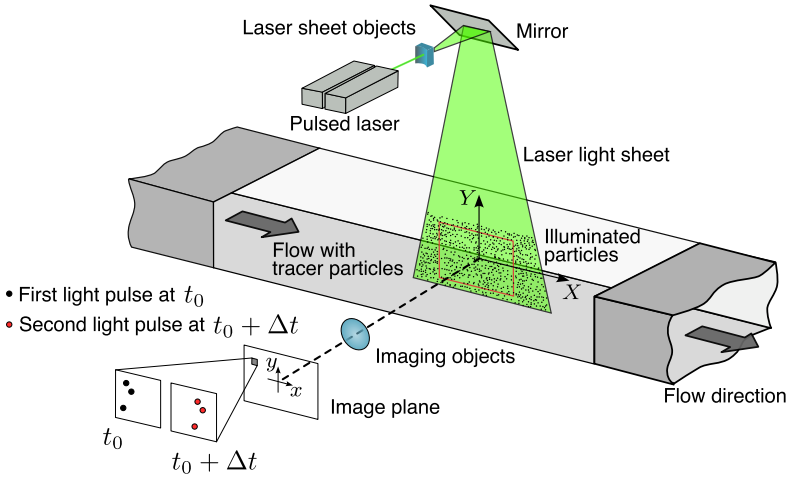


**Figure 3.1.:** Particle Image Velocimetry principle, after Raffel et al. (2018)

$$u = \frac{\Delta x \cdot M}{\Delta t} = \frac{\Delta X}{\Delta t} \quad (3.1)$$

The magnification factor  $M$  can be determined by recording an image with a calibration target at the light sheet's position and dividing the pixel shift by the corresponding length. Note that this procedure does not account for distortions in the optical system.

More advanced multi-pass correlation methods improve the accuracy of PIV by using an iterative refinement of the interrogation window size. In the first pass, larger interrogation windows are used to capture the overall mean flow field. Larger windows benefit from more data, yielding higher correlation values, but they lack spatial resolution. To address this limitation, subsequent passes are conducted using smaller interrogation windows. The information from the first pass is utilized to adapt these smaller windows to account for the mean flow gradient, improving the accuracy, particularly in regions with high flow gradients, see Soria (1996). To further enhance spatial resolution, the interrogation windows can be overlapped during post-processing. For example, an overlap of 75% can increase the number of data points by a factor of 16, leading to a more detailed flow field analysis.

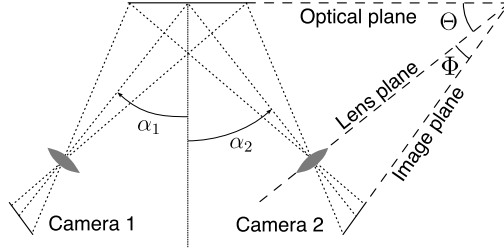


**Figure 3.2.:** Stereoscopic PIV configuration with Scheimpflug condition (see also Scheimpflug (1904)) and camera angles in the  $XZ$ -plane, after Bauknecht (2016)

### Stereoscopic Particle Image Velocimetry

Two-dimensional PIV (2D2C) only delivers the in-plane velocity components. For larger FOVs the problem arises that the optical axis is not always perpendicular to the imaging plane, leading to measurement errors where out-of-plane velocity is incorrectly assigned to the in-plane velocity components. To address these limitations, Stereoscopic Particle Image Velocimetry (2D3C), also known as Stereo-PIV, additionally enables the measurement of the out-of-plane velocity component. To gather the additional information needed, a second camera is added. For an opening angle of  $90^\circ$  all three velocity components can be determined with equal accuracy, see Gaydon et al. (1997).

In contrast to a PIV setup in which the optical axis is perpendicular to the image plane, a Stereo-PIV setup features non-parallel image and optical planes. This results in unsharp parts of the FOV for conventional camera lens setups. A patent by Scheimpflug (1904) solves this problem by tilting image and lens plane to each other, causing a sharp image on the image plane. Such a PIV setup is shown in Fig. 3.2. For Stereo-PIV cameras Scheimpflug adapters are used, which enable for the tilting of both image axes, fulfilling the Scheimpflug criterion.

The pixel shift in the image plane now also includes a significant out-of-plane component, as shown in Fig. 3.3

$$d_x = x'_i - x_i = -M(D_x + D_z x'_i / z_0) \quad (3.2)$$

$$d_y = y'_i - y_i = -M(D_y + D_z y'_i / z_0) \quad (3.3)$$

where  $M = z_0/Z_0$  is the magnification factor and  $\mathbf{D}$  represents the particle displacement during  $\Delta t$ . Knowing the camera angles from the calibration provides the camera angle  $\alpha$  in the

$XZ$  plane (as shown in Fig. 3.2) and analogously  $\beta$  in the  $YZ$  plane. This information results in a system of equations describing all three velocity components:

$$u = \frac{u_1 \tan \alpha_2 + u_2 \tan \alpha_1}{\tan \alpha_1 + \tan \alpha_2} \quad (3.4)$$

$$v = \frac{v_1 \tan \beta_2 + v_2 \tan \beta_1}{\tan \beta_1 + \tan \beta_2} \quad (3.5)$$

$$w = \frac{u_1 - u_2}{\tan \alpha_1 + \tan \alpha_2} = \frac{v_1 - v_2}{\tan \beta_1 + \tan \beta_2} \quad (3.6)$$

However, a closer look shows that with three unknown parameters and four equations, the system is overdetermined and must be solved iteratively. In addition, the denominator of the equation can approach zero for values of  $\beta \approx 0$ , making the system mathematically undefinable. Therefore, a setup with non-collinear camera viewing angles is required, see Raffel et al. (2018).

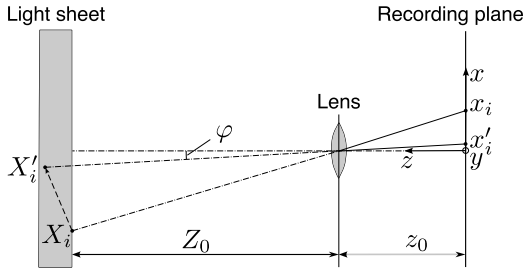


**Figure 3.3.:** Particle displacement, including the out-of-plane component, and the corresponding image mapping (adapted from Raffel et al. (2018)).

## Calibration

For PIV setups with significant image distortions (mostly common for large FOVs), or non-perpendicular camera arrangements, a calibration is required to map each pixel in the image plane to a spatial position in the flow field. Calibration plates placed inside the FOV are used for this purpose. These plates range from 2D dot patterns or checkerboards to precision-milled, dual-level targets for Stereo-PIV.

In the present experiments, double-sided, dual-level calibration targets (LaVision Types 31 and 309-12) were used. An average of 100 images per camera was computed and supplied to

the DaVis calibration routine. This routine offers two classes of calibration models: empirical methods and physics-based approaches.

Empirical methods typically employ polynomial functions (e.g., the third-order polynomial approach proposed by Soloff et al. (1997)) to reconstruct the imaging geometry. Their main drawback is reduced accuracy when the calibration target does not span the entire FOV, due to their undefined and potentially erroneous extrapolation behavior. Physics-based models, in contrast, yield a calibration function that remains valid across the full FOV—an important advantage when working with large FOVs because it removes the need for bulky calibration targets.

For that reason, the physically based pinhole model was used, which assumes that all light rays pass through a single point. Real lenses, however, have finite apertures that cause distortions and therefore require corrections. Such a corrected pinhole model is, e.g., given by Tsai (1987), see Willert (2006).

To mitigate an error caused by a misalignment between calibration target and the light sheet, Wieneke (2005) developed a self-calibration scheme that cross-correlates the dewarped images from all cameras to create a disparity map. This map is then used to refine the calibration parameters, thereby reducing systematic errors.

## Tracer Particles

PIV is an indirect flow measurement method and dependent on the physical particle behavior in the flow and their optical visibility. The particle behavior is influenced by several factors which are shortly summarized in the following.

Measurements in gas flows are often challenging due to the higher density of tracer particles compared to the surrounding fluid. An exception are neutrally buoyant particles, such as helium-filled soap bubbles (HFSB), which are not considered further here due to their relatively large size (typically around 100  $\mu\text{m}$ ).

The influence of gravity on the sink velocity can be described by Stokes' law as

$$V_g = d_p^2 g \frac{\rho_p - \rho}{18\mu} \quad (3.7)$$

where  $d_p$  is the particle diameter,  $g$  is gravitation and  $\mu$  the dynamic viscosity. For a flow field with constant acceleration, the velocity lag  $V_s$  can be expressed as:

$$V_s = d_p^2 a \frac{\rho_p - \rho}{18\mu} \quad (3.8)$$

According to this relationship, the smaller the tracer particle diameter, the smaller the

resulting velocity lag, see Raffel et al. (2018).

Unfortunately, the demand for the smallest possible tracer particles conflicts with the need for good particle visibility. This conflict imposes strict technical demands on both the measurement equipment and the overall PIV setup. High-energy lasers and high-resolution, light sensitive cameras are therefore essential. Smaller FOVs, e.g., allow for less beam widening and thus more light intensity. The arrangement of the cameras also influences the captured light from small tracer particles.

Unlike large particles, which primarily reflect light, smaller particles scatter it. The normalized size parameter

$$q_p = \frac{\pi d_p}{\lambda_w} \quad (3.9)$$

is the decisive criterion distinguishing the scattering regimes. When  $q \ll 1$ , Rayleigh scattering is the dominant scattering mechanism. For macro-PIV experiments, the most important mechanism is Mie scattering (first described by Mie (1908)), which occurs for particles in the range  $0.2 < q < 2000$ . This interval encompasses all tracer sizes used in the present experiments. The highly directional-dependent Mie scattering behavior of an oil drop with a diameter of  $1 \mu\text{m}$  is shown in Fig. 3.4.

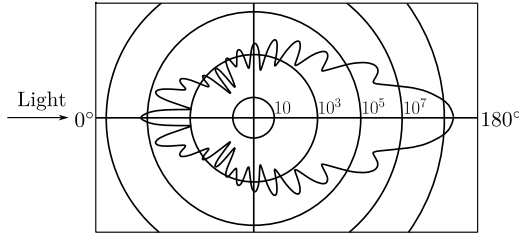


**Figure 3.4.:** Mie scattering of an  $1 \mu\text{m}$  oil drop, after Raffel et al. (2018)

The setup can take advantage from the Mie scattering by pointing the camera viewing direction against the direction of light (“forward scattering”, between  $90^\circ$  and  $180^\circ$  degree) rather than looking in the same direction.

The particle image diameter is mainly determined by the magnification factor  $M$  and the diffraction limit

$$d_{\text{diff}} = 2.44 f_{\#} (1 + M) \lambda. \quad (3.10)$$

For small particles, the diffraction limit sets a lower bound for the particle image size, since it depends not on the particle size but on the optical aperture. A larger aperture, e.g., increases brightness because light intensity is inversely proportional to the square of the  $f$ -number, but it simultaneously reduces the apparent particle image diameter. For larger particles, however,

### 3. Experimental Setup

---

$M \cdot d_p$  becomes linearly larger than the diffraction limit. Assuming an ideal lens both parameters are included in an approximate particle diameter:

$$d_\tau = \sqrt{(Md_p)^2 + [2.44f_\#(1+M)\lambda]^2} \quad (3.11)$$

Given that the magnification factors used in the optical setups range from 0.053 to 0.183 and the particle size is below 5  $\mu\text{m}$ , the diffraction limit dominates the particle image size. However, measurements with real lenses, result in deviations from the theoretical values, primarily due to lens aberrations and the reduction in light intensity with increasing the f-number, especially for large apertures, as shown by Raffel et al. (2018). Cameras exhibit a characteristic noise level that the particle signal must exceed. Increasing  $f_\#$  by one stop reduces the light intensity by half, causing a smaller portion of the Gaussian intensity profile to exceed the signal-to-noise threshold. According to measurements by Raffel et al. (2018), this effect compensates for the increased particle image diameter predicted by Eq. 3.11.

In the present experiments, the aperture was selected such that all particles within the FOV were sharply imaged. Due to lens aberrations the aperture for all setups was closed to  $f_\# = 2.8$ , to ensure sharpness throughout the FOV.

In vortex flows, two detrimental seeding effects must be considered. First, tracer particles that are denser than the surrounding medium experience a centrifugal force, which drives them radially outward and produces a seeding void in the vortex center. Second, the rotation of the particles generates a Magnus force that deflects their trajectories away from the core. Both mechanisms reduce tracer density precisely where velocity gradients are highest, thereby limiting PIV measurements to the outer regions of the vortex.

Using smaller particles mitigates this limitation, because centrifugal acceleration scales with particle mass, leading to a smaller vortex void. Ongoing advances in laser power further support the use of smaller tracers by ensuring sufficient light scattering. A detailed discussion of how these effects were addressed during data reduction, as well as the criteria for accepting or rejecting individual vortex measurements, is provided in Chap. 4.1.2.

## 3.2. Hover Test Stand

The experiments discussed in this thesis were conducted at the Hover Test Stand (HVG) of the German Aerospace Center in Göttingen, illustrated in Fig. 3.5. It is designed to investigate the aerodynamics of an isolated rotor in hover out of ground effect, facilitating a good comparability with numerical methods. This is particularly useful for a detailed comparison of vortex decomposition.

The rotor was mounted on a solid support structure with a built-in electric traverse system, allowing for height adjustments of the rotor plane. This enabled measurements at different axial distances from the rotor without modifying the PIV setup. To adjust the tip vortex spacing, the blade hub allowed to vary the blade number to one-, two- and four-blade configurations. The traverse system was covered by a housing with a diameter of 350 mm and was sealed with a circular cover directly beneath the rotor. For the one-blade cases, a cylindrical counterweight, approximately 12 cm long, was mounted on the opposite side to compensate for the imbalance of the blade.

The rotor of the test stand was powered by a brushless motor (*ALIGN DOMINATOR RCM-BL850MX*) that provided a continuous power of up to 5.1 kW. Because the motor was originally designed for model helicopters, which benefit from stronger airflow than the enclosed housing provides, an auxiliary cooling package, consisting of a fan and water cooling pipes mounted near the stator, was added.

The motor drove a gearbox to achieve the required rotation frequency. Rotor phase information was obtained by a 256-step encoder coupled to the shaft via a toothed belt. To measure

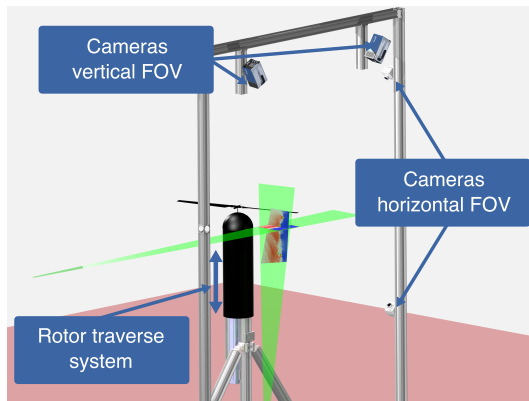


**Figure 3.5.:** Sketch of the hover test stand with PIV planes

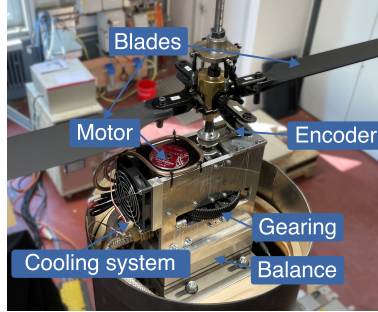


**Figure 3.6.:** Rotor propulsion system, encoder, and balance integration

aerodynamic loads, a six-component piezoelectric balance was installed directly beneath the propulsion assembly, providing simultaneous measurements of force and torque. The complete propulsion system is shown in Fig. 3.6.

### 3.2.1. Test Rotor and Parameters

The rotor plane was between 3.1 m (4.1  $R$ ) and 3.67 m (4.8  $R$ ) above the ground, depending on the traverse height<sup>1</sup>. In reference conditions, the rotor frequency was set to  $f = 18.86$  Hz or  $\Omega = 118.5$  s<sup>-1</sup>, respectively. The blade pitch was adjusted for a blade loading of  $C_T/\sigma = 0.085$ , resulting in a rotor thrust of about  $T = 40$  N for the one-bladed case up to about 160 N for the four-bladed case. For the two- and four-blade cases a variation of the blade-to-blade pitch offset was done. For the two-blade case it is defined as the difference between the blade pitch angles

$$\Delta\theta = \theta_{\text{Blade 2}} - \theta_{\text{Blade 1}} \quad (3.12)$$

The pitch offset for four-blade case is defined as the average difference between the pitch angles of two successive blades

$$\Delta\theta = \frac{\theta_{\text{Blade 2}} - \theta_{\text{Blade 1}} + \theta_{\text{Blade 4}} - \theta_{\text{Blade 3}}}{2}, \quad \theta_{\text{Blade 1,3}} \approx \theta_{\text{Blade 2,4}}. \quad (3.13)$$

An additional parameter variation covers different blade loadings  $C_T/\sigma$  at constant rotor frequency  $f$ , and different rotor frequencies at constant blade loading, see Tab. 3.1.

<sup>1</sup>A discussion about the influence of ground effect is available in Chap. 3.2.2

**Table 3.1.:** Operating conditions

$N_b$	Rotation frequency $f$	Blade loading $C_T/\sigma$	Offset $\Delta\theta$
1	$f = 18.86 \text{ Hz}, \sqrt{2}f, f/\sqrt{2}, f/2$	$0.059, 0.071, 0.085 \pm 0.05,$ $0.098, 0.106$	—
2	$f = 18.86 \text{ Hz}, \sqrt{2}f, f/\sqrt{2}, f/2$	$0.085 \pm 0.05$	$0^\circ, 0.2^\circ, 0.5^\circ, 1^\circ$
4	$f = 18.86 \text{ Hz}$	$0.085 \pm 0.05$	$0^\circ, 1^\circ$

In addition to the operational parameters, the rotor blade design has a large impact on the behavior of blade tip vortices. For this reason, the blade geometry was varied and its effect on vortex decay is discussed in Chap. 6. The different geometries are presented in Fig. 3.7.

To increase the comparability with previous measurements, most test cases were performed with the SpinBlades BlackBelt 685 rotor blades, which were also used in the experimental and numerical studies of Wolf et al. (2019b), Schwarz et al. (2022) and Bodling et al. (2023). The SpinBlades are commercially available and use a proprietary but symmetrical airfoil and a parabolic tip shape. The chord length is  $c = 61 \text{ mm}$  and the span is  $685 \text{ mm}$ , which together with the rotor hub gives a rotor radius of  $R = 760 \text{ mm}$ . The SpinBlades were used to investigate the effect of different numbers of blades ( $N_b = 1, 2, 4$ ). Figure 3.8a presents the corresponding radial distributions of bound circulation, obtained from simulations with the Unsteady Panel Method (UPM). The influence of the blade number on tip losses is clearly visible, as indicated by an increased maximum bound circulation and a radial outward shift of the circulation peak towards the blade tip.

To additionally analyze the effect of blade twist, the ‘DLR-HEL’ design was introduced. The chord length and radius of the SpinBlades were kept, but the airfoil was changed to a NACA

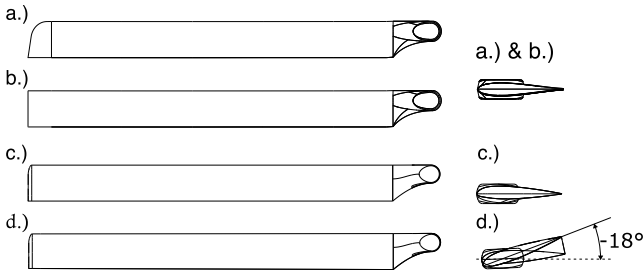


**Figure 3.7.:** Rotor blade types: a) SpinBlades BlackBelt, parabolic blade tip, b) SpinBlades BlackBelt, rectangular blade tip, c) DLR-HEL-0 and d) DLR-HEL-18

23015<sup>2</sup> geometry, and a rectangular tip shape was used. A highly twisted blade (18° (linear)) was compared to an untwisted blade (0°). Figure 3.8b shows the influence of rotor design on the lift distributions for a one-bladed rotor, simulated with UPM. As a result, the influence of twist is clearly seen. The circulation of the twisted blade is nearly elliptical and approaching the ideal distribution for hover. This results in variations in tip vortex strength and downwash velocities, enabling the investigation of their influence on the vortex decay.

### 3.2.2. Validation of Thrust Measurements

With the test setup complete, two validation steps were performed to verify the general configuration. First, thrust measurements were conducted at various pitch angles to ensure that the system produced reasonable results. Figure 3.9a shows that the measured thrust coefficients for one- and two bladed SpinBlades configurations agree well with thrust predictions from a simple blade element method (BEM). For all other configurations only a small pitch angle variation within the target operating range was applied.

To show that the distance between rotor and ground or the distance between rotor and ceiling, respectively, have a negligible influence on the measurement results, the normalized thrust for each measured point at each traverse height is plotted in Fig. 3.9b. Although a small trend of thrust increase with a higher rotor position is evident, this influence remains below 2%.

<sup>2</sup>A thicker version of the NACA23012, which is used for the rotor Blades of the MBB BO105 helicopter

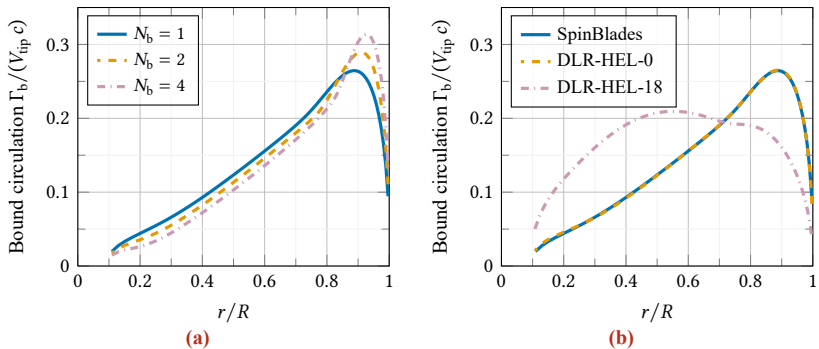


**Figure 3.8.:** Free-wake (UPM) calculations to visualize the influence of: a) Blade number, b) Blade design

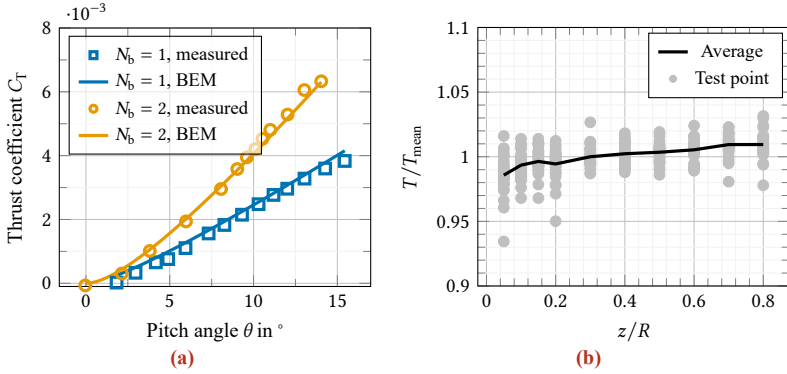


**Figure 3.9.:** Rotor thrust measurements: a) Thrust coefficient against pitch angle for one- and two blade configuration and SpinBlades blades, b) Normalized thrust of all test points (average over the measurement) with different blades and different ground clearances against rotor traverse height

### 3.2.3. PIV Setups

Stereo Particle Image Velocimetry (Stereo-PIV) was selected as the primary measurement technique for this study. The use of three-dimensional particle-tracking methods, such as those used by Wolf et al. (2019b) and Schröder et al. (2023), was evaluated, but the current spatial resolution of these methods in air is lower than that of Stereo-PIV. This limitation arises from the larger tracer particles required in air, which creates voids in vortex cores (Magnus effect), and from the low density of trackable particles that constrains resolution.

Because this research aims to resolve comparatively small secondary vortex structures and to characterize blade tip vortices, minimizing particle void size is essential. Stereo-PIV therefore offers a good compromise between measurement dimensionality and spatial resolution, providing all three velocity components in a well-resolved measurement plane.

To capture both the primary blade tip vortices and the secondary vortex system, two mutually perpendicular Stereo-PIV planes, approximately normal to the respective vortex axes, were employed. To ensure proper alignment of the laser sheets relative to each other these targets were also used to adjust the light sheet orientation correctly, as shown in Fig. 3.10 for the adjustment of the horizontal light sheet with respect to the vertical calibration plate.

Figure 3.11a provides a top-view schematic of the test stand, showing the positions of all cameras for both PIV planes, the laser sources, and the rotor. Figure 3.11b highlights the high- and low-speed fields of view, illustrating how the two measurement planes intersect the rotor wake and overlap in space. Together, the graphics clarify the spatial orientation of each

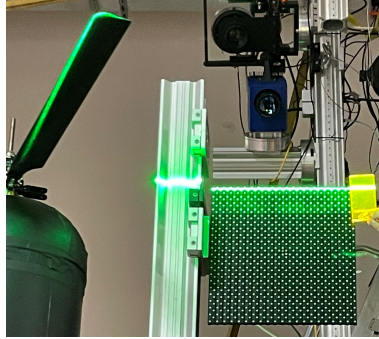


**Figure 3.10.:** Alignment of the vertical calibration plate to the horizontal light sheet.

measurement volume and the rationale for the two-plane setup.

In addition to these measurements, four cases were only investigated in the vertical plane. For these cases the FOV sizes were significantly reduced, and smaller seeding particles were generated (details of the seeding will be discussed in Chap. 3.3.2). This allows a detailed insight into vortex properties, such as maximum tangential velocities and vortex core radii.

The following sections describe each setup in detail and outline the timing strategy used to synchronize the high-speed horizontal system with the low-speed vertical system.

The timing of each system in relation to the other is shown in Fig. 3.12. In each measurement cycle, the high-speed system takes 50 images during on rotor revolution, while the low-speed system takes 10 images over 20 rotor revolutions. All cycles are characterized by a common start at a rotor position, which is defined as  $\psi = 0^\circ$  rotor azimuth. The further recordings in

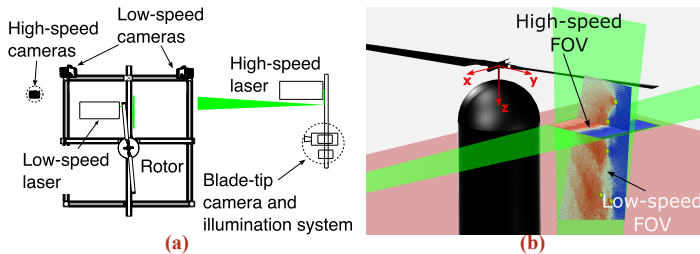


**Figure 3.11.:** Sketches of the measurement systems: a) Top-down view of the test stand and measurement devices, b) PIV fields of view (FOV)

each measurement cycle are then performed with the respective recording frequencies (950 Hz for the high-speed system, 10 Hz for the low-speed system). For the horizontal high-speed PIV system this means to record 50 images during one rotation. The vertical low-speed system records an image every second rotation including a phase shift of  $1/10$  rev. to gain 10 images at 10 different azimuthal positions. When the previous cycle has finished, the system waits until the rotor position reaches  $\psi = 0^\circ$  again and restarts both systems at the same rotor position.

### Secondary Vortex Measurements

For the horizontal plane, a high-speed PIV system was used, to allow a time-resolved and statistical evaluation of the secondary vortex structures. It consists of a camera system (two Phantom VEO640L, with 130 mm focal-length lenses and a resolution of  $2048 \times 1400$  px) and a high-speed laser. The laser has an energy output of  $26 \text{ mJ pulse}^{-1}$  and a time delay between the PIV double frames between  $\Delta t = 30 \mu\text{s}$  and  $\Delta t = 50 \mu\text{s}$ , depending on the expected hover induced velocity. A PIVcts1000 seeding device containing di-ethyl-hexyl-sebacate (DEHS) was used for particle seeding, filling the entire test laboratory with oil droplets. To achieve a homogeneous seeding, the rotor was used to distribute the particles after each seeding run.

The resulting FOV has a size of about  $0.4 R \times 0.4 R$  and a pixel size of  $0.14 \text{ mm}$  corresponding to  $6.93 \text{ px mm}^{-1}$ . An acquisition frequency of 950 Hz was used, to acquire 50 images per measurement cycle. This corresponds to a measurement cycle duration of  $1/19 \text{ s}$  or the time of one full rotor revolution at the reference rotation frequency.

The chosen acquisition frequency leads to an azimuth increment of  $7.2^\circ$  between consecutive

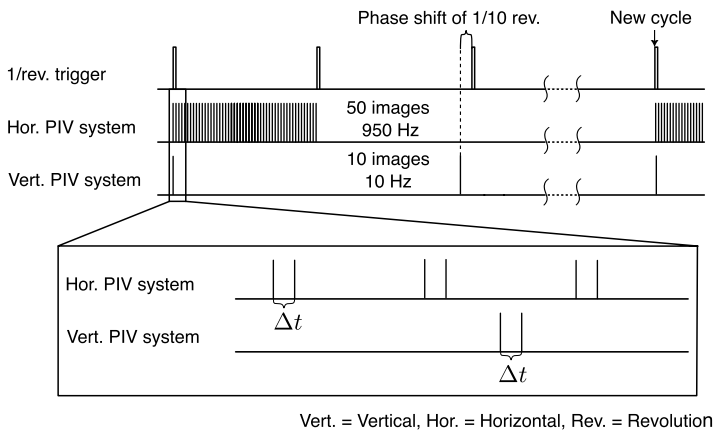


**Figure 3.12.:** PIV timing diagram

images at the reference rotation frequency, while the FOV covers an azimuthal range of  $22.5^\circ$  in space. Consequently, each measurement cycle provides a full temporal phase coverage (one revolution) and simultaneously accumulates  $1125^\circ$  of spatial azimuth coverage due to image overlap. For cases with reduced rotation frequency, the number of recorded images was increased, to maintain full azimuthal coverage. To measure at different vortex ages using fixed PIV planes, the rotor was traversed vertically, resulting in FOV positions ranging from  $z/R = 0.05$  to  $z/R = 0.8$  below the rotor plane.

#### **Blade Tip Vortex Measurements (Overview)**

In addition, a low-speed PIV system was used to measure the primary blade tip vortices and the overall wake structure. Since both measurements were conducted simultaneously, the same seeding parameters as in the previously described experiment were used. The location of the low-speed FOV and the camera positions are sketched in Fig. 3.11a and Fig. 3.11b. For imaging two pco DIMAX S4 cameras with a resolution of  $2024 \times 2024$  px, equipped with 85 mm focal-length lenses were used. This results a FOV with a height of about  $0.9 R$  and a width of between  $0.46 R$  at the top and  $0.72 R$  at the bottom. Accordingly, an average spatial resolution of  $4.85 \text{ px mm}^{-1}$  was achieved. For illumination, a low-speed laser with a pulse energy of about  $200 \text{ mJ pulse}^{-1}$  was used. The time delay  $\Delta t$  was set to between  $\Delta t = 50 \text{ }\mu\text{s}$  and  $\Delta t = 70 \text{ }\mu\text{s}$  depending on the expected hover induced velocity for each case. The low-speed system acquired 10 images per measurement cycle with an acquisition frequency of 10 Hz. Combined with the rotation frequency of approximately 19 Hz, this results in 50 images at each of ten different rotor phase positions.

#### **Blade Tip Vortex Characterization**

In a subsequent experiment four configurations were investigated using smaller vertical FOVs, without measuring secondary vortices. As a result, a smaller laser sheet was used, allowing the use of smaller particles. This offers the advantage of reducing particle voids and thereby enabled the investigation of vortex core size and maximum swirl velocity, parameters that could not be evaluated with the larger FOV.

The setup of these measurements is similar to the previous vertical PIV investigations, and therefore only the modifications are described here. The focal length of the lenses was changed to 180 mm to increase the image magnification while maintaining the camera positions. Instead of the PIVcts1000, a Laskin seeding device was used to achieve smaller seeding particles. Their influence on particle velocity lag is discussed in Chap. 3.3.2.

The reduction in FOV size resulted in a lower spatial coverage of the vortex trajectory. The step width of the rotor traverse system in axial direction ( $z$ -axis) was easy to adjust to account for the smaller coverage. The radial coverage of both young and older vortices, however,

**Table 3.2.:** Field of views for detailed vertical PIV investigations

Field of view	Spatial resolution	Size
FOV1	16.68 px mm <sup>-1</sup>	0.18 R × 0.21 R
FOV2	15.70 px mm <sup>-1</sup>	0.20 R × 0.24 R
FOV3	13.63 px mm <sup>-1</sup>	0.24 R × 0.29 R

required the use of three radially shifted FOVs, which increased the overall setup time. An overview of spatial resolution and size of the FOVs used is given in Tab. 3.2.

### 3.3. Validation and Uncertainty Analysis of the PIV Measurements

PIV measurements are influenced by various factors, not all of which can be quantified through error propagation. However, a rough approximation and discussion of the most common measurement errors remain reasonable here. According to Lazar et al. (2010), the errors in a PIV systems can be divided into the following groups:

- Equipment related errors
- Particle behavior
- Sampling uncertainty
- Processing algorithm errors

The resulting error of each source is derived by an error propagation analysis providing an estimate of the total measurement uncertainty. Assuming that the uncertainties associated with each error source are normally distributed and that all errors are statistically independent, the Gaussian error propagation method for the velocity  $V$  yields a valid estimate of the 95 % confidence interval bounds:

$$E_{0.95,V} = \sqrt{\sum_{m=1}^M \left( \frac{\partial V}{\partial P_m} E_{0.95,P_m} \right)^2} \quad (3.14)$$

The individual contribution of parameter  $P_m$  is given by the confidence bound of this parameter, multiplied by the sensitivity of the measurement result to this parameter. The total confidence bound is then the square root of the sum of squared individual contributions.

### 3.3.1. Equipment Related Errors

#### Timing Error

Since the camera's exposure time is significantly longer than the laser pulse duration, the timing accuracy is primarily defined by the laser. In practice, however, the laser pulse does not perfectly align with the rising edge of the trigger signal but exhibits some jitter. While high-speed Nd:YLF lasers typically have negligible jitter, lower-speed lasers, such as the Quantel Twins Q-smart used in this study, exhibit slightly higher jitter, though it remains below 1 ns.

For the cases where a time delay of  $\Delta t = 7 \mu\text{s}$  was used the resulting timing error remains below 0.015%. In most cases, however,  $\Delta t$  ranges between  $30 \mu\text{s}$  and  $50 \mu\text{s}$  which further reduces this error. In addition to the jitter the illumination length, also set by the lasers used, introduces an error. The Nd:YAG laser has a pulse duration of less than 5.8 ns, whereas the high-speed Nd:YLF laser has 150 ns.

For the high-speed system, where the minimal  $\Delta t$  used is  $30 \mu\text{s}$ , this results in a maximum error of about 0.5%. For the low-speed laser, using  $\Delta t = 7 \mu\text{s}$ , the maximum error is 0.0843%, including the previously discussed influence of jitter. The contributions of the individual timing errors are summarized in Tab. 3.3.

**Table 3.3.:** Timing error calculation for all PIV systems

Error source	Vertical PIV $f$	Horizontal PIV
Timing unit jitter	< 1 ns	< 1 ns
Laser jitter	< 1 ns	–
Pulse duration	5.8 ns	150 ns
Minimum $\Delta t_{\min}$	$\Delta t = 7 \mu\text{s}$	$30 \mu\text{s}$
Maximum relative error $\left( \sqrt{\sum_1^M E^2} / \Delta t_{\min} \right)$	0.085%	0.5%

#### Calibration Error

Calibration uncertainties arise from four main sources: fitting error of the camera model, inaccuracies of the calibration target, shadows, or glare points causing false or uncertain point detection, and the alignment of the calibration target with the light sheet. The last source of error can be effectively eliminated using self-calibration, as described in Chap. 3.1.2, which compensates for a possible misalignment. During the calibration imaging process, two LED flood lamps and a long exposure time are used to produce glare point and shadow free, and brightly illuminated images of the calibration target.

In a next step the error due to imperfections of the calibration target is addressed. According to the manufacturer, it has a positional accuracy of  $\pm 50 \mu\text{m}$ , which contributes to the overall uncertainty by:

$$E_{\text{target},0.95,V} = \frac{E_{\text{target},0.95}}{\Delta x} \frac{100 \mu\text{m}}{15 \text{mm}} = 0.33\%. \quad (3.15)$$

For the calibration a pinhole model is used, because the calibration target does not always cover the entire image, which requires an extrapolation that is more accurately handled by the pinhole model than by polynomial approaches. As part of this calibration process, DaVis returns the standard deviation of this fit. The relative error for a plain target can be calculated, knowing the distance of between neighboring points, by

$$E_{\text{cal},0.95,V} = \frac{1.96 \cdot E_{\text{cal},0.68}}{\Delta x} \quad (3.16)$$

However, in a dewarped image corrected along all axes, the scaling factor becomes strongly direction-dependent. As a result, a given pixel error translates into varying physical errors depending on the orientation. To avoid overly complex formulations, the approximation proposed by Wolf (2014) was adopted. In this approach, the smallest effective  $\Delta x$  is used, corresponding to the maximum possible error and thus providing a conservative estimate, when a maximum tilt angle of  $45^\circ$  is assumed:

$$E_{\text{cal},0.95,V} = \frac{\sqrt{2} \cdot 1.96 \cdot E_{\text{cal},0.68}}{\Delta x} \quad (3.17)$$

This equation is used to calculate the relative uncertainty for each FOV, as shown in Tab. 3.4.

**Table 3.4.:** Calibration error calculation for each FOV

Field of view	Fit error $E_{\text{fit},0.68}$	Relative uncertainty $\sqrt{E_{\text{cal},0.95,V}^2 + E_{\text{target},0.95,V}^2}$
Vertical FOV, large	0.026 mm	0.59%
Vertical FOV1, small	0.045 mm	0.89%
Vertical FOV2, small	0.037 mm	0.76%
Vertical FOV3, small	0.057 mm	1.10%
Horizontal FOV	0.010 mm	0.38%

### 3.3.2. Particle Behavior

The behavior of small particles in a flow has already been discussed in Chap. 3.1.2. In this section, a quantitative assessment of the uncertainty effects associated with all employed PIV

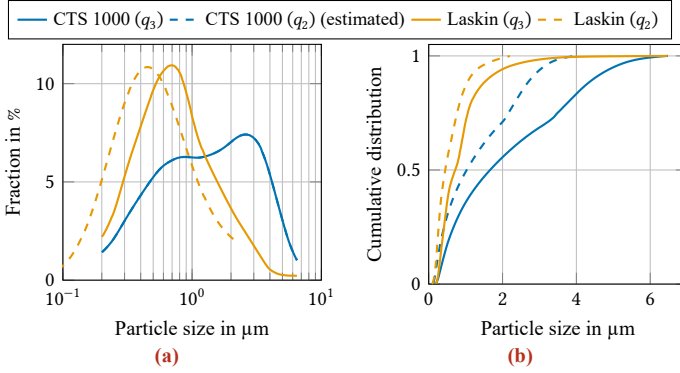


**Figure 3.13.:** Frequency (a) and cumulative (b) volumetric particle size distributions ( $q_3$ ), based on values from Raffel et al. (2018)

setups is made. Birch et al. (2013) propose a methodology to predict tracer particle transport in vortex flows, which is widely used to quantify uncertainties in blade tip vortex flows, see e.g., Schwarz (2020) or Bauknecht (2016).

Using the methodology of Birch et al. (2013) the error can be quantified by:

$$E_{\text{particle}} = 2 \cdot (\alpha_L^2 + 0.5)^2 \left( \frac{V_{\theta, \max} \rho_p d_p^2}{18 \nu \rho_\infty r_c} \right)^2 \quad (3.18)$$

The requirement to know the true value for  $V_{\theta, \max}$  can be satisfied using the biased measured data, under the assumption of small errors. Birch et al. (2013) showed that for relative errors  $\ll 100\%$  the resulting influence on the estimation is negligible.

Applying this estimation presents certain challenges, some parameters are not given as distinct values, but rather represented by probability distributions. To obtain representative values across the entire measurement set, in which the maximum tangential velocity  $V_{\theta, \max}$  and the vortex core radius  $r_c$  vary, a conservative approach was chosen. This was achieved by selecting the 95<sup>th</sup> percentile of  $V_{\theta, \max}$  and the 5<sup>th</sup> percentile of  $r_c$  for the tip vortex data. Nevertheless, this error estimate does not include all contributing factors, e.g., the actual particle size inside the vortex is unknown. The influence of the lack of seeding particles near the vortex core, is discussed in Chap. 4.1.2.

A precise determination of the particle diameters was not possible, as no measurements were taken during the experiment. However, reference measurements of particle distributions from comparable seeding devices are available in Raffel et al. (2018) and Kähler et al. (2002), and are shown in Fig. 3.13 for both seeding devices used in this study. Assuming a 95 % confidence

interval for the  $q_3$ -distributions in this context, yields particle sizes of  $5.05 \mu\text{m}$  for the CTS 1000 and  $2.10 \mu\text{m}$  for the Laskin seeding device. These values are noticeably higher than those commonly cited in the literature (see, e.g., Bauknecht (2016)). This discrepancy is primarily attributed to the fact that the  $q_3$  distribution is volume weighted, whereas in PIV measurements, an area-weighted distribution more accurately reflects the particle occurrence.

For a Laskin seeding generator the area-weighted cumulative distribution yields a particle diameter of  $1.31 \mu\text{m}$ . Unfortunately, equivalent area-weighted data for the CTS 1000 is not available. A simplified reconstruction of the  $q_2$  value for the Laskin device produced inconsistent results in the estimated distributions.

To provide at least an informed estimate, the ratio between  $q_2$  and  $q_3$  for the Laskin generator was used to approximate a  $q_2$  cumulative distribution for the CTS 1000. This approach resulted in an estimated particle size of  $d_{p,0.95} = 3.2 \mu\text{m}$ .

Furthermore, one could argue that centrifugal forces preferentially displace larger particles away from the vortex core, concentrating smaller particles in the region of maximum swirl velocity. This suggests that the actual error due to particle inertia may be significantly lower than previously estimated. Results from synthetic PIV data of vortices from Domogalla (2021) also indicate a smaller error than predicted for similar conditions. The resultant particle velocity lag uncertainties for all FOV's are shown in Tab. 3.5.

**Table 3.5.:** Particle velocity lag uncertainty

Field of view	$V_{\theta,\text{max},0.95}$	$r_{c,0.05}$	$d_{p,95}$	$\varepsilon_{\theta}$
Vertical FOV, large	$19.87 \text{ m s}^{-1\text{a}}$	4.20 mm	$3.2 \mu\text{m}$	12.85 %
Vertical FOV1, small	$27.01 \text{ m s}^{-1}$	2.76 mm	$1.31 \mu\text{m}$	1.54 %
Vertical FOV2, small	$21.71 \text{ m s}^{-1}$	3.70 mm	$1.31 \mu\text{m}$	0.56 %
Vertical FOV3, small	$17.43 \text{ m s}^{-1}$	4.27 mm	$1.31 \mu\text{m}$	0.27 %
Horizontal FOV	$2.28 \text{ m s}^{-1}$	1.12 mm	$3.2 \mu\text{m}$	2.38 %

<sup>a</sup> Due to large particle voids, this value does not represent the physical maximum and is utilized solely for the purpose of error estimation (see Chap. 4.1.2).

### 3.3.3. Sampling Uncertainty

Up to this point, only the errors associated with instantaneous PIV results have been discussed. Higher sampling, by, e.g., averaging several flow fields typically helps to reduce these errors. However, in this thesis mainly instantaneous results were evaluated, although at least for 50 rotor revolutions. The data from each instantaneous image was subsequently averaged according to its corresponding rotor azimuth angle or vortex age. The specific procedure differs

for the different measurements and is discussed in Chap. 4.

### 3.3.4. Image Processing Errors

The correct parameter settings of multi-pass PIV processing have a significant influence on the quality of the data. Keane et al. (1992) demonstrated in a Monte Carlo simulation using synthetic PIV data that the probability of correct velocity detection is mainly dependent on the image particle density  $N_i$ , the in-plane loss-of-correlation  $F_i$ , and the out-of-plane loss-of-correlation  $F_o$ , where  $F_i = 1$  and  $F_o = 1$  if no loss of correlation is present. To obtain at least 95 % valid detections peaks, the Monte Carlo simulation predicts a requirement of

$$N_i F_i F_o > 5. \quad (3.19)$$

In other words, at least five particles in a correlation window of the first image must also be present in the respective correlation window of the second one. For all PIV systems used, a seeding density of approximately 0.025 ppp was achieved. For the final interrogation windows, which have a size of 16 px  $\times$  16 px, this results in an average of 0.025 ppp  $\cdot$  16<sup>2</sup>px = 6.4 particles per final interrogation window.

Modern multi-pass interrogation algorithms implement a window-shifting approach, which aligns the second interrogation window with the expected particle displacement. This effectively eliminates in-plane decorrelation, resulting in  $F_i \approx 1$ . The physical limitation of out-of-plane losses cannot be eliminated. A light sheet thickness of approximately 5 mm for the low-speed laser and approximately 10 mm for the high-speed laser is assumed. For the horizontal setup, for instance, a maximum  $\Delta t$  of 50  $\mu$ s was used, which together with the maximum swirl velocity of 28 m s<sup>-1</sup>, leads to a minimum  $F_o$  of 0.86 and accordingly results in  $N_i F_i F_o = 5.50$ . Another well-known rule of thumb, additionally recommends keeping the out-of-plane displacement below one quarter of the light sheet thickness ( $\Delta z/z_{LS} < 0.25$ ). This condition is fulfilled for all measurements.

For the vertical PIV planes, the situation is more complex as  $\Delta t$  was adjusted based on

**Table 3.6.:** Loss-of-correlation effect

Field of view	Light sheet thickness $z_{LS}$	$\Delta t_{\max}$	$w_{LS, 95}$	$N_i F_i F_o$
Vertical FOV, large	5 mm	70 $\mu$ s	8.90 m s <sup>-1</sup>	5.60
Vertical FOV1, small	5 mm	25 $\mu$ s	3.60 m s <sup>-1</sup>	6.28
Vertical FOV2, small	5 mm	50 $\mu$ s	8.15 m s <sup>-1</sup>	5.88
Vertical FOV3, small	5 mm	70 $\mu$ s	5.06 m s <sup>-1</sup>	5.95
Horizontal FOV	10 mm	50 $\mu$ s	28 m s <sup>-1</sup>	5.50

the expected out-of-plane component, ranging from  $7 \mu\text{s}$  to  $70 \mu\text{s}$ . Additionally, the expected out-of-plane velocity is more difficult to predict, as axial velocity components in vortex models are not well documented. In general, young vortices tend to exhibit higher axial velocities and are also linked to the blade's immediate wake, which itself shows stronger out-of-plane motion.

For measurements with the large FOV this is less critical, as the analysis does not focus on accurate results near to the vortex core, where the axial velocity of a vortex should be the highest. In contrast, for the high-resolution PIV (smaller FOVs), a parameter study on  $\Delta t$  demonstrated convergence of swirl velocity distributions, indicating the validity of the chosen delay settings. Table 3.6 summarizes the loss-of-correlation effect for all FOVs.



## 4. Data Processing

Careful data processing is essential for generating meaningful results. Each measurement therefore requires a customized processing chain to account for necessary masking, to exclude defective image regions (e.g., blades or reflections), outlier filtering, and variations in vortex processing. When preparing the data for a comparison with CFD, it is necessary to harmonize post-processing procedures. The standard processing of PIV data differs from the typical CFD post-processing procedure, for example due to the high sensitivity of velocity gradient calculations to measurement noise. Since the measurements were intended to provide a comprehensive dataset for the comparison with numerical results, it is crucial to document the exact evaluation procedure. This is because even minor differences in the procedure can lead to substantially different outcomes. Parts of the Chapters 4.1.1 and 4.2 were published in Heintz et al. (2025) and Heintz et al. (2023). Descriptions of comparisons with high-resolution CFD data can be found in Gajo et al. (2024).

### 4.1. Vertical Field of Views

The purpose of the vertical FOVs is to capture the position and characteristics of primary blade tip vortices. Therefore, two distinct measurement campaigns were conducted.

The first campaign was carried out in parallel with the horizontal secondary vortex investigations to examine potential correlations between vortex decay and the formation of secondary vortices. It primarily focused on vortex positions and basic characteristics, such as their circulation, which serves as a key indicator of vortex breakdown, see, e.g., Ghimire et al. (2017). The second campaign focused on four representative cases, employing a significantly smaller FOV and finer seeding particles to enable high-resolution measurements of the vortex velocity field. This enabled accurate vortex velocity measurements down to the inner part of the vortex.

Together, these datasets establish a comprehensive validation and reference case for the analysis of vortex decay in hovering rotor conditions. A description of the overall PIV setup is provided in Chap. 3.2.3.

### 4.1.1. Overview Vertical PIV

Figure 4.1a shows a camera image of the overview PIV setup, which was mapped to the radial-axial reference frame ( $r/z$ ) of the rotor. Particle voids result in an intuitive visualization of the tip vortices, but also in a lack of quantitative velocity data. Consequently, evaluations of the maximum swirl velocity  $V_{\theta, \max}$  or the vortex core radius  $r_c$  are not performed for the overview PIV data.

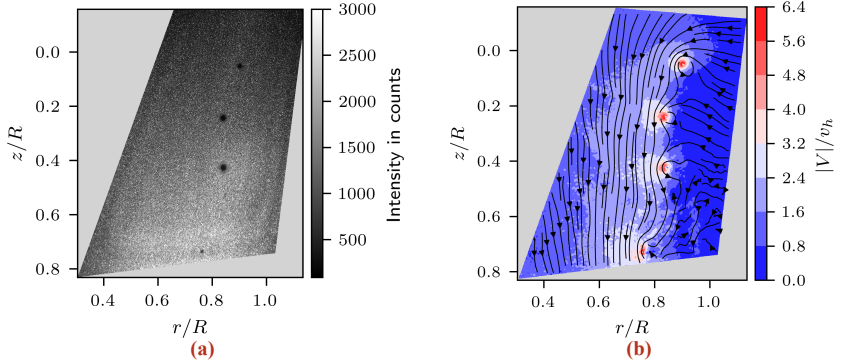


**Figure 4.1.:** Vertical PIV plane at 0.05  $z/R$  rotor height: a) Raw image from a PIV camera in world coordinates, b) Sample vertical PIV result.

In Fig. 4.1b the resultant velocity field is depicted. The four particle voids in the vortex centers are not visible, since the missing correlation data was filled up with interpolated values to facilitate subsequent evaluation steps. As a first step, a median filter with a window size of 5 points, equivalent to 4.13 mm, was applied to remove outliers and slightly smooth the vector field. The filtered data was used solely for vortex detection, while the raw data served for quantitative analyses. Following this, some areas of the measurement plane may contain erroneous data due to the rotor blades blocking the camera view. These areas were masked automatically based on the PIV processing results: On the one hand, high uncertainties in the  $x, z$ -plane derived by the correlation statistics, described e.g., by Wieneke (2015), and on the other hand low correlation values. The mask is then slightly dilated to ensure that the entire blade is masked. Before calculating the vortex criteria for the vortex detection, it is necessary to calculate the velocity gradients. Only spatial gradients were considered since the temporal resolution of 10 Hz is too low to calculate meaningful temporal gradients. For the first estimate of the vortex location the swirling strength

$$\lambda_{ci} = \max \left[ \Im \left\{ \frac{1}{2} \left( \frac{\partial u}{\partial x} \frac{\partial v}{\partial y} \right) + \sqrt{Q} \right\}, \Im \left\{ \frac{1}{2} \left( \frac{\partial u}{\partial x} \frac{\partial v}{\partial y} \right) - \sqrt{Q} \right\} \right] \quad (4.1)$$

was used.

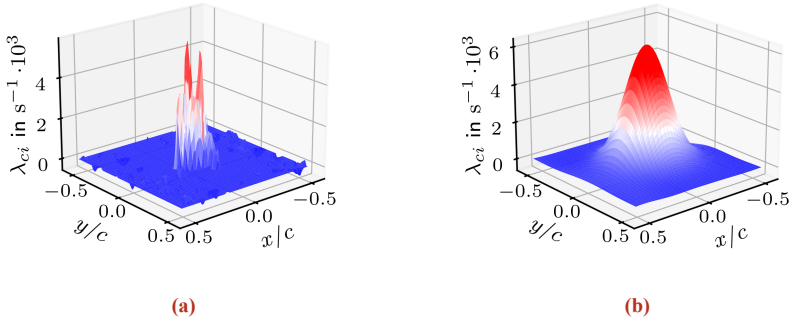


**Figure 4.2.:** Primary blade tip vortex detection and post-processing: a) Unfiltered vortex, b) Low-Pass filtered vortex

A sample distribution of the swirling strength for a middle-aged vortex and without further post-processing is shown in Fig. 4.2a. Due to limited resolution in the vortex core, the vortex criterion does not provide reliable data in this sector. For instance, in Fig. 4.2a, this results in multiple peaks appearing for a single vortex. In addition, the gradient operator amplifies noise in the vortex criterion data. To prevent false detections, a Gaussian kernel ( $\sigma_{\text{Gaussian}} = 10$  points, respectively  $\sigma_{\text{Gaussian}} = 8.2$  mm) was applied to the raw swirling strength field via convolution, with a magnitude preserved by multiplication with  $\sigma$ . A similar approach was used by van der Wall et al. (2006) or Bauknecht et al. (2015). The filtered result is shown in Fig. 4.2b.

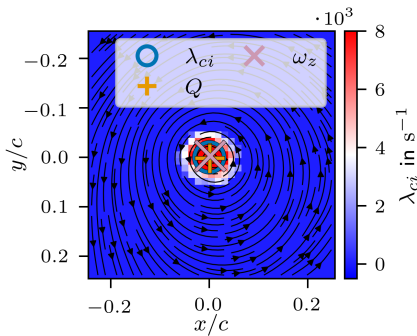


**Figure 4.3.:** Vortex center detection based on different vortex criteria

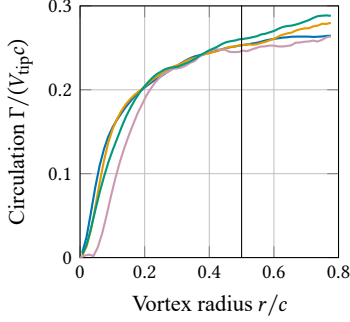


**Figure 4.4.:** Circulation  $\Gamma$  over the vortex radius normalized with the blade chord length  $c$  for several sample vortices

The peak of the filtered data is not necessarily equivalent to the physical vortex center. Hence, a cut-off threshold of  $\lambda_{ci} = 2800 \text{ s}^{-1}$  is applied, and subsequently, the resultant area is utilized to determine the center of gravity concerning the values of  $\lambda_{ci}$ . In instances where the blade loading varies, the threshold is scaled accordingly. A comparison of the selected  $\lambda_{ci}$ -criterion with two other commonly used criteria, the  $Q$ - and  $\omega_z$ -criterion, showed only minor discrepancies, see Fig. 4.3 for an example.

In addition to identifying vortex positions, it is crucial to extract essential vortex properties, particularly vortex circulation  $\Gamma_v$  and swirl velocity  $V_\theta$ . To achieve this, a radial binning method is employed, where the average tangential velocity within each radial bin is computed, see Fig. 4.5. This approach provides the swirl velocity,  $V_\theta$ , as a function of the vortex radius,  $r$ . Similar approaches were already used by Wolf et al. (2019a) or Braukmann (2021).

With the swirl velocity profile, the vortex circulation  $\Gamma_v$  was determined at a specific radius using the line integral of the velocity around a closed curve, as given by the following equation:

$$\Gamma = \oint_{\mathcal{C}} \mathbf{V} \, ds \xrightarrow{\text{for circles}} \Gamma(r) = 2\pi r_{\text{mean}} V_\theta(r_{\text{mean}}) \quad (4.2)$$

However, due to the large particle void in the vortex core, it was not possible to detect the maximum swirl velocity for most of the vortices. As a result, this study focuses on examining the circulation. Given the insufficient velocity data in the central void, the circulation is calculated via the shown line integral (Eq. 4.2) of the tangential velocity at a specific radius rather than via the surface integral of the vorticity.

In Fig. 4.4 the resulting circulation  $\Gamma_v$  as a function of the vortex radius  $r$  is shown. To capture the majority of the total circulation while minimizing the influence of neighboring

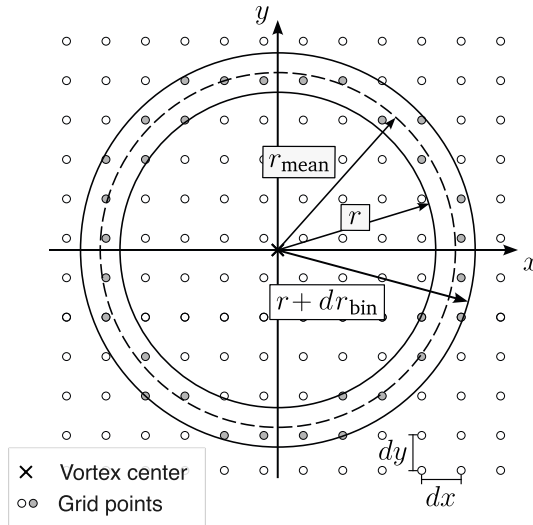


**Figure 4.5.:** Sketch of binning a vortex in radial slices, after Braukmann (2021)

flow structures, a radius of  $r/c = 0.5$  provides a suitable compromise. This radius lies outside the vortex core, where the circulation increases sharply with radius, but not that far as to be overly influenced by external factors.

A database is used to store the information of each identified tip vortex, including its position, the associated rotor azimuth and PIV image data, the total circulation, and the radial distribution of velocity and circulation. It contains information from 500 instantaneous flow fields acquired at 10 different traverse heights. Each flow field contains multiple tip vortices which must be assigned to the respective vortex age and blade number (in case of multi-blade rotors). This process is quite complex, since the tip vortices were sometimes masked by the blades, and the youngest vortices close to the rotor plane were not within the PIV field of view, particularly for higher traverse positions.

Initially, the measurement point with the lowest rotor position, or the youngest tip vortices, was evaluated. Utilizing the current azimuth of the rotor, the initial vortices within the FOV were assigned to their corresponding blade of origin. Based on the order in which the vortices were arranged downstream, all other vortices of the respective instantaneous flow fields were also assigned to their vortex age. Since some vortices were still incorrectly assigned because some were obscured by blades, it was necessary to correct the aforementioned assignment. The correction assumes that younger vortices from the same blade occur at higher positions than older ones and that age assignments can only be too young, never too old. For instance, if the

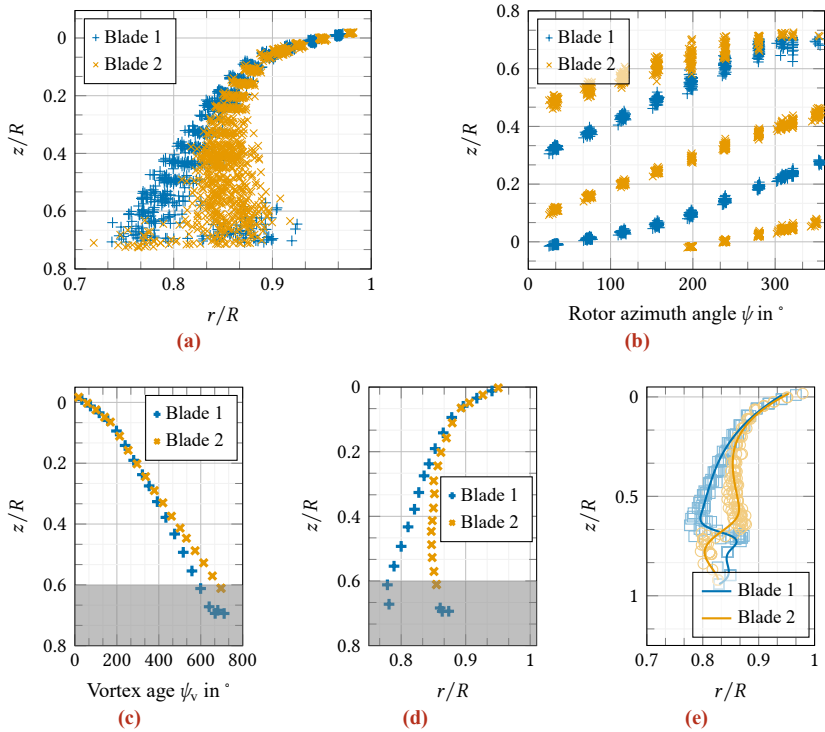


**Figure 4.6.:** Blade tip vortex processing steps: a) Detected vortices from a single measurement (500 images), b) Vortices sorted by rotor azimuth angle, c) Averaged vortex  $z$ -position of the first measurement in the two-blade case plotted over vortex age, d) Averaged vortex position of the first measurement in the two-blade case, e) Merged blade tip vortex positions.

first vortex is obscured by a blade, the second vortex may have been assigned an age that is too young and does not match its height. These assumptions allow the vortex ages to be corrected until the assigned age matches the vortex position. The vortex age is then used to determine the blade of origin. Figure 4.6a shows the result of this separation for a representative case of a two-bladed rotor.

The measurement was conducted at only ten different azimuthal rotor positions, which permitted the vortices in each instantaneous flow field to be sorted by their current rotor azimuth angle, shown in Fig. 4.6b. This illustration demonstrates that the points accumulate in point clouds in accordance with their vortex age. For each of these point clouds, the median was calculated to remove outliers, yielding a single data point for each vortex age. As a result, Figs. 4.6c and 4.6d show the median  $z$ -positions of the tip vortices as a function of the vortex age and median radial positions, respectively. Due to an accumulation of mismatches in the lowest part of the FOVs, they are only evaluated up to 450 mm ( $z/R = 0.59$ ) below the rotor plane. The areas of unreliable data in Figs. 4.6c and 4.6d is grayed out.

Up to this point, only measurements from the lowest rotor traverse position were evaluated. At higher positions, the youngest vortices are no longer within the FOV. To determine the vortex age in such cases, the high vertical overlap of the FOVs was exploited. Results from the top FOV were used to interpolate the vortex age as a function of the height  $z/R$ . The youngest vortices in the lower FOV were subsequently assigned to a specific blade and vortex age based on their height and the blade position at the time of acquisition. A fifth-order smoothing spline was then fitted to the calculated points to construct the vortex trajectory, as shown in Fig. 4.6e. It is noted that in Fig. 4.6 the trajectories of blades 1 and 2 are dissimilar due to a *vortex pairing* event, details on this phenomenon will be discussed in Chap. 6.

### 4.1.2. High-Resolution Vertical PIV

To overcome limitations associated with the large FOV, a supplementary high-resolution study was conducted for selected cases. Three separate FOVs were measured to capture the full range of vortex ages. The FOV positions were staggered in axial direction and shifted in radial direction to follow the contracting vortex trajectories.

This specialized setup, however, required additional methodological considerations to ensure the validity and consistency of the measurements. The adapted post-processing approach is described in the following.

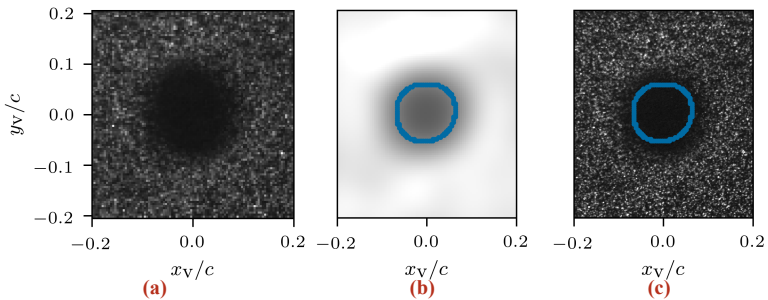


**Figure 4.7.:** Void detection procedure: a) Interpolated reduced data (every fourth pixel), b) Low-passed filtered reduced data with identified void boundary, c) Original data with detected void boundary

### Vortex Void Detection

Before calculating vortex properties, it is important to consider the absence of seeding particles inside the vortex core in PIV measurements. Interrogation windows containing such particle voids may lack valid velocity information and should therefore be excluded from statistical analysis. To detect these voids, each recorded image was first dewarped and then downsampled by a factor of four in both spatial dimensions to reduce the overall dataset size. These reduced images, exemplary shown in Fig. 4.7a, were subsequently used in the void detection process.

Prior to void detection, the reduced images were linearly interpolated onto the coordinate grid used for the flow field measurements. Given the PIV processing parameters (16 px interrogation windows with 75% overlap, resulting in a vector spacing of approximately 4 px), this interpolation results in only minor corrections due to the near equivalence of the grids. Subsequently, the blade masking used in the flow field processing is directly applied to the

interpolated images. This enables an intensity correction to account for gradients present within the original image data.

For void detection, all images were low-pass filtered using a convolution filter with Gaussian weighting, as illustrated in Fig. 4.7b, removing the individual tracer particles and focusing on the large-scale intensity variation caused by the void. To detect the void, a thresholding approach was applied, masking all regions below a defined intensity level. Figure 4.7c shows the detected void in the raw image and demonstrates that the applied processing yields comparable results to the direct analysis of the original (non-downsampled) images.

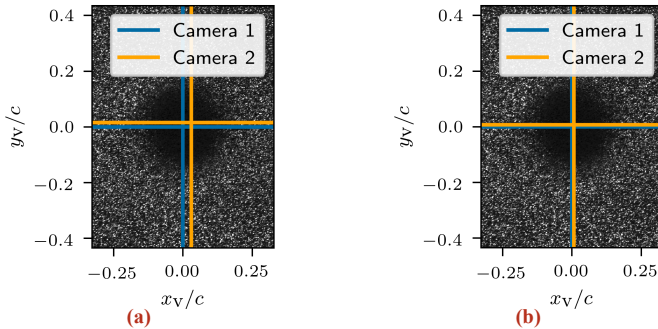


**Figure 4.8.:** Void center detection of two cameras: a) After reconstruction using the calibration and self-calibration, b) Calibration was manually shifted into the light sheet by 0.5 mm

When comparing the detected void positions from both stereo cameras, a slight deviation between the voids became apparent, as shown in Fig. 4.8a. Analysis of the deviation map obtained during self-calibration reveals that, for some images, the observed shift significantly exceeded the expected calibration error. However, considering the light-sheet thickness of approximately 5 mm, this deviation appears reasonable. Introducing an artificial out-of-plane offset of 0.5 mm into the calibration, as demonstrated in Fig. 4.8, nearly compensates for the observed displacement. This suggests that the discrepancies between the void positions are likely related to the finite thickness of the light sheet.

Nevertheless, the processing of Stereo-PIV data was affected by this phenomenon, as each image was initially evaluated independently. For vortex void masking, the binary masks from all four images (two cameras with two frames each) were summed. Although the void position does not change within the short  $\Delta t$  between frames, including both frames increases reliability. The resulting region was then represented by an ellipse fitted to its boundaries. In the final vortex velocity profiles, the major axis of this ellipse was interpreted as the void *radius*.

In the subsequent analysis, all related vortices were clustered using a machine learning

approach based on their vortex position and rotor azimuth. To determine velocity profiles and vortex properties of each cluster, all individual vortices were interpolated onto a common set of radial coordinates.

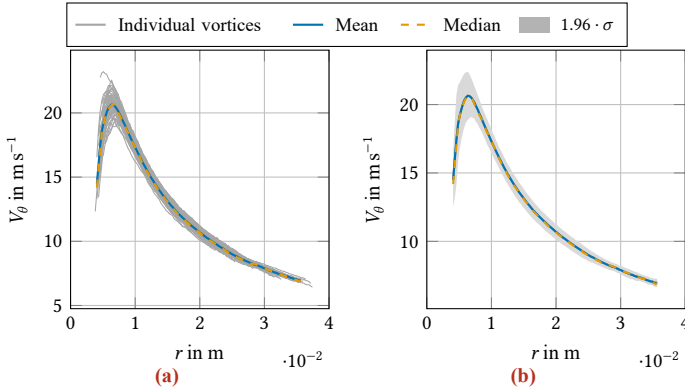


**Figure 4.9.:** Evaluation of the velocities of one series of vortices at a common vortex age

For each coordinate with at least five valid data points, defined as points outside the vortex void and not intersecting the FOV boundary, the mean, median and standard deviation of the velocity were calculated, see Fig. 4.9a. This procedure ensured that invalid data did not influence the results, in contrast to methods in which void regions are included after averaging.

Comparisons with simple binning methods, as used for the overview FOV, showed that, particularly in regions with strong velocity gradients, the interpolation approach yields superior accuracy. Unlike spline curve fitting approaches the applied method also enables basic statistical analysis. The resulting vortex velocity and circulation profiles and their associated deviations are shown in Fig. 4.9b.

This data is subsequently taken to also calculate vortex circulation distribution, vortex core radius and the maximum swirl velocity. An example of this evaluation is plotted in Fig. 4.10.

## PIV Parameter Study

Due to the higher demand for precise velocity data, an extensive parameter study was carried out on the high-resolution PIV datasets, and the resulting flow velocities were systematically compared. Richard et al. (2006) showed that vortex velocity, especially maximum swirl velocity, and vortex core radius are sensitive to PIV evaluation parameters. In particular the

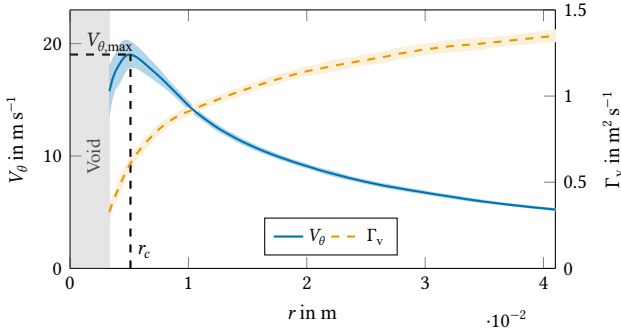


**Figure 4.10:** Example vortex properties

interrogation window overlap and the final window size exert a pronounced influence on vortex parameters.

As a rule of thumb, PIV measurements tend to underestimate swirl velocity and overestimate the vortex core radius. Therefore, a systematic parameter study was conducted, varying the aforementioned parameters as well as the final interrogation window shape for each measurement point. As for the final evaluation, the vortices were averaged across all images corresponding to the same rotor azimuth position, resulting in a single vortex velocity distribution including statistical properties.

The maximum swirl velocity and the vortex core radius were then extracted, along with their respective  $1.96 \cdot \sigma$  values, corresponding to the 95% confidence interval under the assumption of normally distributed data. Compared to previous parameter studies (e.g., by van der Wall et al. (2006)), this approach further enhances the statistical significance of the resulting data. To reduce the influence of particle voids, a measurement location with minimal void regions was selected. (In this case 95% for the vortex voids are below 2.12 mm).

The resulting study is depicted in Fig. 4.11, illustrating the major PIV correlation parameters, available in DaVis 11.4.6. A detailed description of the evaluation parameters is provided in Chap. A.

Initially, the influence of multigrid settings was evaluated. It is imperative to select sufficiently large initial windows to capture the maximum particle shift within the double frame, ensuring a distinct correlation peak. At the same time, excessively large initial windows should be avoided as they necessitate numerous multigrid passes and thereby increase computational effort. Figure 4.11a demonstrates that the influence of the initial window size on the vortex properties is rather low, when keeping it above 64 px.

The final interrogation window determines the spatial resolution of the derived velocity

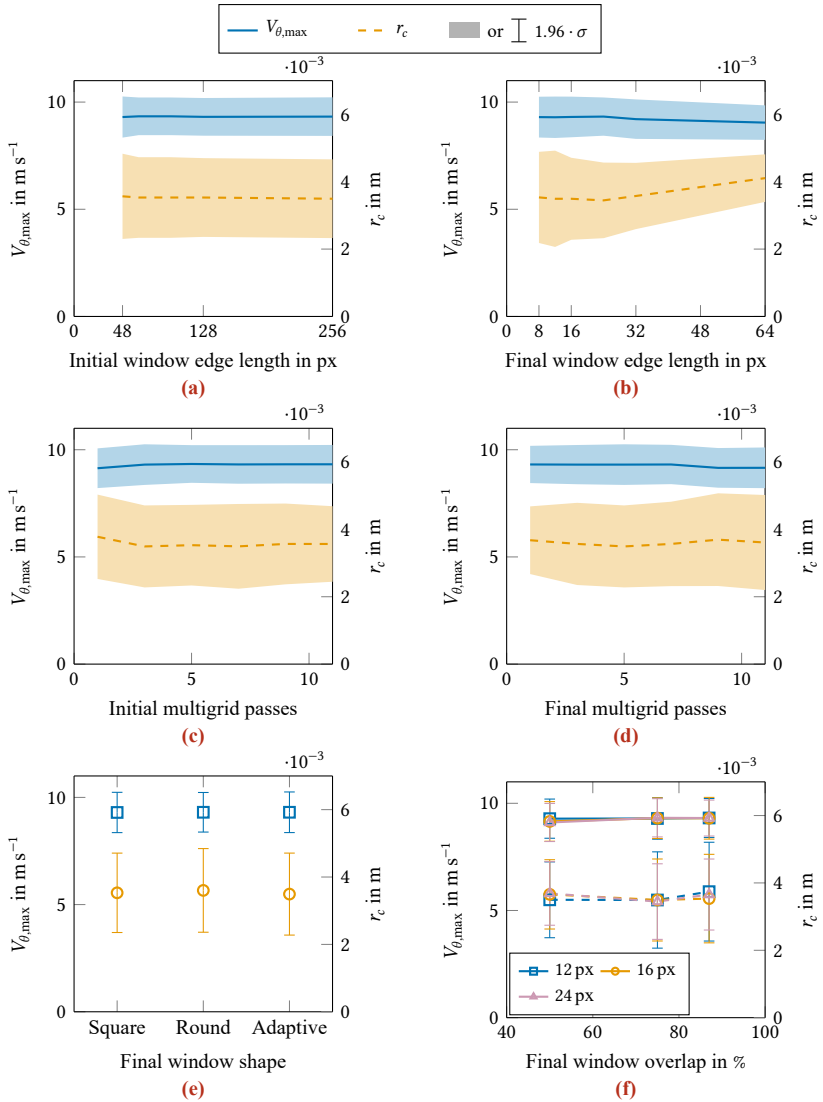


Figure 4.11.: PIV correlation parameter study in DaVis 11.

field and is therefore a critical parameter influencing both precision and data size. In this study, the vortex identification algorithm was adjusted for various resolutions. In accordance with van der Wall et al. (2006), increasing the final window size generally leads to lower peak swirl velocities and larger vortex core radii. This trend is confirmed in Fig. 4.11b. However, evaluations remain robust for window sizes up to approximately 24 px, consistent with findings by Bauknecht (2016).

With respect to the vortex core radius, it remains nearly constant up to 24 px, after which a slight increase in core size was observed. The standard deviation of the extracted parameters decreases with increasing final window size. While this reduction might indicate increased precision, the deviation becomes notably high for window sizes smaller than 16 px, indicating unreliable results in that regime. It should also be noted that the requirement of  $N_i F_i F_o > 5$  as discussed in Chap. 3.3.4, is not fulfilled for windows below 16 px.

In a multigrid PIV processing not only the window sizes, but also the number of passes between window refinements are decisive settings for obtaining reliable results. Although the exact internal algorithms of DaVis are not fully disclosed, we evaluated the influence of the pass settings to ensure that this parameter does not affect the outcome significantly. Reducing the number of passes without compromising accuracy also minimizes computational effort. As shown in Figs. 4.11c and 4.11d, the impact of this setting is indeed negligible. Nevertheless, a minimum of three initial and three final passes is recommended to ensure convergence.

Modern PIV correlation software allows customization of the final interrogation window shape. In DaVis 11, square, circular, elliptical, and adaptive windows are available. Square windows are computationally efficient and therefore well suited for initial passes. Circular or adaptive windows use an initial interrogation window with twice the edge length, applying weighted contributions corresponding to the nominal window size. Circular windows apply a Gaussian weighting function, while adaptive windows further vary the shape in the first pass based on the local velocity gradient field. Elliptical windows are primarily intended for flows with high gradients in a certain direction, see LaVision (2023). In boundary layer flows, for instance, spatial resolution of the velocity gradient can be increased when the major axis is perpendicular to the wall, where the gradients are lower and not require a high spatial resolution. In vortex flows, however, this gradient occurs in radial direction. Hence, the use of adaptive windows, following the gradient in Cartesian coordinates should be beneficial.

The influence of the final interrogation window shape on the major vortex parameters is depicted in Fig. 4.11e. Although the overall influence is minor, square and adaptive windows tend to produce slightly higher maximum swirl velocities and smaller vortex core radii. Considering the complexity of the rotor flow, a more pronounced impact might have been anticipated.

Figure 4.11f illustrates the effect of final window overlap for several interrogation window sizes. Consistent with findings of Bauknecht (2016), the window overlap has only a minor influence on maximum swirl velocity, regardless of window size. For overlaps above 75%, the maximum swirl velocity remains unchanged. The standard deviation remains unaffected, while the vortex core radius shows only a slight dependence on overlap. Given the absence

**Table 4.1.:** Selected PIV correlation parameters

Initial window size in px	Final window size in px	Overlap in %	Final window shape	Initial passes	Final passes
64	16	75	adaptive	3	5

of a known ground truth and the small variations observed, the evaluation can be regarded as robust with respect to this parameter.

To summarize this discussion, choosing reasonable PIV processing parameters most properly deliver very similar results. The selected evaluation parameters are shown in Tab. 4.1.

## 4.2. Horizontal Field of View

The detection of secondary vortices in the horizontal FOV was generally based on the same principles as the tip vortex detection in the vertical FOVs. To remove outliers and low-pass filter the vector field, first a convolution median filter with a window size of 9 points, respectively 5.22 mm was applied. Due to the camera positions, the masking of the blades, which are now very present in some pictures, was crucial for the horizontal FOV. In addition to the uncertainty and correlation values, the raw images are processed to eliminate over-illuminated parts of the blades that may not necessarily have a poor correlation value.

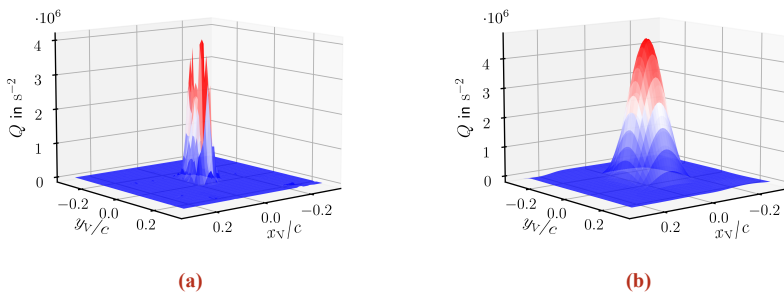


**Figure 4.12.:** Effects of filtering on the secondary vortex detection: a) Unfiltered vortex, b) Low-Pass filtered vortex

The vortex detection was once again based on a vortex criterion, namely the  $Q$ -criterion,

defined as

$$Q = \frac{\partial u}{\partial x} \frac{\partial v}{\partial y} - \frac{\partial u}{\partial y} \frac{\partial v}{\partial x} - \frac{1}{2} \left( \frac{\partial u}{\partial x} + \frac{\partial v}{\partial y} \right)^2, \quad (4.3)$$

which was also used by Schwarz et al. (2022) for detecting secondary vortices. It has been demonstrated to yield a slightly lower signal-to-noise ratio for secondary vortex detection compared with other criteria. However, when similar vortex criteria were taken, for example swirling strength, the results did not change significantly. The flow conditions differed from those of the vertical FOVs, as they involve both positive and negative vortex circulations. To differentiate between them, the  $Q$ -criterion is signed according to the sign of the vorticity and is defined as  $Q_{\text{rot}} = \frac{\omega_z}{|\omega_z|} Q$  in the following.

Even though, secondary vortices exhibited a weaker particle void, Fig. 4.12a indicates that the  $Q$ -criterion remains quite noisy for some cases. For this reason, a Gaussian convolution filter was also used for the horizontal FOV, but with a lower standard deviation of  $\sigma_{\text{Gaussian}} = 6$  pnts (or as a dimensionally affected value  $\sigma_{\text{Gaussian}} = 3.42$  mm), to account for the potential spatial proximity of the structures. A sample result of this procedure is shown in Fig. 4.12b. Secondary vortices were identified as coherent regions exceeding a threshold of  $Q_{\text{thr}} = 48 \cdot 10^4 \text{ s}^{-2}$ .

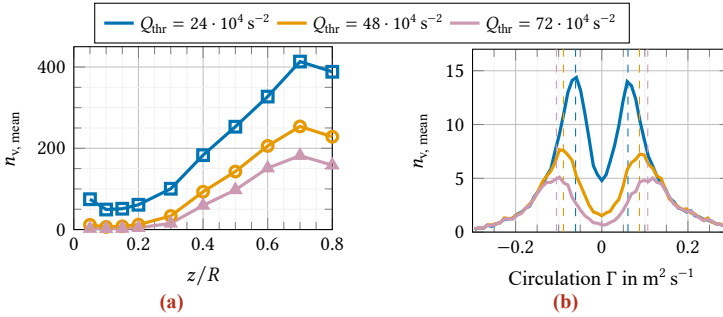


**Figure 4.13.:** Influence of the selected threshold  $Q_{\text{thr}}$ : a) Sample distributions of  $n_{v, \text{mean}}$  over the rotor height, b) Histogram of the circulation of the detected vortices

In Fig. 4.13 the influence of the  $Q$ -threshold choice on the number and circulation of the identified vortices for a two-blade sample case is shown. Figure 4.13a shows the significant influence on the number of detected vortices over  $z/R$ . A lower threshold leads to more secondary structures, but there is also a risk of detecting noise or small-scale turbulence. For  $Q_{\text{thr}} = 24 \cdot 10^4 \text{ s}^{-2}$ , for example, the blade shear layer was also detected at lower rotor positions. Nevertheless, different  $Q$ -thresholds yield qualitatively similar distributions. In order to get more insight into the vortex properties Fig. 4.13b shows a histogram of the circulation of

the detected vortices. For stronger vortices the circulation has no influence on the vortex number. For weaker vortices, a smaller  $Q$ -threshold results in a larger number of identified secondary vortices, and a higher probability of weaker secondary vortices. A threshold of  $Q_{\text{thr}} = 48 \cdot 10^4 \text{ s}^{-2}$  was found to be a good compromise between a high sensitivity but still excluding measurement noise and shear layer vortices.

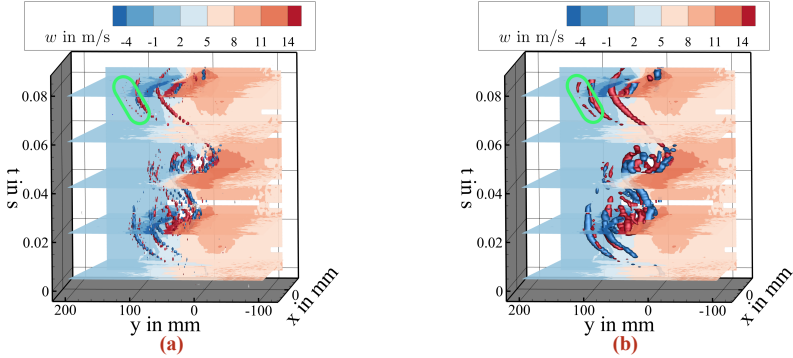


**Figure 4.14.:** Secondary vortex detection sample for a one-blade test-case over the time at  $z/R = 0.4$  with iso-surfaces of  $Q_{\text{thr}} = 48 \cdot 10^4 \text{ s}^{-2}$ : a) Raw data, b) Low-Pass filtered data

To visualize the effect of filtering on secondary vortex detection, the results of a filtered and unfiltered detection are plotted over time in Fig. 4.14. The time axis is scaled by the blade tip vortex convection velocity to obtain a three-dimensional flow field under the assumption of spatially constant convection velocity and the Taylor hypothesis (Taylor (1938)). There is a good agreement between the detected structures with and without the Gaussian convolution filter. However, the filtering yields a more continuous representation of the secondary structures, with fewer interruptions over time. This is, for example, apparent for the structure marked with a green box in the upper part of the figure.

For further evaluation of vortex properties, the determination of the center of a secondary vortex is crucial. It has to be taken into account that the peak of the filtered  $Q_{\text{rot}}$  field does not necessarily coincide with the center of a vortex. Therefore, it was identified as the center of gravity of the unfiltered vorticity values in this region. Figure 4.15a shows in analogy to Fig. 4.3 that the identification of the secondary vortex centers is insensitive to the choice of the vortex criterion.

For a detailed analysis of the behavior of secondary vortices, it is crucial to gain insight into their properties. Similar to blade tip vortices, vortex circulation is a key parameter for determining the strength of these vortices. The calculation is also robust against disturbances and inaccuracies of the velocity field near the vortex centers using the binning method already

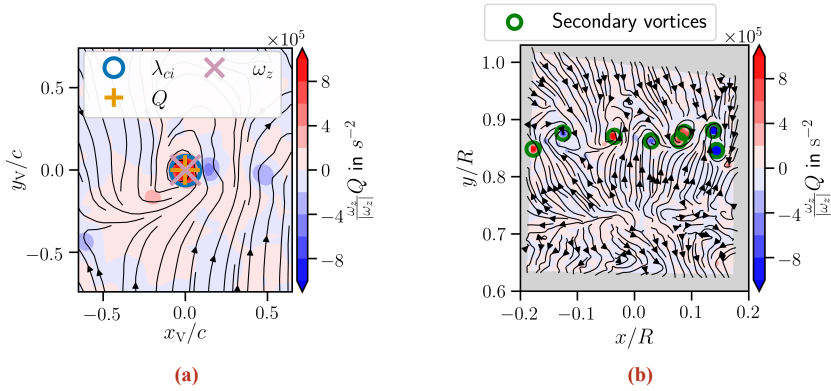


**Figure 4.15:** Secondary vortex detection sample for a two-blade test-case at  $z/R = 0.4$ : a) Vortex center detection using different vortex criteria, b)  $Q$ -criterion of the flow field, with detected secondary structures

presented for primary blade tip vortices, see Fig. 4.5. However, the primary challenge in evaluating secondary vortices is not the vortex void. Secondary vortices exhibit much lower circulation, resulting in a less pronounced void. Instead, the main difficulty arises from the close spatial proximity of individual vortex structures. To counter this, it is necessary to choose a radius that is both outside the vortex core and as small as possible to minimize the influence of adjacent vortices. The determination of such a radius is explained below.

To determine a suitable radius for circulation evaluation of secondary vortices, both the lower and upper limits must be considered. The lower limit is set by the vortex core size, up to which circulation increases rapidly with radius. Figure 4.18 shows sample circulation profiles as a function of the vortex radius  $r$ . It can be seen that the edge of the core is approximately between  $0.08 < r_v/c < 0.14$ , which therefore defines the minimal evaluation radius. The upper limit is constrained by the spatial proximity of neighboring secondary vortices. Figure 4.16 presents a histogram of nearest-neighbor distances for all secondary vortices of the reference two-blade case. Accordingly, an evaluation radius of  $0.15c$  would cause an interference of about 34 % off all secondary vortices, whereas a radius of  $0.1c$  reduces the interference to 10 %, but fails to capture the full circulation. A radius of  $0.15c$  was therefore selected. Assuming only one intersecting vortex, the intersection fraction of the integration path can be expressed as a function of the distance to the nearest-neighbor  $d$

$$\text{Intersected ratio}(d) = \frac{\arccos\left(\frac{d}{2 \cdot 0.15}\right)}{180^\circ} \quad (4.4)$$

Applying this formulation together with the histogram data (Fig. 4.18) yields an average

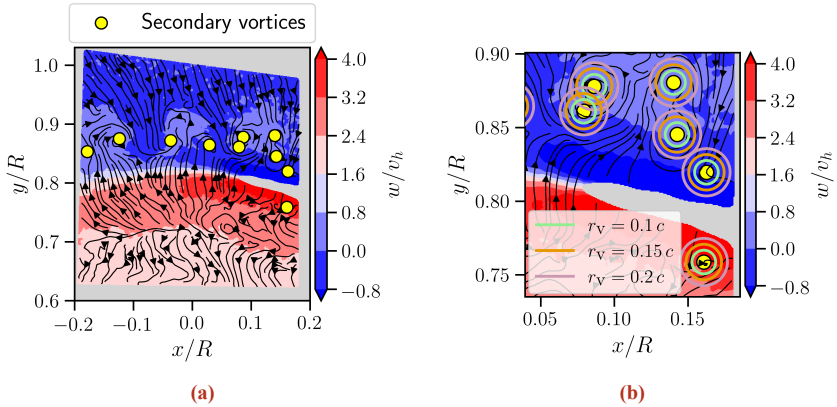


**Figure 4.16.:** A sample  $w$ -velocity flow field and masked vortex void: a) Overall flow field with secondary vortices, b) Detailed view on the vortex void. Secondary vortices and evaluation radii for the circulation calculation are shown.

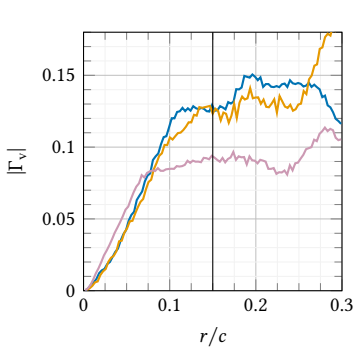


**Figure 4.17.:** Sample circulation distributions of secondary vortices, where the black vertical line denotes the radius used for the line integral.

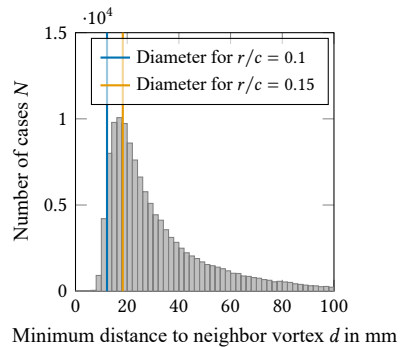


**Figure 4.18.:** Histogram of the distance to the nearest vortex for a sample two-blade case (all traverse heights).

intersection ratio of about 6.5 %, which represents an acceptable compromise between capturing circulation and avoiding excessive interference.

## Secondary Vortex Statistics

Secondary vortices are part of a turbulent decay in the rotor wake and their occurrence is subject to inherent randomness. As a consequence, their evaluation has to be based on a statistical analysis, requiring a sufficiently large sample size. For this reason, 2500 flow fields were measured at each height ( $z/R = 0.05, 0.1, 0.15, 0.2, 0.3, 0.4, 0.5, 0.6, 0.7, 0.8$ ) providing statistics for more than 150 rotor revolutions. These data are subsequently used to quantify secondary structures as a function of the wake age, respectively distance from the rotor.

To ensure equal distribution across the azimuthal angles, each measured flow field is divided into one-degree azimuth bins. Each bin must contain data up to a radius of  $0.98 R$  to be included in the analysis. An example of this binning is shown in Fig. 4.19a, where the gray shaded region represents areas excluded by this criterion. In some images, blade reflections or other visual obstructions cause masking of certain areas, leading to regions without reliable data. To account for this, two rules were applied. Firstly, azimuth bins with more than 50 % masking were excluded from the analysis, as indicated by the dark gray windows in Fig. 4.19b. Secondly, for azimuth bins with less than 50 % masking, a correction factor was applied, accounting for the proportion of masked points (represented as NaN values) relative to the total number of points in the bin. This correction factor is defined as:

$$\text{correction} = \frac{\text{number of nan values}}{\text{number of values}}, \psi_i < \psi < (\psi_i + 1) \text{ and } 0.7 < R < 0.98. \quad (4.5)$$

For each azimuthal bin with available data, the average number of secondary structures  $n_{\text{sec},i}$  was computed and normalized to  $360^\circ$  azimuth

$$n_{\text{sec},i} = \frac{1}{N_{\text{windows}}} \sum_{j=1}^{N_{\text{windows}}} n_{\text{sec},j} \cdot (1 - \text{correction})^{-1} \cdot 360^\circ, \quad (4.6)$$

where  $N_{\text{windows}}$  represents the total number of measured windows in the azimuthal range and  $n_{\text{sec},j}$  is the number of secondary structures detected in the  $j$ -th window. Due to blade blockage, certain azimuthal regions lacked data. Assuming that secondary vortices appear in that regions with the same probability, the overall average of secondary vortices in all azimuthal regions with data (RWD) was finally calculated as the average of all available  $n_{\text{sec},i}$  values:

$$n_{\text{v,mean}} = \sum_{i=1}^{\text{RWD}} \frac{1}{\text{RWD}} n_{\text{sec},i} \quad (4.7)$$

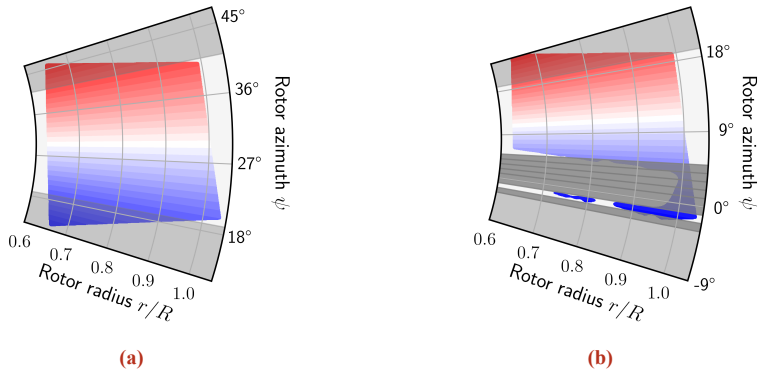


**Figure 4.19.:** Sample FOV for statistical secondary vortex evaluation with azimuthal bins used: a) Regular FOV with unused areas due to spatial limitations marked light gray, b) FOV with a blade mask inside; unused bins with more than 50 % mask coverage are additionally marked in dark gray.

This approach ensures a systematic analysis of secondary flow structures, accounting for potential data limitations such as masking and blade blockage. It also enables for a comparison of the experimental data, which is mainly limited in the azimuthal coverage and spatial resolved numerical data. A similar evaluation approach has been documented by Schwarz et al. (2022) or Bodling et al. (2023) and its results are elementary part of the discussion on factors influencing secondary vortices.

# 5. Blade Tip Vortex Measurements

This chapter presents a detailed investigation of the vortex parameters derived from high-resolution measurements of primary blade tip vortices. The results were evaluated against existing and slightly modified vortex models to benchmark how accurately these models capture the observed vortex behavior and to identify aspects that remain insufficiently described. The experimental results were previously analyzed in the bachelor thesis of Neef (2025), which was supervised by the author.

Comprehensive, high-quality comparisons for vortices with ages exceeding  $900^\circ$  are scarce in the literature. This study therefore contributes closing that gap by complementing existing datasets and model validations. The measurement setup and data processing procedures are described in Chaps. 3.2.3 and 4.1.2.

Table 5.1 summarizes the investigated configurations and gives a short overview of the key rotor parameters.

**Table 5.1.:** Investigated configurations

Case	$N_b$	Blade	Blade loading $C_T/\sigma$	Thrust coefficient $C_T$	$V_{tip}$
0	1	DLR-HEL-0	$0.812 \cdot 10^{-1}$	$2.076 \cdot 10^{-3}$	$90.06 \text{ m s}^{-1}$
1	1	SpinBlades	$0.821 \cdot 10^{-1}$	$2.097 \cdot 10^{-3}$	$90.05 \text{ m s}^{-1}$
2	2	SpinBlades	$0.823 \cdot 10^{-1}$	$4.204 \cdot 10^{-3}$	$90.05 \text{ m s}^{-1}$
3	1	DLR-HEL-18	$0.814 \cdot 10^{-1}$	$2.080 \cdot 10^{-3}$	$90.06 \text{ m s}^{-1}$

## 5.1. Application of Vortex Models on Measurement Data

To evaluate how well the vortex models match the investigated configurations, the vortices were reduced to the maximum swirl velocity  $V_{\theta,max}$  and the vortex core radius  $r_c$ . The vortex circulation  $\Gamma_v$  was not included as a comparison parameter, primarily for two reasons:

First, owing to vortex aging effects, the assumption of approximately constant circulation is

only valid for very young vortices.

Second, even the prediction of the initial circulation using analytical or empirical methods is difficult and subject to significant uncertainty. The main contributing factors are the bound circulation, which cannot be easily determined analytically in the case of non-ideal lift distributions, and the unknown fraction of circulation that is ultimately rolled up into the blade tip vortex.

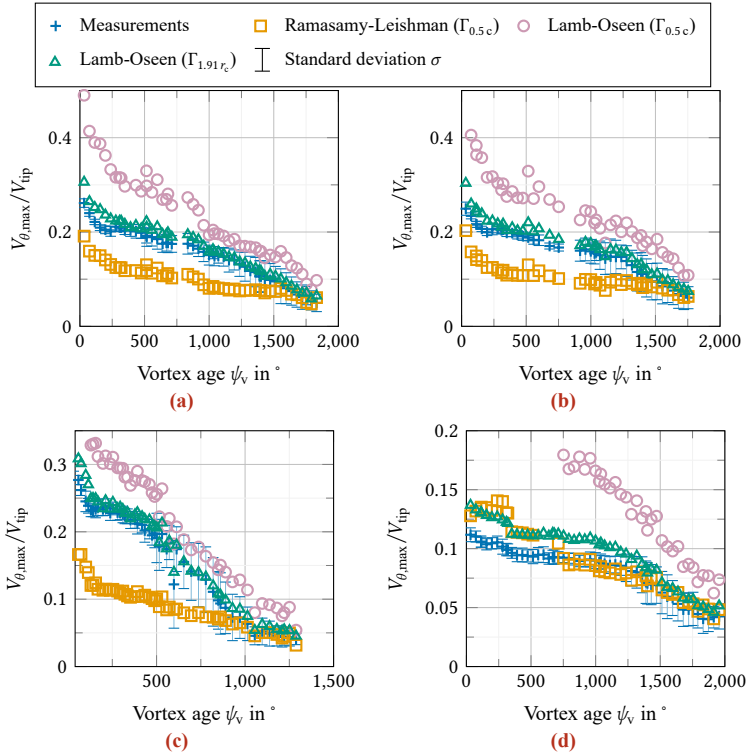


**Figure 5.1.:** Maximum swirl velocity as a function of vortex age, compared against individual Lamb-Oseen models for two reference circulation values and the Ramasamy-Leishman vortex model: a) DLR-HEL-0, b) SpinBlades  $N_b = 1$ , c) SpinBlades  $N_b = 2$ , d) DLR-HEL-18

Figure 5.1 shows the evolution of the maximum swirl velocity as a function of the vortex age for each investigated configuration. The results are compared with the vortex models

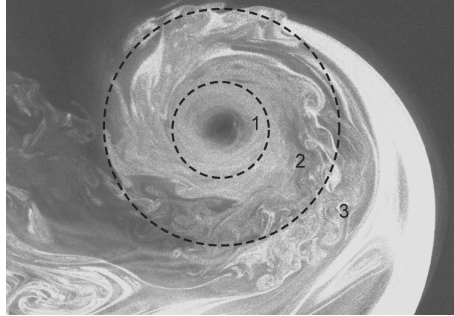


**Figure 5.2.:** Flow visualization of a sample tip vortex, showing distinct flow structures: 1) laminar, 2) transitional and 3) turbulent, Ramasamy et al. (2007)

of Ramasamy et al. (2006) and with the laminar vortex formulation, originally proposed by Lamb (1932) and Oseen (1912), as introduced in Chap. 2.3. Both models depend on the vortex core radius  $r_c$  and the total vortex circulation  $\Gamma_v$ . For both parameters the measured values were used as input. The comparison of the vortex core radius with corresponding models is discussed separately in the following section.

Initially, the measured circulation evaluated at  $r = 0.5 c$  was taken as  $\Gamma_v$  in the Lamb-Oseen vortex model to predict the maximum swirl velocities. This radius is significantly larger than the vortex core and should, under the assumption that circulation converges at large radii, capture nearly the entire vortex circulation.

However, the comparison with the Lamb-Oseen model ( $\odot$ ), which describes laminar and isolated vortices, showed poor agreement with the measurements. This discrepancy was expected, since, as already seen in Fig. 4.10, the experiments did not exhibit a constant circulation for larger vortex radii, in contrast to the Lamb-Oseen prediction of circulation distribution.

In the literature, this continued increase in circulation is commonly attributed to turbulence within the vortex core. Ramasamy et al. (2007) proposed an Ansatz that added an eddy viscosity function across the vortex. Based on flow visualizations (e.g., Fig. 5.2), they assumed that transitional vortices consist of several flow regions: a laminar core, a transitional region, and an outer turbulent region. This leads to a radial variation of eddy viscosity, whereas the Lamb-Oseen model assumes it to be constant. The Ansatz was subsequently fitted to measurements, accounting for turbulence and at the same time reproduced the observed increase in circulation. Vatisas (2006) adopted the fully empirical approach, adjusting their vortex model using the same measurements Ramasamy et al. (2007) used, which lead to a similar outcome.

The results of a decomposition of slipstream and vortex flow fields in Chap. 5.2, however,

indicate that this continued increase in circulation is primarily driven by the slipstream boundary of the wake. This demonstrates that the assumption of an isolated vortex is not consistent with the observed flow field. Instead, the wake shear layer contributes substantially to the vortex circulation, as the downwash on the inner side of the vortex reaches its maximum directly adjacent to the vortex, while the outer region may even exhibit a slight upwash.

To address this discrepancy in vortex circulation definition, the vortex radius at which the Lamb-Oseen model reaches 99% of its total circulation was calculated as follows:

$$\begin{aligned} (1 - e^{(-\alpha_L^2 \bar{r}^2)}) &= 99\% \\ \Rightarrow \bar{r} &= 1.915 \end{aligned} \tag{5.1}$$

The radius of  $1.91 r_c$  was adopted as a new reference for circulation extraction to assess whether this more accurately reflects the maximum swirl velocity. The close agreement of the green markers ( $\Delta$ ) with the measurement data supports this choice.

Nevertheless, this does not imply that the model accurately represents the velocity distribution at larger radii. The Lamb-Oseen vortex requires the circulation to remain constant for larger radii, which in turn implies a  $1/r$  decay in velocity. In contrast, the measurements still exhibit a different behavior, so that the agreement between model and experiment is limited to small vortex radii.

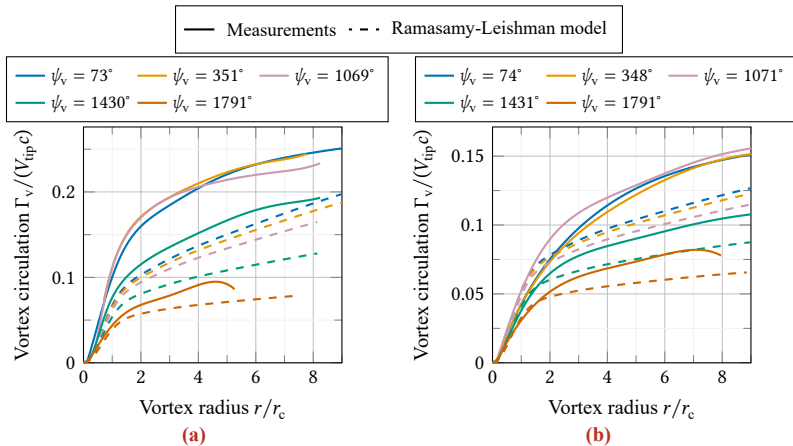


**Figure 5.3.:** Comparison of measured circulation distributions with the Ramasamy-Leishman model: a) DLR-HEL-0, b) DLR-HEL-18

Compared to the laminar Lamb-Oseen model, the Ramasamy-Leishman model is intended to account for the influence of turbulence within the vortex, which was assumed to cause the increase in circulation at larger vortex radii.

However, except for the twisted blade case shown in Fig. 5.1d, the agreement of the Ramasamy-Leishman model (□) with the measurements remained nearly as poor as that of the Lamb-Oseen model using  $\Gamma_{0.5c}$ . Only at very high vortex ages the model started to approach the measured data. A notable weakness of the model lies in the uncertainty in selecting the reference circulation, i.e., the point at which the modeled circulation is constrained to match the prescribed reference value.

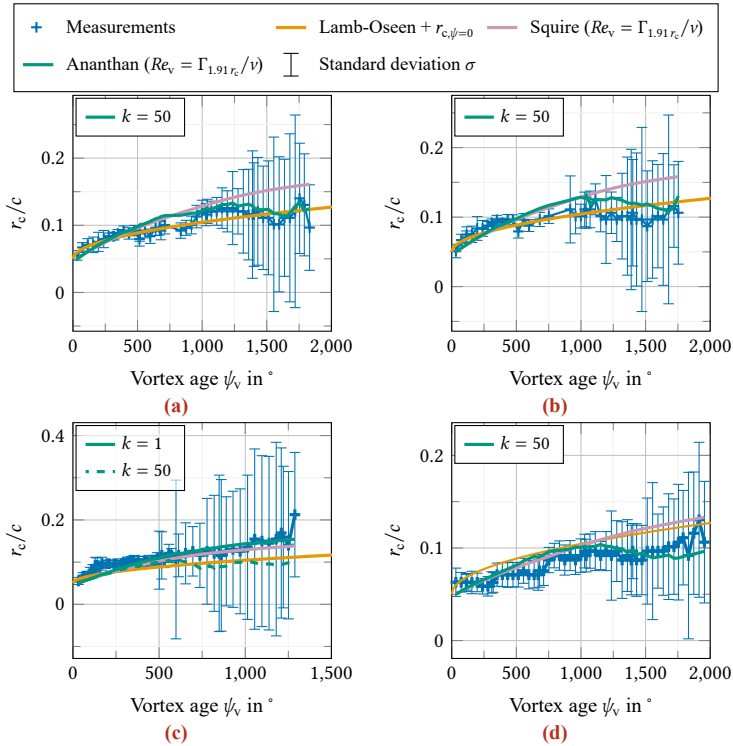


**Figure 5.4.:** Vortex core radius as a function of vortex age, compared with the corresponding Squire and modified Lamb-Oseen vortex core model: a) DLR-HEL-0, b) SpinBlades  $N_b = 1$ , c) SpinBlades  $N_b = 2$ , d) DLR-HEL-18

To illustrate this effect, Fig. 5.3 compares the Ramasamy-Leishman model with the measured

circulation over the vortex radius for several vortex ages. While the model shows reasonably good agreement at smaller radii, it clearly deviates from the measurements at larger radii. Notably, the model does not even reproduce the inserted circulation at  $r = 0.5c$ . This behavior is consistent with the observations discussed in Chap. 2.3.

Figure 5.4 presents the vortex core radius,  $r_c$ , as a function of vortex age, comparing experimental data with several core growth models, including those by Squire, Ananthan, and a modified Lamb-Oseen approach. The standard deviation of the core radius is shown as a measure of the fluctuation level. Note that, due to the skewness of the vortex core radius distribution at higher vortex ages, values below zero appear. These do not represent negative radii but merely indicate strong fluctuations.

As discussed in Chap. 2.3, the specification of an initial core radius is required to enable reasonable comparisons with blade tip vortex measurements. This value is set to  $0.05c$ , which approximately corresponds with the displacement thickness  $\delta_1$  of the used airfoils at the blade tip Reynolds number.

The following discussion begins with the Lamb-Oseen vortex core model. Note, that this model does not inherently include an initial core radius. For this reason, the initial value of  $r_{c,\psi=0}$  was added. With this modification, the model fits well for all one blade configurations, particularly the non-twisted cases. However, for the two blade cases, the Lamb-Oseen core model tends to underpredict the measured radius. This discrepancy may be attributed to the strong vortex pairing observed in the two-blade case, which significantly influences vortex trajectories and is not captured by the Lamb-Oseen formulation.

The Squire model formulation introduces two primary modifications compared to the Lamb-Oseen model. First, it interprets the initial vortex core displacement as an offset along the x-axis (vortex age), rather than the y-axis (vortex core radius). This adjustment reflects the assumption that vortex formation begins upstream of the trailing edge, and the model addresses this by incorporating an offset along the y-axis. Second, the models accounts for additional eddy viscosity by adding a constant factor  $\delta$  in the growth part of the term:

$$\delta = 1 + a_1 \frac{\Gamma_v}{\nu} \quad (5.2)$$

To determine the empirical value of  $a_1$ <sup>1</sup>, Bhagwat et al. (2002) demonstrated the best agreement with experimental data for  $0.00005 < a_1 < 0.0002$ .

For this study, the value recommended by Ramasamy et al. (2007),  $a_1 = 6.5 \cdot 10^{-5}$  was used. Since the vortex circulation decreases with increasing vortex age, the original Squire formulation was modified by integrating over the actual circulation decay, included in  $\delta(\psi)$ , leading to the following expression:

---

<sup>1</sup>Note that the parameter  $a_1$  in the Squire model differs from the  $a_1$  used in the Ramasamy-Leishman model shown in Tab. 2.1

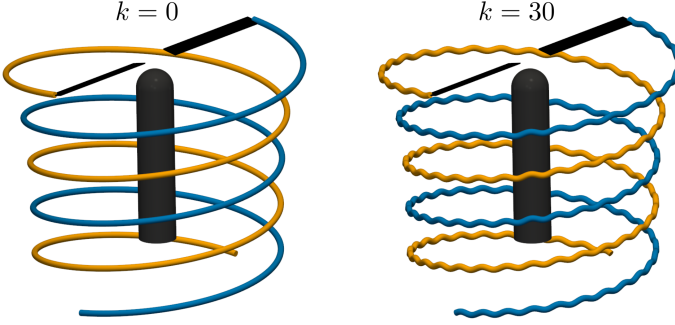


**Figure 5.5.:** Sketch of a harmonic long-wave instability with wave number  $k = 30$  at constant amplitude, affecting the vortex system of a two-blade rotor

$$r_c(\psi_v) = \sqrt{r_{c,\psi_v=0}^2 + \frac{4v\alpha_L^2}{\Omega} \int_0^{\psi_v} \delta(\psi) d\psi} \quad (5.3)$$

Despite the additional information which is included in the Squire model, the overall agreement with the measurement data decreased, compared to the simple implementation of the adapted Lamb-Oseen model. Only in the two-bladed configuration, shown in Fig. 5.4c, an improvement was observed.

Two possible explanations for the observed discrepancies are possible. First, the suggested value of  $a_1$  does not fit for the conducted measurements. A smaller value would improve the Squire model, but the effect is limited, when constrain to the given range ( $0.0002 < a_1 < 0.00005$ ). Second, the Squire model does not account for vortex stretching effects. The Ananthan-Leishman model builds upon the Squire formulation by incorporating an approximation based on mass conservation (see Chap. 2.3). Typically, blade tip vortex trajectories are influenced by two main vortex stretching mechanisms.

The first mechanism is associated with the contraction of the wake, which cause a vortex compression, particularly for low vortex ages. This effect is represented by

$$\varepsilon_{\text{wake}} = \frac{\Delta l}{l} = \frac{r(\psi_v)}{R}. \quad (5.4)$$

The second mechanism is induced by long-wave instabilities, described in Chap. 2.5.2. Figure 5.5 shows the influence of those instabilities for a harmonic wave number on the vortex paths. A reconstruction of the elongation of these paths caused by long-wave instabilities was

proposed by Bartzsch (personal communication): Assuming harmonic perturbations, the vortex tube trajectory is modeled by a sine wave. The length of this wave is given by the integral:

$$L(a, k) = \int_{\mathcal{C}=a \sin(k\varphi)} ds = \int_0^{\varphi} \sqrt{1 + (ak)^2 \cos^2(k\varphi)} d\varphi \quad (5.5)$$

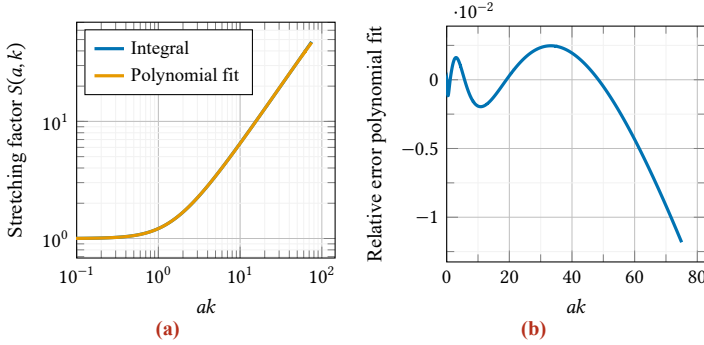


**Figure 5.6.:** Approximation of the stretching factor, due to long-wave instabilities over the product of wavelength and amplitude: a) Polynomial fit and numerical solution of the integral, b) Relative error of the polynomial Fit

The stretching factor  $S(a, k)$  due to long-wave instabilities is calculated by comparing the actual length of the line integral for a circle with the circumference of a quarter wavelength (the smallest periodical length):

$$S(a, k) = \frac{k}{2\pi} \int_0^{\frac{2\pi}{k}} \sqrt{1 + (ak)^2 \cos^2(k\varphi)} d\varphi \quad (5.6)$$

Here,  $a$  denotes the amplitude and  $k$  the wave number. Since this integral can only be solved either by employing the incomplete elliptic integral of the second kind or by numerical integration, a fifth-degree polynomial fit, shown in Fig. 5.6a, serves as a practical analytical approximation and is defined as follows<sup>2</sup>:

$$S(a, k) \approx 1 + 0.00248 \log(ak + 1) + 0.18688 \log^2(ak + 1) + 0.45776 \log^3(ak + 1) - 0.14854 \log^4(ak + 1) + 0.03792 \log^5(ak + 1) \quad , \quad ak \in [0, 71] \quad (5.7)$$

When respecting the given boundaries, the error of the fit remains below 1%, as shown in Fig. 5.6b. For the present measurements only values of  $ak < 10$  are relevant, resulting in an error below 0.2%.

<sup>2</sup>This formulation was derived based on a first proposal of H. T. Bartzsch in a personal communication.

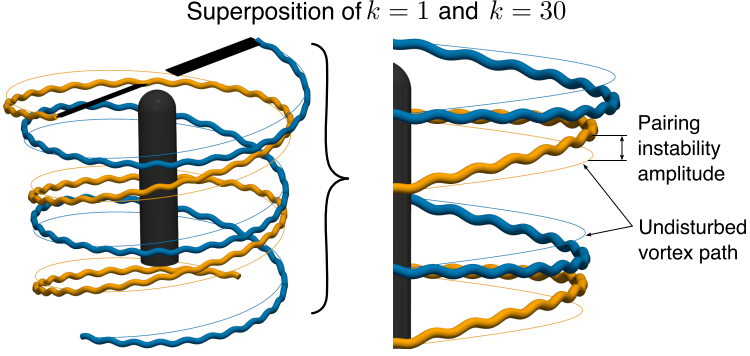


**Figure 5.7.:** Sketch of long-wave instabilities with two superimposed wave numbers  $k = 1$  and  $k = 30$  at constant amplitude, showing their influence on the vortex system (left) and the disturbance amplitude (right)

This results in the modified Anathan-Leishman model:

$$r_c(\psi, a, k, r) = \sqrt{r_{c,\psi=0}^2 + \frac{4v\alpha_L^2}{\Omega} \epsilon_{\text{wake}}(r)^{-1} S(a, k)^{-1} \int_0^\psi \delta(\psi) d\psi} \quad (5.8)$$

Since instantaneous vortex trajectories are not available from the measurement data, an exact solution cannot be derived. Nevertheless, the following analysis demonstrates that with plausible parameter estimates, this formulation is able to model the vortex core growth with good accuracy.

To approximate the amplitude  $a$ , the standard deviation of the vortex trajectory coordinates at a given vortex age is used:

$$a \approx \sqrt{\text{std}(r)^2 + \text{std}(z)^2} \quad (5.9)$$

The wave number  $k$  was not measured in present experiments. However, Shadowgraphy results from other experiments in hover flight, such as the HVAB rotor (Norman et al. (2023)) and full-scale BO105 airborne experiments (e.g., Wolf et al. (2022)), suggest wave numbers between 35 and 50 as reasonable.

Using a wave number of  $k = 50$ , all one-blade cases show good agreement with the corresponding model, as vortex stretching suppresses vortex core growth for older vortices. The two blade case, however, shows a different behavior, with measured core radii lying above the Squire prediction. Since vortex pairing dominates the instability dynamics in this configuration, it is plausible that lower wave numbers, reflecting the pairing process, are more dominant

here. Pairing is typically amplified most strongly at wave numbers of  $k = 0.5 \cdot N_b$  and its odd multiples, where successive vortices are exactly out of phase, see Gupta et al. (1974). To illustrate, Fig. 5.7 shows a reconstruction of long-wave instabilities, superimposing the wave numbers  $k = 30$  and  $k = 1$ . Since higher wave numbers, usually exhibit lower amplitude the measured amplitude mostly is assigned to the pairing instability. Most experiments, e.g., Leweke et al. (2014), have observed the highest amplification for the lowest unstable wave number, see also Chap. 2.5.2. Therefore, a wave number of  $k = 1$  was selected, which yields good agreement with the experimental results.

Despite the good agreement of this empirically tuned vortex model, the objective of the previous section was to illustrate a possible application of the vortex stretching term in the Ananthan-Leishman model. In particular, perturbations in older vortices have a pronounced effect on vortex core growth. Nevertheless, it must be emphasized that the choice of the wave number is guided solely by plausibility considerations and remains uncertain for the present measurements.

## 5.2. Application of Vortex Models on the Fluctuating Flow Field

In the previous section, a potential influence of the wake shear layer on the tangential velocity and circulation of a vortex was observed. For this reason, the present section compares selected sample results obtained by applying the same evaluation procedure to the fluctuating component of the flow field, where the time-averaged flow field is subtracted. This approach was conceived only after the experiment had been completed, and, consequently, the experimental setup exhibits certain limitations.

The most important limitation is that not all azimuth angles contribute equally to the average value. This is primarily due to two factors: First, when blade masking was required, the flow field lacks data in these regions. Second, restrictions in the available laser timing led to a non-uniform distribution of rotor azimuths in the dataset. As a consequence, certain azimuth angles are weighted more heavily than others.

In summary, this section is to explore the hypothesis of wake shear layer influence rather than to provide results meeting the strict accuracy requirements applied in the direct flow-field evaluation. Nevertheless, the data indicate whether the subtraction of the wake shear layer shifts the tangential velocity distribution towards the Lamb-Oseen prediction. This would be an indication that, at least for the evaluated cases, the Ansatz of including eddy viscosity, which shifts the circulation outwards, is not the physical reason for the continued increase for radii larger than  $1.91 r_c$ .

The transformation of the original data to the fluctuating component is shown in Fig. 5.8. A slight inaccuracy becomes visible in the time-averaged data at about  $0.4 z/R$ , caused by blade

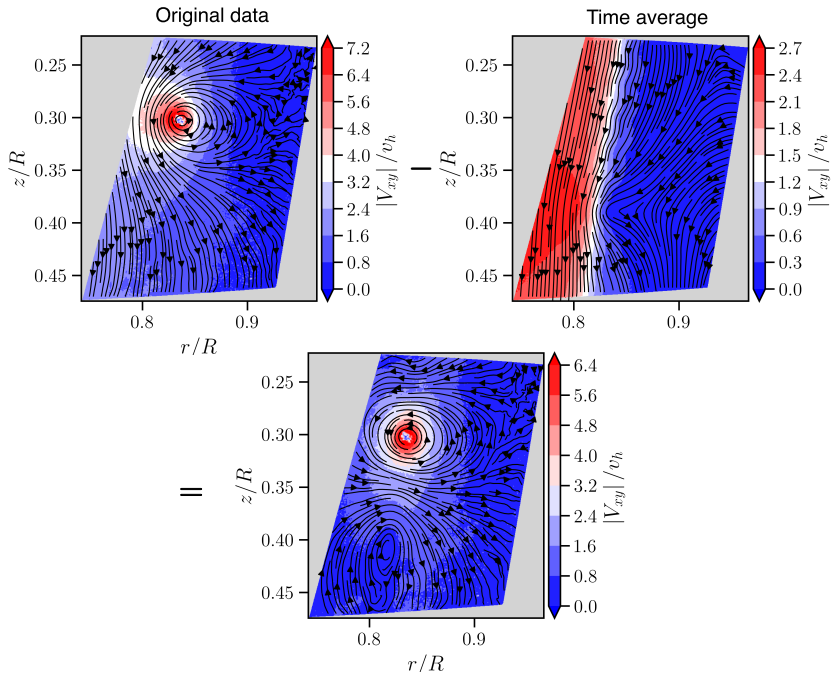


**Figure 5.8.:** Subtraction of the average flow field.

masking but located beyond the evaluated vortex domain for this sample. Outside the wake, this effects the streamlines more strongly due to the overall lower velocities.

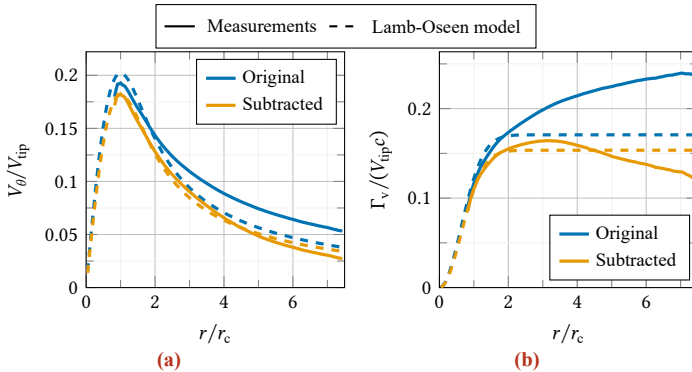


**Figure 5.9.:** Effect on evaluating a mean subtracted flow field on: a) Maximum tangential velocity, b) Circulation

Figure 5.9 shows the influence of this procedure on the sample vortex presented in Fig. 5.8. Note that subtracting the circulation of the mean vortex field at the position of the instantaneous vortex from the instantaneous vortex circulation yields comparable results.

While the original data indicate a significant increase of circulation with vortex radius, the subtracted flow field delivers a vortex which agrees more closely with the Lamb-Oseen model. The circulation reaches a maximum at approximately  $2r/r_c$  after which the circulation decreases again. This decrease reflects the finite spatial extent of vortices in a helical vortex system. In other words, the circulation midway between to consecutive vortices must approach zero again, whereas the Lamb-Oseen model is also able to describe an infinite vortex, a situation that does not occur in reality.

To summarize, if the slipstream velocity distribution, for example obtained from low-order methods, is known, and the associated circulation is added to the Lamb-Oseen vortex model, a reasonable representation of the swirl velocity distribution can be achieved. Despite its usefulness for vortex modelling, the physical interpretation of this approach is limited. Although linear decomposition of flow fields is widely used in aerodynamics, the subtracted flow field does not satisfy the principle of energy conservation. This limitation is reinforced by the findings of Martin (2001), who argued that such a decomposition is physically not permissible, since it is not Galilean invariant and the measured vortices do not reach the bound circulation of the blade.

### 5.3. Behavior of Vortex Voids

When investigating the vortex voids, their behavior appeared counterintuitive. Beyond a certain vortex age, the vortex core growth stops and the large voids begin to collapse inward and occasionally appear<sup>3</sup> to vanish suddenly.

This chapter therefore aims to explain the key mechanisms dominating the evolution of vortex void sizes.

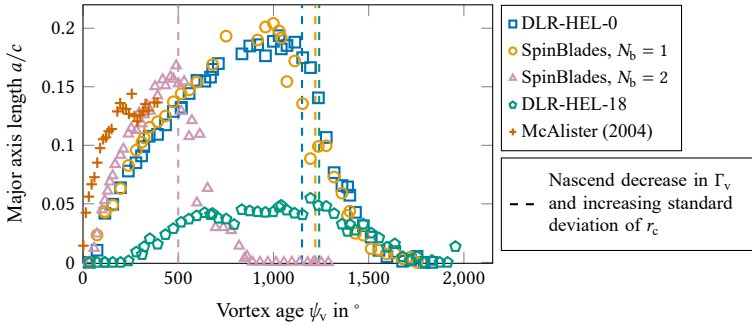


**Figure 5.10.:** Vortex void size over angular velocity for all investigated cases

Figure 5.10 shows the evolution for the major axis length of the vortex void with increasing vortex age, for detail PIV cases. In addition, the measurements from McAlister (2004) are included. Tab. 5.2 provides a brief overview of the key parameters of that experimental setup.

**Table 5.2.:** Operating conditions McAlister (2004)

$N_b$	Twist (linear)	Radius $R$	Rotation frequency $f$	Airfoil	Chord length $c$	Blade loading $C_T/\sigma$
2	$7.6^\circ$	0.958 m	14.5 Hz	NACA0012	104 mm	0.095

The two non-twisted cases DLR-HEL-0 and SpinBlades exhibit very similar voids sizes. As expected, for vortex ages below  $900^\circ$  the void size grows continuously with the vortex age, as particles are subjected to centrifugal forces over an increasing time. This growth, however,

<sup>3</sup>The 10 Hz acquisition frequency was insufficient to resolve the temporal evolution of the void decay. Instead, images corresponding to the same vortex age were compared. As the critical age was reached, two distinct conditions were identified: in some cases, large voids persisted, while in others, the voids had already collapsed. The simultaneous observation of both states at the same vortex age indicates that the collapse of vortex voids occurs as a sudden event.

ends for older vortices before the void vanishes completely. Similar qualitative observations were made for the other two configurations. In the two-bladed case, the slope at young vortex ages is a slightly steeper than for the previously discussed configurations, which is reasonable given the somewhat higher initial circulation. Subsequently, the decrease in vortex void size starts already at  $500^\circ$  vortex age. The highly twisted blade DLR-HEL-18 shows a similar onset of void size decrease, but generally produces smaller voids, due to its overall lower circulation.

The sharp reduction in void size coincides in all measured cases with a decrease in vortex circulation and an increasing standard deviation of the vortex core radius, as marked by the vertical lines in Fig. 5.4. This suggests a relationship of vortex and void decay. A plausible explanation for the sudden decrease is a laminar/turbulent transition of the vortex. By analogy with a turbulent boundary layer, one may argue that turbulent vortices exchange momentum and mass with the outer flow, generating a radial velocity component that causes particle injection and also accelerates vortex decay.

The comparison with the experimental data from McAlister (2004) is limited, since the setup differed slightly and only young vortices were investigated. For this reason, no decrease in circulation or void radius was observed. Nevertheless, some comparisons can be made. The initial slope is slightly steeper for young vortices, possibly due to the higher blade loading. At somewhat older vortices, a plateau was reached, indicating a slower growth, even though the circulation remained high and should have continued to influence vortex void growth.

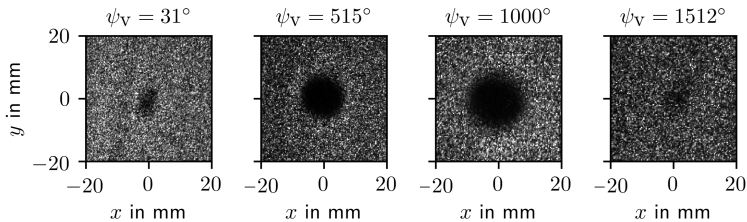


**Figure 5.11.:** Void decay of DLR-HEL-0

Figure 5.11 shows representative particle images at various vortex ages in the vortex-centered coordinate system, with the vortex center located at the origin. The initial void growth is clearly visible, producing a void with a sharp boundary between seeded and non-seeded regions at  $\psi_V = 1000^\circ$ . At  $\psi_V = 1512^\circ$ , the seeding density in the vortex center is still reduced, but a well-defined void is no longer discernible.

# 6. Combined Vortex Investigations

After discussing primary blade tip vortices in selected cases, this chapter presents the combined analysis of configurational and operational influences on primary vortex decay and secondary vortex formation. It is thus organized according to configurational changes or a specific behavior of the flow field, depending on the effect which is to be described. Parts of this chapter were published in Heintz et al. (2023) and Heintz et al. (2025).

## 6.1. Numerical Methods

Selected configurations were also investigated numerically by our DFG project partner, the Institute of Aerodynamics and Gas Dynamics (IAG) at the University of Stuttgart. Since some of these simulation results are included in the subsequent discussion, a brief description of the applied CFD methods are provided here. Additional details of the numerical results are published in Gajo et al. (2024) and Gajo et al. (2025).

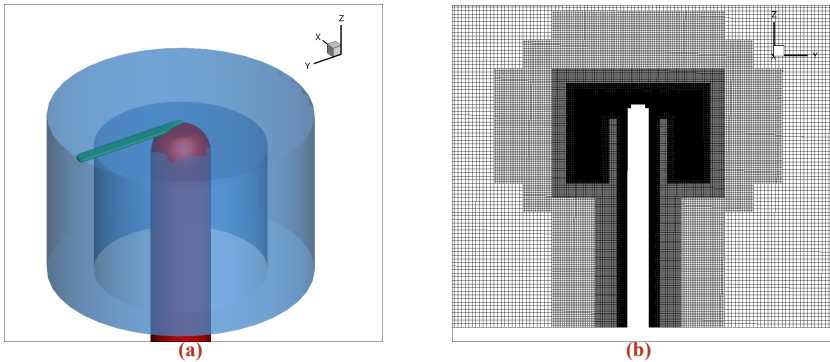


**Figure 6.1.:** Computational meshes for the numerical simulations, reproduced from Gajo et al. (2025) with permission: a) Overview of the individual meshes used, b) Cartesian background mesh

All numerical simulations were carried out using the block-structured CFD solver FLOWer.

This solver, originally developed by DLR and later adapted for rotor applications by IAG, solves the unsteady Reynolds-averaged Navier Stokes (RANS) equations. A sixth-order spatial and second-order temporal discretization was applied to reduce numerical dissipation in the strong shear layers of the rotor wake. For the present simulations a DDES-SST ( $k - \omega$ ) scheme was used with a time step of  $\Delta\psi = 0.25^\circ$

To enable the use of a Cartesian grid, the computational domain was divided into three subdomains, as shown in Fig. 6.1a: a rotating near-blade sub-mesh (green), a stationary displacement body sub-mesh (red), and a stationary Cartesian background mesh (blue). Both near-wall sub-meshes were generated with a  $y^+ = 1$ . The background sub-mesh has a grid spacing of  $3\% c$  in the expected wake region, with a progressive increase toward the outer boundary of the mesh. The sub-meshes were coupled at each time step using the Chimera method. The resulting total number of nodes ranged from  $2.88 \cdot 10^8$  for the one blade rotor to  $2.92 \cdot 10^8$  for the four blade case, see Gajo et al. (2024).

The post-processing of the numerical data also differed in several points, as described in detail in Gajo et al. (2025). These differences primarily arise from the distinct data structures (CFD provides full 3D volumes at a few time steps, while experiments deliver 2D planes across many time steps) as well as from the differences in spatial resolution of the flow field. All adjustments to the post-processing are explained alongside the discussion of the affected results.

## 6.2. Configurational Parameter Study

This section presents the results of the parameter study and works out contributing configurational parameters on vortex decay and secondary vortices. Table 6.1 summarizes the presented configurations including the according section, where their influence is discussed.

### 6.2.1. Influence of the Blade Number

Airborne experiments on helicopters with different blade numbers have shown significant differences in vortex decay, see e.g., Braukmann et al. (2023). Therefore, the first part of the discussion will concentrate on the influence of the blade number on the primary vortex breakdown. A further research question is, to what extent the assumed early breakdown is also connected to a different appearance of secondary structures. All investigated cases are also compared with numerical results.

Initially, the focus lies on the primary blade tip vortex decay. Figure 6.2 shows the different behavior of the blade tip vortex trajectory. The light markers show individual experimental data points for a single measurement case and for a given vortex age. Dashed lines correspond to a fifth-order spline fit of the experimental data, see Chap. 4.1.1 and Fig. 4.6d for further

**Table 6.1.:** Investigated parameters and corresponding cases. The table also lists the sections where their influence on vortex decay and secondary structures is discussed.

Number of blades $N_b$	Rotation frequency $f$	Blade	Blade loading $C_T/\sigma$	Pitch offset $\Delta\theta$
<b>Chap. 6.2.1: Influence of the Blade Number</b>				
1,2,4	18.85 Hz	SpinBlades	0.085	0°
<b>Chap. 6.2.2: Influence of Blade Pitch Offset</b>				
2	18.85 Hz	SpinBlades	0.085	0°, 0.25°, 0.5° and 1°
<b>Chap. 6.2.3: Influence of Vortex Pairing</b>				
2	18.85 Hz	SpinBlades: parabolic and rectangular	0.085	0°
<b>Chap. 6.2.4: Influence of Blade Loading</b>				
1	18.85 Hz	SpinBlades	0.059, 0.07, 0.08, 0.097, 0.106	0°
<b>Chap. 6.2.5: Influence of Blade Geometry</b>				
1	18.85 Hz	SpinBlades, DLR-HEL-0, DLR-HEL-18	0.085	0°
<b>Chap. 6.2.6: Influence of Blade Passing Frequency</b>				
All parameters				

details. The solid lines represent the numerical results. Note that the blade tip position is slightly above the hub position ( $y = 0$ ) due to blade bending and play in the blade mounting, hence, the tip vortex trajectories may start at positive  $z$ -values.

For the one-blade case (Fig. 6.2a) with the default blade loading of  $C_T/\sigma = 0.08$ , both the experimental and numerical trajectory follow agree well. The initial contraction kinks due to the downward acceleration caused by the downwash of the following blade at a vortex age of about  $360^\circ$ . The trajectory then continues in a relatively linear path until the end of the detection.

The trajectories of the two-blade case (Fig. 6.2b), however, show significantly more vortex interaction. As the downwash of the following blade interacts with the tip vortices, the experimental trajectory splits into two curves. The inner vortex follows the path of the single-blade case until about  $0.5z/R$ , the outer vortex is deflected to larger radii. This separation leads to vortex pairing at about  $0.6z/R$ , where the two vortex paths cross. This also leads to a reduction of the distance between the paired vortices, due to the downward acceleration of

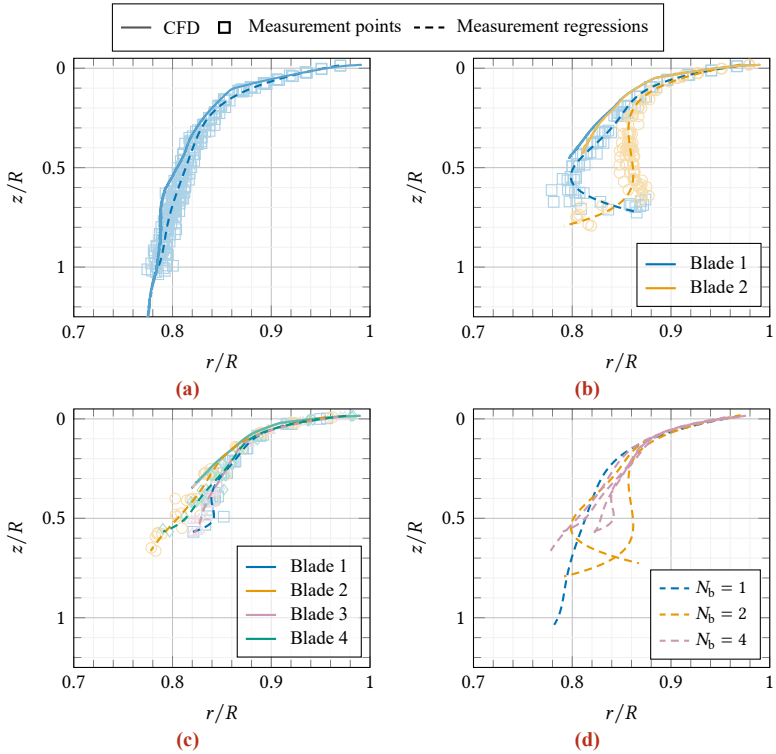


**Figure 6.2.:** Blade tip vortex trajectories for cases with different  $N_b$ : a) One-blade case, b) Two-blade case, c) Four-blade case and d) Comparison between different numbers of blades

the outer vortex induced by the circulation of the inner one and vice versa. The earlier decay compared to the one-blade case is consistent with the observations of Quaranta et al. (2015) and can be attributed to the high receptivity of helical tip vortices to asymmetries, where even minor initial perturbations are sufficient to induce long-wave vortex instabilities, leading to vortex pairing. A one-bladed configuration thus minimizes the asymmetry.

The numerically predicted trajectories deviate significantly from the measurements. Most prominently, the numerical results do not exhibit such a strong vortex pairing as observed in the experiments. A similar behavior was reported by Bodling et al. (2024) and Schwarz et al. (2022) and, according to Bodling et al. (2024), can be attributed to imperfections in the experimental vortex pitch adjustment. In fact, Bodling et al. (2024) demonstrated that an artificially introduced pitch offset also triggers vortex pairing in CFD simulations. When this absence of pairing is considered, the agreement between experiment and CFD appears reasonably good. The slightly weaker contraction of the inner experimental trajectory compared with both blades in the simulations is most probably caused by mutual vortex-vortex interactions.

Note that the vortex identification for older vortices in the simulation was significantly more challenging, thereby shifting the end of detection to lower vortex ages compared with the experimental evaluation. The main reason for this is the strong decrease of velocity gradients within the vortex core due to numerical dissipation, which reduces the resultant vortex criteria below the detection threshold. A possible solution would be the use of adaptive mesh refinement (AMR) methods, which increase the resolution in flow regions with high gradients. Due to the additional computational effort, this was not tested so far.

The four-blade case, shown in Fig. 6.2c, does not exhibit a clear pairing behavior. However, below  $z/R \approx 0.3$ , the trajectories separate into two groups: blades one (—) and three (—) follow the outer path, whereas blades two (—) and four (—) remain on the inner path. Owing to the subsequent vortex decay, it remains uncertain whether this grouping indicates the onset of vortex pairing at this location. The numerical data exhibit a similar trend to the experimental results, which is consistent with expectations, since vortex pairing was already absent in the two-blade configuration.

When comparing all experimental regressions (see Fig. 6.2d), most of the vortex trajectories agree quite well with each other. The pairing of the two-blade case leads particularly to a different behavior of the outer vortex part, although this vortex interaction does not lead to an earlier vortex decay. By contrast, the four-blade case shows an earlier vortex breakdown than the other two configurations.

Figure 6.3a shows the circulation of the discussed cases, as a correlation between vortex breakdown and a decrease in circulation is expected. Before discussing the results, it is noted that the vortex core radii in the CFD simulations are approximately 60 % to 80 % larger than those observed in the experiments. This discrepancy is most likely due to the limited numerical resolution of the background grid. To compensate, the evaluation radius was increased to  $0.8c$  so that the initial circulation of the one-blade case matched between experiment and simulation. This adjustment, however, caused a drop in circulation when the vortex interacted with the

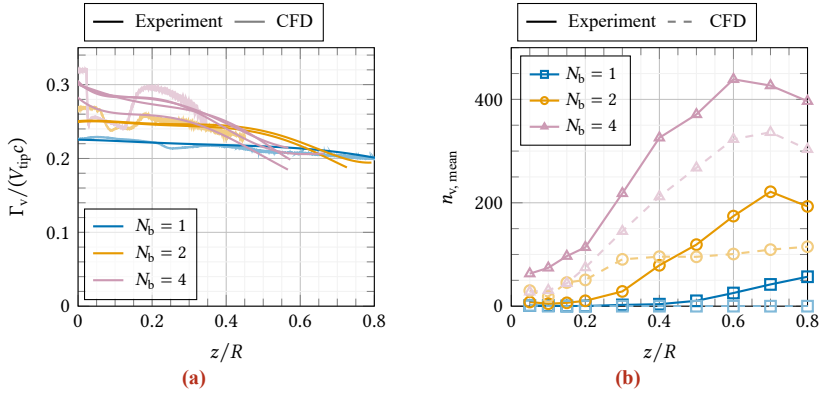


**Figure 6.3.:** Primary blade tip vortex circulation  $\Gamma_v$  (a) and detected secondary vortices per revolution  $n_{v, mean}$  (b) for different numbers of blades

blade shear layer of the subsequent blade. This effect is particularly pronounced for the two- and four-blade configurations at about  $\psi_v = 180^\circ$  and  $\psi_v = 90^\circ$ , respectively. Further details on this behavior are discussed in Gajo et al. (2024).

Most prominently, Fig. 6.3a highlights the dependence of the initial circulation on the blade number for both CFD and experiments, despite a constant blade loading. This difference arises from the dependence of tip-loss on the number of blades, e.g., shown in the tip-loss approximation function by Betz et al. (1919). A higher tip-loss factor leads to a stronger concentration of bound circulation near the blade tip, which in turn increases the circulation shed into the trailing tip vortices, assuming a constant blade loading.

Turning to the circulation further downstream, the experiments and CFD simulations agree exclusively for the one-blade case, which shows a slight decrease in circulation and an almost constant slope across the entire range. This behavior is consistent with the undisturbed vortex trajectories discussed earlier and the absence of a clear breakdown event.

For the two-blade configuration, experiments and simulations diverge more noticeably. In the experiments, vortices from both blades exhibit a nearly constant plateau up to around  $0.4 z/R$ , after which the circulation begins to decrease. This decline coincides with the onset of strong vortex pairing, observed in Fig. 6.2b. In contrast, the numerical simulation shows a slight decrease in vortex circulation up to their detection limit at about  $0.45 z/R$ . Additionally, the initial circulation is slightly higher than in the experiments.

In the four-blade case, the discrepancy in initial circulation between experiment and simulation is even more pronounced. The subsequent numerical results are strongly influenced by the

blade shear layer. However, when focusing on the regions outside this initial drop, the slopes of the experimental and numerical curves are comparable. The onset of a more pronounced circulation decrease occurs at approximately  $z/R = 0.3$  in both cases, although the detection limit in the simulation is reached shortly thereafter.

Figure 6.3b shows the average occurrence of secondary vortices  $n_{v,\text{mean}}$  in different planes below the rotor for several numbers of blades. Note that the threshold for evaluating the numerical data was adapted. Because the  $Q$ -criterion depends quadratically on spatial velocity gradients, it is highly sensitive to grid resolution. Coarser grids tend to low-pass filter the gradients, thereby reducing their magnitudes. Experimental and numerical studies on sample secondary vortices with different vector spacings have shown an approximately linear dependence of peak values. For this reason, the threshold for secondary vortex detection was scaled with the vector spacing ratio between experiments and CFD, see also Gajo et al. (2025):

$$Q_{\text{thr, CFD}} = Q_{\text{thr, Exp.}} \frac{\text{Vector Spacing Exp.}}{\text{Vector Spacing CFD}} \quad (6.1)$$

The measurements show that the number of detected secondary vortices increases with the blade number. When comparing the occurrence of secondary vortices with the primary vortex circulation, no correlation is observed between the circulation collapse and an increase in detected secondary structures. Thus, newly created secondary vortices in the surrounding regions of a previous blade tip vortex are not a result of vortex fragments splitting from unstable blade tip vortices. This is evident at least in the case of a four-blade configuration. Although the number of blades has a significant influence on secondary vortices, no single parameter could be defined as the main contributor. This is because altering the number of blades simultaneously affects several parameters, including vortex spacing, circulation, and blade passing frequency.

The CFD captures the overall trend of stronger secondary structures with increasing blade number, but underestimates their magnitude compared to the experiments. Consistent with the measurements, the simulations also reveal no correlation between the reduction in circulation of the primary blade tip vortices and the increase in secondary vortices. A plausible explanation for the underprediction of  $n_{v,\text{mean}}$  is that the adapted CFD threshold  $Q_{\text{thr, CFD}}$  does not fully compensate for the effects of the coarser resolution.

## 6.2.2. Influence of the Blade Pitch Offset

In addition to the number of blades, Schwarz et al. (2022) suggested that the blade pitch offset could influence the occurrence of secondary structures. The blade pitch offset is defined as the difference between the individual pitch angles of the blades, while the mean pitch angle is kept constant, see also Chap. 3.2.1. Such blade-to-blade pitch differences are likely to occur in experimental studies, for example, due to play in the swashplate components or due to the differing elastic behavior of the blades. This is particularly relevant for handmade blades

and non-isotropic materials, as used in this study. In full-scale helicopters similar effects may also arise, since track-and-balance procedures are generally limited to adjustments of blade tip height and lead/lag behavior rather than exact pitch alignment. Hence, a study with intentionally introduced pitch offsets was conducted, allowing to investigate their influence on the wake flow.

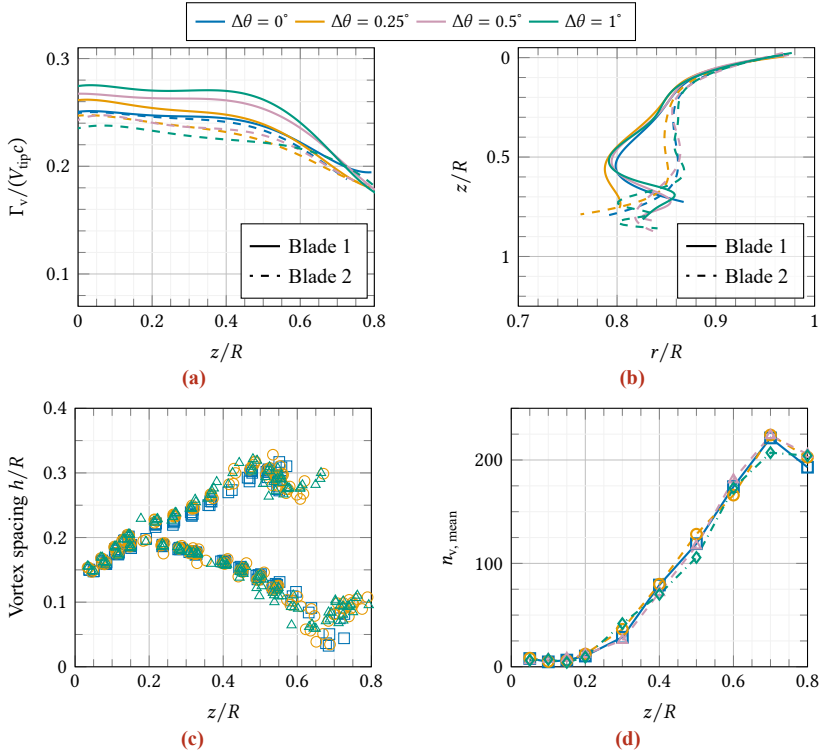


**Figure 6.4.:** Influence of blade pitch offset  $\Delta\theta$  on: a) Primary blade tip vortex circulation  $\Gamma_v$ , b) Blade tip vortex trajectories, c) Average blade tip vortex distance for each azimuth in each conducted measurement over the mean  $z$ -distance and d) Detected secondary structures and course of the primary vortex circulations

To demonstrate the precision and accuracy of the pitch trimming, the vortex circulation of the trailing blade tip vortices is plotted in Fig. 6.4a. For the trimmed case (pitch offset  $\Delta\theta = 0$ ) the vortex circulation of blades one and two is found to be in good agreement, indicating that the pitch setting is accurate. As the pitch offset increases, the gap in between the vortex

circulations of the two blades also increases.

Figure 6.4b shows the impact on the blade tip vortex trajectories. A small offset shifts the pairing to a younger vortex age. Nevertheless, this effect is constrained to the inner vortex trajectory and quite small. Even by reversing the pitch offset, we were unable to eliminate the pairing, so the pitch offset is not the only contributing factor to vortex pairing. For example, less vortex pairing was observed for a rectangular blade shape. This is discussed in detail in Chap. 6.2.3.

Although a change in pitch angle usually alters the vortex spacing, this effect was not observed in the present experiment, see Fig. 6.4c. A likely explanation is that vortex pairing dominates the wake dynamics and enforces a stable trajectory. As already noted for the vortex trajectories, the blade pitch offset has no significant influence on the path of the trajectories. Applied to the vortex spacing, the conclusion is that vortex pairing effects are so dominant that they override other parameters such as the blade pitch. Similarly, no detectable effect on the formation of secondary vortices was found (Fig. 6.4d). This is consistent with the numerical findings of Bodling et al. (2024). To summarize, the effect of blade pitch offset on the vortex breakdown does not appear to be a dominant factor.

### 6.2.3. Influence of Vortex Pairing

The pitch offset variation in the previous section intended to alter or suppress the blade tip vortex pairing, and to study the resulting influence on the secondary vortices. Even though no effect was observed, a strong influence of the blade tip geometry on the pairing process for the two-bladed rotor was found.

Comparing the trajectories of the rectangular blade tip shape (Fig. 6.5a) with those of the parabolic blade tip (Fig. 6.5b) shows that the rectangular blade tip shape leads to much less pairing. One possible reason for this are instabilities in the blade tip vortex generation.

In general, a wing tip vortex forms through the merging and roll-up of multiple discrete vortices that arise due to changes in lift and the associated pressure compensation, see e.g., Luckring (2019). For a parabolic blade tip planform, this process extends along the curved tip and leads to a gradual merging of vortices over a larger radial range. In contrast, a rectangular blade tip ends abruptly, restricting the roll-up process to a narrow region and producing more sharply defined vortices. This confinement is expected to suppress the development of certain instability modes compared to the parabolic blade tip. Supporting evidence comes from numerical studies on the shape of fixed wing tips, e.g., Freed et al. (2025), which demonstrated a significant influence of tip-edge geometry on vortex formation.

An alternative hypothesis is that the blade tip shape influences the initial vortex core size. From generic experiments on co-rotating vortices, it is known that the core size plays a key role in vortex interaction and vortex pairing mechanisms, see Meunier et al. (2005). However, for

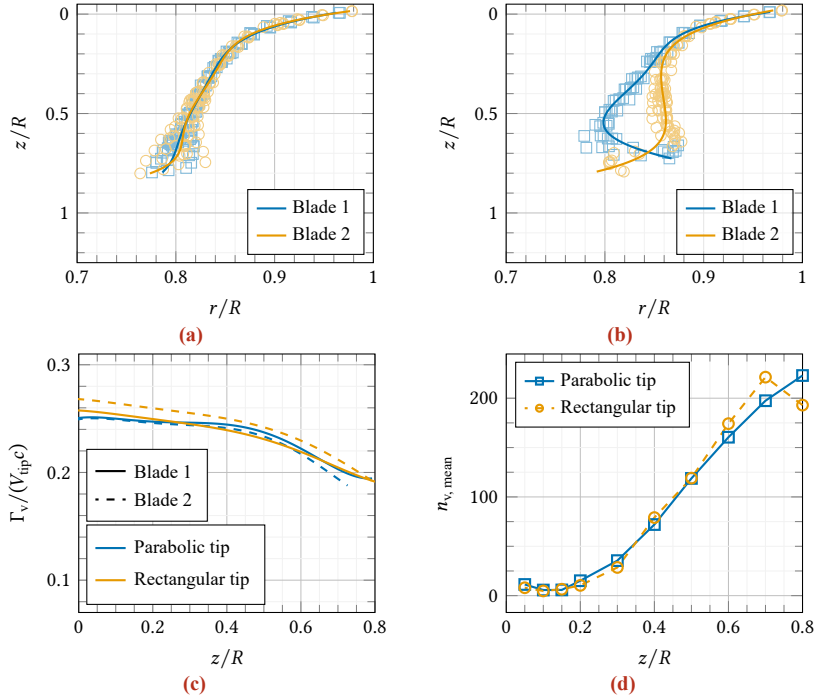


**Figure 6.5.:** Comparison between a case with strong vortex pairing (parabolic blade tip shape) and with weak vortex pairing (rectangular blade tip shape): a) Vortex trajectory for a two-blade configuration with rectangular blade tip shape, b) Vortex trajectory for the default parabolic configuration, c) Primary blade tip vortex circulations  $\Gamma_v$ , d) Detected secondary structures

the configuration with the rectangular blade tip shape, no high-resolution PIV measurements were available, to also resolve vortex core size. The overview PIV configuration was not designed to provide a detailed velocity field for very young blade tip vortices.

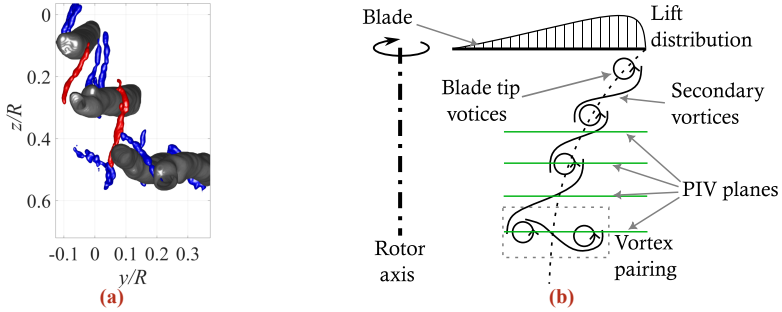


**Figure 6.6.:** Vortex system below a rotor. a) STB measurement adapted from Wolf et al. (2019b) of a vortex system with blade tip vortex pairing, b) Scheme of the secondary vortices, when vortex pairing occurs.

Prior to comparing the detected number of secondary vortices, Fig. 6.5c proves that there is no considerable impact on vortex circulation in the rotor wake due to the change in lift distribution over the blade.

Although the present study does not provide a comprehensive analysis of the relation between tip shape and vortex stability, this case provides a useful basis for assessing how vortex interaction influences the occurrence of secondary vortices. Figure 6.5d indicates that this influence is negligibly small.

However, the three-dimensional measurements by Wolf et al. (2019a), shown in Fig. 6.6a, suggest an influence on the azimuthal distribution of secondary vortices. To illustrate, Fig. 6.6b sketches their expected formation between paired blade-tip vortices, where they tend to form in the vicinity of the primary vortices. When vortex pairing occurs, as in the two-blade case (SpinBlades), the two primary vortices no longer lie in a plane with a  $180^\circ$  phase shift but instead move azimuthally closer together. Consequently, the distribution of secondary vortices should also change, although their total number remains approximately constant.

To analyze this behavior Fig. 6.7 shows the azimuthal distribution of secondary vortices in relation to the primary blade tip vortex position. The  $x$ -axes are normalized with respect to the azimuthal position of the primary vortex originating from the first blade, thereby illustrating the phase shift of the other vortex. Phase shifts exceeding  $270^\circ$  are wrapped to negative values to improve readability of the secondary vortex distribution.

At  $0.2 z/R$  (Fig. 6.7a and Fig. 6.7b), both blade tip shapes exhibit two peaks of secondary

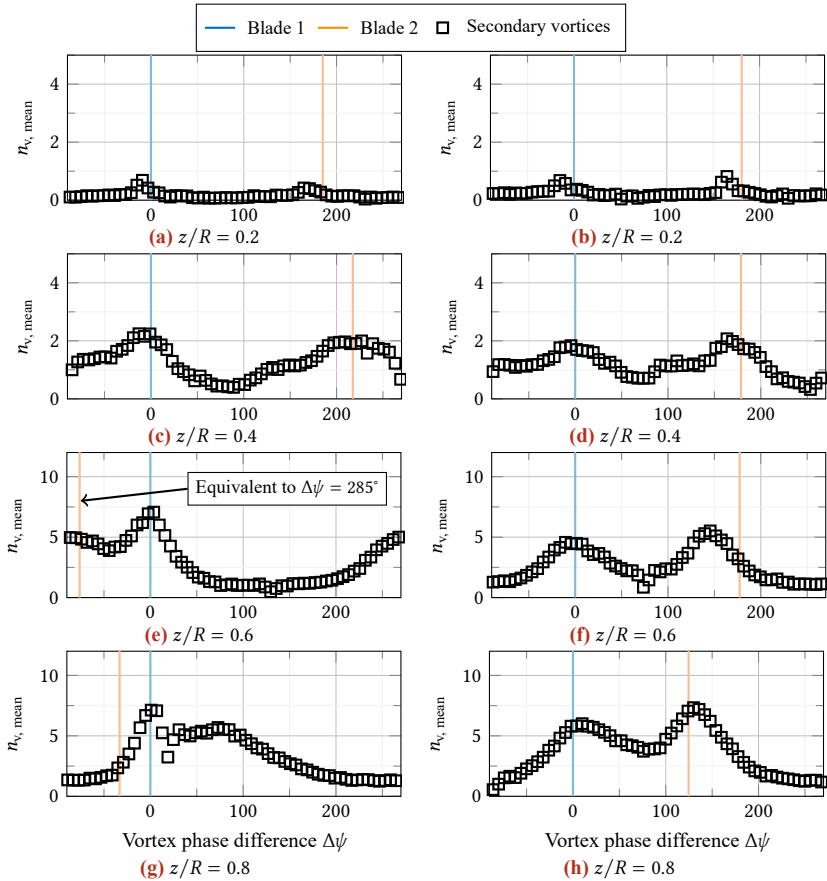


**Figure 6.7.:** Azimuthal distribution of secondary vortices in one plane and corresponding blade tip vortex positions for a case with strong vortex pairing or parabolic blade tip shape (a, c, e, g) and with weaker vortex pairing or rectangular blade tip shape (b, d, f, h)

vortices with a phase shift of about  $180^\circ$ . These positions correspond to the azimuthal locations of the blade tip vortices, marked in orange and blue, where the vortices intersect this  $z/R$ -plane, as also observed in the vertical PIV planes.

For the parabolic blade tip, the peak in secondary vortices gradually shifts with the primary vortex position (Figs. 6.7c, 6.7e). In Fig. 6.7e the phase shift exceeded  $270^\circ$  and is for illustration purposes wrapped to approximately  $-75^\circ$ , which is an equivalent measure to  $285^\circ$  phase shift. At a height of  $0.8z/R$ , shown in Fig. 6.7g, the vortex pairing reduces the phase shift to approximately  $-40^\circ$ , indicating that the tip vortices have almost switched places. Correspondingly, the two peaks of secondary vortices merge as the primary vortices approach the same plane.

For the rectangular tip, the phase shift between the primary vortices remains nearly constant up to  $0.6z/R$ , while the secondary vortices accumulate around them. Even at  $0.8z/R$ , shown in Fig. 6.7h, only a small shift from approximately  $180^\circ$  to about  $125^\circ$  is observed. This reflects the weaker vortex interaction in this case, and accordingly, the two peaks of detected secondary structures remain distinct.

In summary, vortex interaction clearly influences secondary vortices. This effect is not seen in their overall number  $n_{v,\text{mean}}$ , but rather in their azimuthal distribution.

## 6.2.4. Influence of the Blade Loading

So far, it was found that neither a blade pitch offset nor a blade tip vortex interaction is the driving factor of the occurrence of secondary vortices. For this reason, the next investigation is done using a single bladed rotor with varying blade loading by changing the pitch angle, to investigate the effect of blade tip vortex spacing. The variation in blade loading causes a change of blade tip vortex spacing and primary vortex circulation, without affecting the rotation frequency or the blade number. As it was unclear to which extent the influence of vortex pairing is negligible, the investigations were mainly carried out on a one-blade rotor with the object of minimizing potential impact of vortex interactions.

Figure 6.8a shows the vertical tip-vortex spacing of the one-bladed rotor for different blade loadings as a function of the  $z$ -position. Although a considerable variation was achieved, the comparison with Fig. 6.9 indicates that it is still smaller than the variation caused by changing the number of blades. Nevertheless, the variation in vortex distance is sufficient to study its influence on secondary vortices.

Theoretical considerations also suggest that blade loading and vortex circulation are proportional, since blade element theory predicts that blade loading is proportional to the maximum bound circulation for a given circulation distribution (i.e., blade geometry). According to lifting-line theory, the vortex circulation should therefore correspond with the maximum bound circulation. This behavior is indeed observed in Fig. 6.8b, where the primary vortex circulation

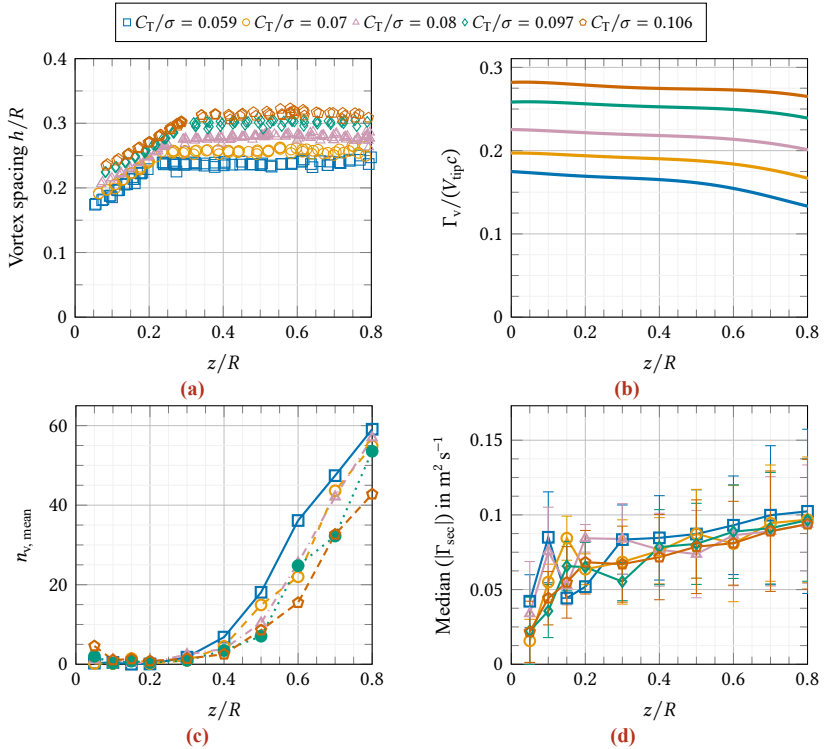


**Figure 6.8.:** Influence of blade loading  $C_T/\sigma$  on: a) Average blade tip vortex distance over the mean  $z$ -distance, b) Vortex circulation, c) Detected secondary vortices, d) Median of absolute secondary vortex circulation

scales approximately linearly with blade loading. Moreover, the slope of circulation is very similar across cases, although a reduction in blade loading tends to cause a slightly steeper decrease in vortex circulation. A plausible explanation is that reduced blade loading leads to vortices of greater age at the same distance from the rotor plane.

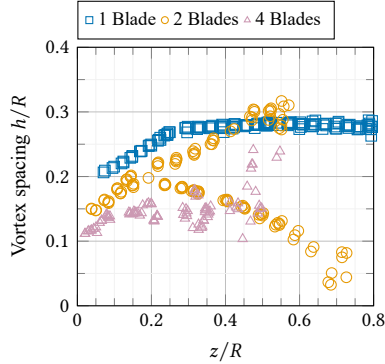


**Figure 6.9.:** Average blade tip vortex distance over the mean  $z$ -distance for different numbers of blades  $N_b$

Figure 6.8c shows the influence of blade loading on secondary vortices. A reduction in blade loading, and thus in vortex spacing and circulation, leads to a higher number of secondary vortices. Although the effect is not as strong as that of changing the number of blades, the influence on secondary structures is evident.

Compared with the other parameter studies discussed so far, this is the first case, aside from the blade-number variation, where a measurable trend can be identified. While vortex spacing does not appear to be the primary factor behind the differences in secondary-structure occurrence between rotors with different blade counts, it is certainly a subordinate one.

Interestingly, the median of the absolute secondary vortex circulation, shown in Fig. 6.8d, exhibits only slight variations across the measured blade loadings. A tendency can be observed in which a reduction in blade loading, and thus in primary vortex circulation, is accompanied by a slight increase in secondary vortex circulation. This observation further indicates that the two circulations are not directly dependent.

## 6.2.5. Influence of the Blade Geometry

Until now, the investigations only focused on a single blade geometry. This chapter discusses the impact of blade design variation on secondary vortex decay. As shown in Fig. 3.7 the blade

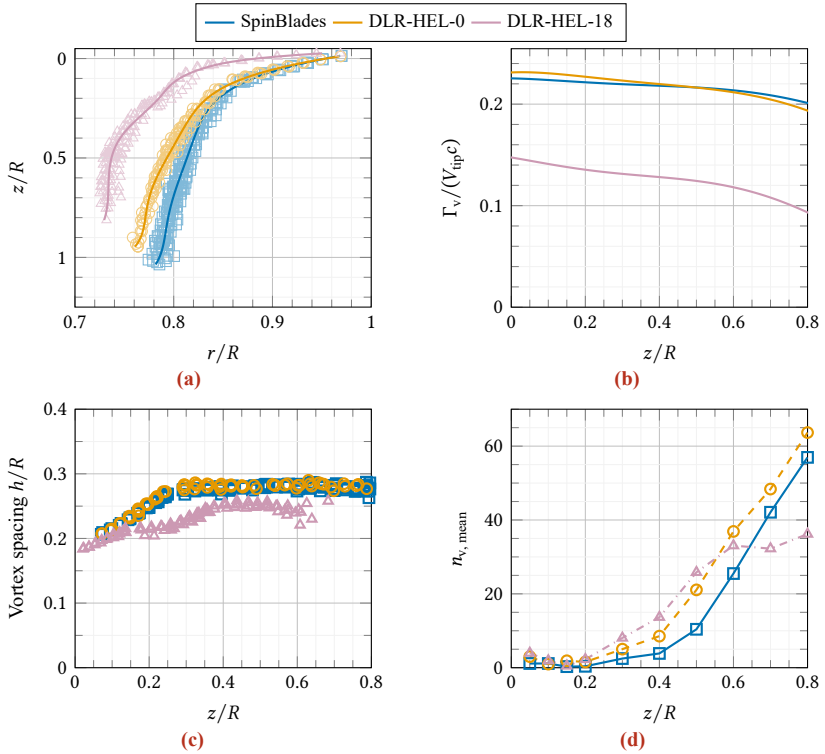
design was modified to a generic own-design with a lift producing airfoil (NACA23015) in contrast to the symmetric airfoil (SpinBlades parabolic and rectangular). The own-designs have a rectangular tip shape and have been measured with a linear twist of  $-18^\circ$  (DLR-HEL-18) and again in an untwisted version (DLR-HEL-0). The design objective of these generic blades is to use a well-known airfoil together with an easily reproducible geometry. Detailed information on blade design is given in Chap. 3.2.1.

Figure 6.10a shows the trajectories of the DLR-HEL blades in comparison with the SpinBlades parabolic blade. In general, negative twists reduce thrust at higher rotor radii and consequently produces a stronger wake contraction. This impact of twist is also captured by the prescribed wake model of Kocurek et al. (1977). Accordingly, the vortex trajectory of the twisted DLR-HEL-18 ( $\blacktriangle$ ) exhibits a much stronger contraction compared with the SpinBlades configuration ( $\square$ ). The DLR-HEL-0, although untwisted by design, still shows a slightly increased contraction, particularly after the first blade passage. This behavior can be attributed to the momentum coefficient of the NACA 23015, that is more than twice as high as that of the other blades, combined with its slightly higher flexibility. This results in an increased torsion towards a negative twist.

Regarding the vortex circulation, which is plotted in Fig. 6.10b, the strong twist of the DLR-HEL-18 blade leads to a weaker pressure gradient at the rotor tip and, consequently, to a reduced vortex circulation. The achieved circulation of about  $\Gamma_v \approx 2C_T/\sigma$  agrees well with the theoretical prediction of blade element theory for ideally twisted blades. For the untwisted blades DLR-HEL-0 and SpinBlades, the evolution of the vortex circulation is very similar. The slight discrepancy in the initial circulation is a result of the influence of the blade geometry towards a change in the lift distribution.

The reduced circulation on the outer part of the DLR-HEL-18 rotor is also been noticed in the vortex spacing shown in Fig. 6.10c. In contrast to the SpinBlades and the DLR-HEL-0 rotor, which exhibit identical vortex spacing over the entire vortex age, the DLR-HEL-18 has a significantly smaller vortex spacing, particularly within the range between  $0.2 z/R$  and  $0.4 z/R$ . Interestingly, however, this approaches the level of the other two rotor blade designs for larger vortex ages.

Figure 6.10d illustrates the influence of the blade design on the formation of secondary structures. Both DLR-HEL rotor designs exhibit a higher number of secondary vortices than the SpinBlades at rotor distances up to about  $0.5 z/R$ . This observation is consistent with the findings presented in Chap. 6.2.4, where a reduction in vortex spacing also led to slightly more secondary vortices. For older vortices, however, the DLR-HEL-18 no longer shows an increase in the further course and thus even has fewer detected structures from  $0.7 z/R$  onwards. This can be attributed to the earlier onset of vortex decay for this blade. In contrast, the DLR-HEL-0 continues its course parallel to the SpinBlades configuration up to the oldest detected position. This shows the dependence of vortex decay and secondary vortex occurrence on the specific rotor design.



**Figure 6.10.:** Influence of various blade designs on: a) Blade tip vortex trajectories, b) Primary blade tip vortex circulation  $\Gamma_v$ , c) Average blade tip vortex distance over the mean  $z$ -distance, d) Detected secondary structures

### 6.2.6. Influence of the Blade Passing Frequency

Up to this point, this chapter has shown various parameters with differing levels of influence on secondary structures, but no single dominant parameter has been identified that would allow a consistent comparison between cases with different numbers of blades. To address this, the blade passing frequency (BPF) was evaluated, and additional measurements were conducted to enable direct comparisons between one- and two-blade configurations at the same BPF.

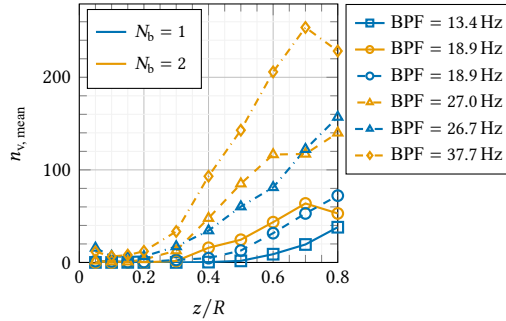


**Figure 6.11.:** Detected secondary structures for different blade passing frequencies

In these measurements, the blade loading was kept constant, while the rotation frequency varied. The one-bladed cases were tested at BPFs of 13.4 Hz, 18.9 Hz, and 26.7 Hz, and the two-bladed cases at 18.9 Hz, 27.0 Hz, and 37.7 Hz. This allows for a comparison of the one- and two-bladed configurations at overlapping BPF levels.

The upper limit of the BPF was constrained by mechanical restrictions of the test stand and by power limitations of the propulsion system. For completeness, results are also presented from the one-blade case at 13.37 Hz and the two-blade case at 37.7 Hz, even though no corresponding comparative data were available at these frequencies.

The results of the secondary vortex detection are shown in Fig. 6.11. One-bladed data are shown in blue, and two-bladed data in orange. The number of secondary vortices increases with an increasing BPF. The one- and two-bladed cases yield very similar values at the matching (or similar) BPF. As a trend, the two-bladed rotor produces slightly more secondary vortices. It is further noted that the BPF does not affect the vortex spacing, see Figs. 6.12a and 6.12b. For the one-bladed cases, the spacing remains constant over the tested BPF range. For the two-bladed cases, the trajectories split caused by the vortex pairing, but the variation with BPF produces only scatter and no systematic trend. In summary, the time constant between two successive blade passes is an independent and decisive parameter of secondary vortex formation.

Having established the strong influence of BPF on the occurrence of secondary vortices,

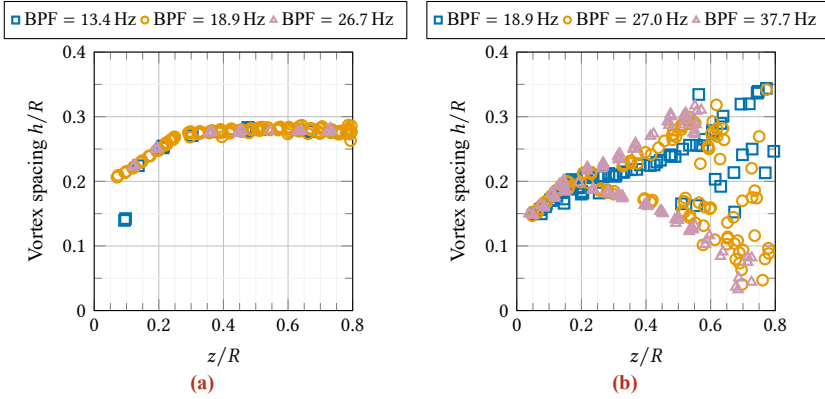


**Figure 6.12.:** Average blade tip vortex distance over the mean  $z$ -distance for different BPFs: a)  $N_b = 1$ , b)  $N_b = 2$

Fig. 6.13 now shows all measured secondary vortices (+) at a height of  $0.6 z/R$  as a function of the BPF. Within the observed range, an almost linear dependency of the BPF is shown. However, it is noticeable that the origin of this linear line does not pass through the origin, as no secondary vortices are detected at very low BPF. This offset is attributed to the measurement threshold: weak or small-scale vortices fall below the detection limit, resulting in very few detections for low-BPF or low-thrust cases.

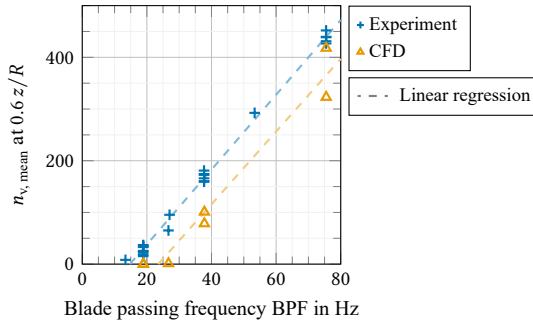


**Figure 6.13.:** Detected number of secondary vortices at  $0.6 z/R$  as a function of blade passing frequency for all investigated cases

When comparing the experimental findings with the available CFD data ( $\Delta$ ), also shown in Fig. 6.13, a very similar trend is observed. Although the simulations tend to predict slightly

fewer vortices, the slope of the increase is nearly identical. The slight shift toward larger BPF values is most likely due to the limited numerical resolution. As a result, strong velocity gradients are insufficiently resolved, which suppresses small-scale vortices and affects the vortex detection criterion. Additional inaccuracies may arise because the linear scaling of the vortex criteria with grid spacing is only a first order approximation and does not account for potential nonlinearities.

### 6.3. Validation of Evaluation Parameters

The final part of the discussion addresses the sensitivity of the secondary vortex measurements to the chosen evaluation parameters. To assess the robustness of the previous findings, the influence of three factors is examined: the rotor traverse heights at which the secondary vortices were extracted, the detection threshold, and the mean number of secondary vortices  $n_{v, \text{mean}}$  used as an evaluation parameter. This analysis demonstrates that the observed trends are not artifacts of parameter choice but reflect genuine physical behavior.

Figure 6.14 shows the average curves of the BPF for all cases at different distances from the rotor plane. At small distances the trend appears more exponential, whereas at larger distances ( $0.7 z/R$  and  $0.8 z/R$ ) and higher blade passing frequencies the number of secondary vortices falls below the curve extrapolated from smaller distances. This trend is caused by the onset of primary and secondary vortex decay, which begins earlier at higher BPF than at lower values. Nevertheless, the overall conclusion remains valid: the strong dependence of secondary vortices on the BPF is evident at all measured distances, given that primary vortex decay plays only a minor role.

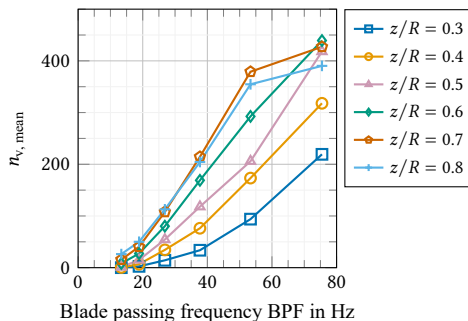


**Figure 6.14.:** Detected number of secondary vortices for several distances to the rotor plane as a function of the blade passing frequency

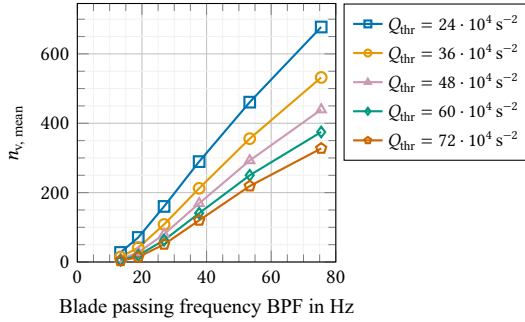


**Figure 6.15.:** Detected number of secondary vortices at  $0.6 z/R$  for different detection thresholds as a function of the blade passing frequency

In Chap. 4.2 it was argued that a detection threshold of  $Q_{\text{thr}} = 48 \cdot 10^4 \text{ s}^{-2}$  represents a reasonable compromise for evaluation purposes. To further assess its influence on the key results, a parameter variation was performed for each case, and the resulting number of secondary vortices at  $0.6 z/R$  as function of the BPF is shown in Fig. 6.15. As expected, lowering the threshold increases the number of secondary vortices detected in each case. This is consistent with the findings presented in Chap. 4.2. Figure 4.13b has shown for one sample, that lowering the threshold extends the result by only adding weaker vortices. However, the factor in between  $Q_{\text{thr}} = 72 \cdot 10^4 \text{ s}^{-2}$  and the other evaluations vary with the blade passing frequency, see Fig. 6.16. Cases with smaller BPF values are more sensitive to threshold variation, indicating that they contain smaller structures than those with higher blade passing

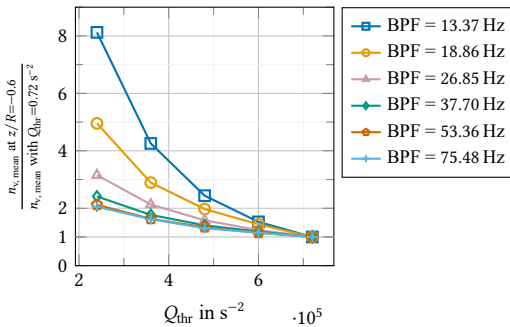


**Figure 6.16.:** Influence of the vortex detection threshold  $Q_{\text{thr}}$  on  $n_{v, \text{mean}}$  in relation to  $Q_{\text{thr}} = 72 \cdot 10^4 \text{ s}^{-2}$  for several blade passing frequencies at  $0.6 z/R$

frequencies.

Two explanations appear most plausible for this trend. First, the initial number of secondary vortices for small blade passing frequencies is quite small. As a consequence, almost all secondary vortices lie below the detection threshold. Second, with a limited resolution of a FOV there also is a limited number of separate secondary vortices that can be detected. A result of the threshold decrease is that several vortices may be detected as they are on a plateau with no decrease in  $Q$  in between. A physical vortex merging and an apparent merging due to the limited resolution cannot be separated.

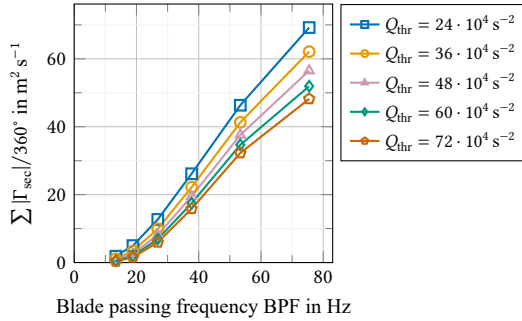


**Figure 6.17.:** Cumulative circulation of secondary vortices per revolution for different detection thresholds  $Q_{thr}$

The relevance of this discussion can be assessed by evaluating the cumulated circulation of secondary structures per revolution, presented in Fig. 6.17. This diagram is shown in dimensional form, since the circulation of secondary structures does not depend on blade loading and therefore cannot be non-dimensionalized with  $V_{tip} c$ . It should be noted that the circulation of secondary vortices also exhibits a strong dependency on the BPF. However, lowering the detection threshold primarily adds small vortices, so that the effect of the threshold on the total captured circulation is significantly weaker than on the total number of vortices.

To summarize, the dependency on BPF is consistent over a wide range of evaluation parameters and is the key finding of this chapter. The sensitivity analysis also confirmed that the post-processing settings, which had been tested *a priori* on sample results, remain appropriate. As a consequence, it was decided to keep the initial settings for the overall evaluation. Although, one may argue that the cumulative secondary vortex circulation may be the more meaningful parameter compared to the plain number of vortices, it is also difficult to interpret its meaning for streamwise vortices. Another argument for evaluating the number is the effort to keep the evaluation parameters as simple as possible.

## 7. Conclusions and Outlook

This thesis presents the methodology and results on experimental studies of a rotor in hover. For this purpose, the Hover Test Stand Göttingen (HVG) was developed. The setup enables the investigation of primary and secondary blade tip vortex decay for a wide range of parameters. By avoiding the geometric and aerodynamic complexities of a complete rotorcraft configuration, the simplified test stand provided controlled conditions well suited for creating a reference experimental database for the validation of numerical simulations. The built-in traverse system allowed for measurements of secondary vortices without requiring modifications of the PIV setup, thereby facilitating a unique parameter study covering more than 30 different configurations. It also allowed for the investigation of very old vortices (up to  $2000^\circ$ ), a regime for which experimental data are otherwise scarce.

*How accurately do existing vortex models reproduce the measured blade tip vortices?*

For four selected cases, a highly resolved study of primary blade tip vortices was conducted. The results were used to benchmark several vortex models from literature. It was found that the circulation at larger vortex radii deviated from the prediction by most vortex models. For this reason, the Lamb-Oseen vortex model was adapted by using the vortex circulation at  $1.91 r_c$  as input circulation for the model. This value represents the radial position where the Lamb-Oseen model reaches 99% of its predicted circulation. With this minor modification, the Lamb-Oseen model predicted the maximum tangential velocity with good accuracy. However, for tangential velocities at larger vortex radii the previous described discrepancy remained. Interestingly, the agreement at larger radii was best when the circulation induced by the wake shear layer was subtracted from the flow field. In these cases, the circulation first converged for higher radii, aligning well with the Lamb-Oseen model. Beyond this region, a slight decrease was observed, which accounts for the finite expansion of a vortex within a helical vortex system. At the latest by  $h/2$ , the vortex circulation is expected to approach zero. As a result, the Lamb-Oseen model only serves as a good prediction for small vortex radii, up to about  $4r/r_c$ , since its derivation assumes a vortex embedded in an infinite domain.

The vortex core radii were also represented reasonably well by a slightly modified Lamb-Oseen model that accounts for an initial vortex core size. However, this approach could not reproduce the observed decrease in core size for older vortices. Improved agreement was obtained with the Ananthan vortex core model, when vortex stretching and compression were incorporated under reasonable assumptions. These findings indicate that vortex

stretching/compression must be considered, as their influence is potentially significant.

*Which influencing factors govern the occurrence of secondary vortices, and how do secondary vortices contribute to vortex breakdown and interactions?*

An extensive simultaneous study of primary and secondary blade tip vortices was conducted for over 30 different configurations. For selected cases, the experimental data were compared with high-fidelity numerical results. Most notably, both CFD and experiment revealed a strong, nearly linear dependence on blade passing frequency (BPF). Although the CFD simulations slightly underpredicted the magnitude of secondary vortices, the experimental trends were reproduced.

Other parameter variations also affected vortex decay and interaction. The rectangular blade tip exhibited a significantly reduced vortex pairing. However, the number of secondary structures remained constant, even though their azimuthal distribution changed, reflecting their tendency to form around the primary blade tip vortices

Changes in blade loading and vortex spacing also influenced the secondary vortices. A reduction in blade loading tended to increase their occurrence. Moreover, the median absolute circulation of the secondary vortices showed a slight increase with the blade loading, supporting the argument that the primary and secondary blade tip vortices are largely independent.

Blade geometry further affected vortex decay. The twisted blade showed a stronger contraction due to its more uniform lift distribution on the blade. The lower convection velocity of the vortices, however, led to earlier decay at smaller axial distances from the rotor. The complete decay of primary vortices also inhibited the subsequent formation of additional secondary vortices below  $0.6 z/R$ .

In contrast, the blade-to-blade pitch offset did not significantly affect the secondary vortices or the overall vortex decay. This finding was unexpected, as Bodling et al. (2024) reported numerical studies predicting a measurable influence. A plausible explanation is that the influence of geometric imperfections in a perfectly defined CFD model cannot be directly compared with the introduction of pitch trim imperfections on a real-world model.

## Outlook

This thesis has expanded the experimental database of hover measurements of rotor wakes, particularly with respect to blade tip vortices at high vortex ages and secondary vortices. The new measurements of primary blade tip vortices highlight additional challenges for vortex modelling. Current vortex models were not able to capture tangential velocity distributions with sufficient accuracy, which motivated the development of slightly adapted models. However, the variation in vortex Reynolds number in the present experiments was too small to draw final

---

conclusions regarding its influence on the tangential velocity. Addressing this question would be an important step towards understanding to which extent model-scale measurements can be reliably compared with full-scale helicopter data. A follow-up project is planned to close this gap by employing a rotor in the High Pressure Wind Tunnel Göttingen (HDG). Pressurization of the test environment allows the vortex Reynolds number to be increased by up to two orders of magnitude. This enables vortex characterization of the same rotor at model scale and full-scale vortex Reynolds numbers and though the systematic investigation of its influence.

In addition to the tangential velocity, the proposed approach of incorporating long-wave instabilities into the Ananthan-Leishman vortex model requires further validation. This requires a combination of high-resolution velocity field measurements with simultaneously accurate three-dimensional tracking of the blade tip vortex trajectory.

The understanding of the factors, contributing to the formation of secondary vortices has been advanced through this thesis. Nevertheless, the precise mechanisms governing the formation process remain unclear. The fact that the CFD simulations reproduced the trends observed in the experiments, suggests that the formation process observed in CFD is physically meaningful. A major advantage of the CFD is the availability of all flow parameters throughout the entire flow field, enabling more detailed investigations, e.g., the analysis of mass and momentum exchange between the flow field and secondary vortices.

An experimental approach to gain further insight into the development of secondary vortices would be to reduce complexity, e.g., by experimentally validating DNS simulations, which also predict the occurrence of secondary vortices between co-rotating vortex pairs. Such studies could also help address the broader question of how vortices exchange vorticity and, in the best case, contribute to the development of a general theory explaining streamwise vortices.

# **Appendix**

## A. PIV Parameter Study

**Table A.1.:** Overview of PIV processing parameters used in the evaluation of velocity fields.

Initial window size (px)	Final window size (px)	Overlap (%)	Final window shape	Initial passes	Final passes
64	16	75	adaptive	1	5
64	16	75	adaptive	3	1
64	16	75	adaptive	3	3
64	16	75	adaptive	3	7
64	16	75	adaptive	3	9
64	16	75	adaptive	3	11
64	16	75	adaptive	5	5
64	16	75	adaptive	7	5
64	16	75	adaptive	9	5
64	16	75	adaptive	11	5
64	8	75	adaptive	3	5
64	8	50	adaptive	3	5
64	12	50	adaptive	3	5
64	12	75	adaptive	3	5
64	12	87	adaptive	3	5
64	16	50	adaptive	3	5
64	16	87	adaptive	3	5
64	16	75	square	3	5
64	16	75	round	3	5
64	16	75	adaptive	3	5
48	16	75	adaptive	5	5
96	16	75	adaptive	5	5
128	16	75	adaptive	5	5
128	16	75	adaptive	3	5
256	16	75	adaptive	5	5
64	24	50	adaptive	3	5
64	24	87	adaptive	3	5
64	24	75	adaptive	3	5

*A. PIV Parameter Study*

---

Initial window size (px)	Final window size (px)	Overlap (%)	Final window shape	Initial passes	Final passes
64	32	75	adaptive	3	5
64	64	75	adaptive	3	5

# References

- Abraham, A., Castillo-Castellanos, A., and Leweke, T. (2023), Simplified Model for Helical Vortex Dynamics in the Wake of an Asymmetric Rotor, *Flow*, Vol. 3, E5, DOI: 10.1017/flow.2022.33.
- Abras, J., Hariharan, N. S., and Narducci, R. P. (2019), Wake Breakdown of High-fidelity Simulations of a Rotor in Hover, AIAA Scitech 2019 Forum, San Diego, CA, USA, DOI: 10.2514/6.2019-0593.
- Ahlborn, Fr. (1902), Über den Mechanismus des Hydrodynamischen Widerstandes, *Abhandlungen aus dem Gebiete der Naturwissenschaften*, Vol. 17, No. 1, pp. 1–59.
- Ananthan, S. and Leishman, J. G. (2004), Role of Filament Strain in the Free-Vortex Modeling of Rotor Wakes, *Journal of the American Helicopter Society*, Vol. 49, No. 2, pp. 176–191, DOI: 10.4050/jahs.49.176.
- Anderson, J. D. (2017), Fundamentals of Aerodynamics, Sixth edition, McGraw-Hill Series in Aeronautical and Aerospace Engineering, McGraw-Hill Education: New York, NY, USA.
- Barkley, D. and Henderson, R. D. (1996), Three-Dimensional Floquet Stability Analysis of the Wake of a Circular Cylinder, *Journal of Fluid Mechanics*, Vol. 322, pp. 215–241, DOI: 10.1017/S0022112096002777.
- Bartzsch, H. T., Wolf, C. C., Galli, E., Raffel, M., Braune, M., and Löhr, M. (2025), BOS and HWA Measurements on Rotor Tip Vortices in a High Pressure Wind Tunnel, Vertical Flight Society's 81st Annual Forum & Technology Display, Virginia Beach, VA, USA.
- Bauknecht, A., Ewers, B., Schneider, O., and Raffel, M. (2015), Aerodynamic Results from the STAR Hover Test: An Examination of Active Twist Actuation, European Rotorcraft Forum, Munich, Germany.
- Bauknecht, A. (2016), Characterization of Blade Tip Vortices on Large-Scale Rotors, PhD thesis, Gottfried Wilhelm Leibniz Universität Hannover.
- Bauknecht, A., Ewers, B., Wolf, C. C., Raffel, M., and Leopold, F. (2014), Three-Dimensional Reconstruction of Blade Tip Vortices of a BO 105 Using a Multi-Camera BOS System, American Helicopter Society 70th Annual Forum, Montreal, Canada, pp. 1–12.
- Bell, J. H. and Mehta, R. D. (1992), Measurements of the Streamwise Vortical Structures in a Plane Mixing Layer, *Journal of Fluid Mechanics*, Vol. 239, p. 213, DOI: 10.1017/S0022112092004385.
- Bernal, L. P. and Roshko, A. (1986), Streamwise Vortex Structure in Plane Mixing Layers, *Journal of Fluid Mechanics*, Vol. 170, pp. 499–525, DOI: 10.1017/S002211208600099X.
- Betz, A. and Prandtl, L. (1919), Schraubenpropeller mit geringstem Energieverlust, *Nachrichten von der Gesellschaft der Wissenschaften zu Göttingen, Mathematisch-Physikalische Klasse*, Vol. 1919, No. 1, pp. 193–217.

- Bhagwat, M. J. and Leishman, J. G. (2002), Generalized Viscous Vortex Model for Application to Free-Vortex Wake and Aeroacoustic Calculations, 58th Annual Forum and Technology Display of the American Helicopter Society, Montreal, Canada.
- Birch, D. M., Lee, T., Mokhtarian, F., and Kafyeke, F. (2003), Rollup and Near-Field Behavior of a Tip Vortex, *Journal of Aircraft*, Vol. 40, No. 3, pp. 603–607, DOI: 10.2514/2.3137.
- Birch, D. M. and Martin, N. (2013), Tracer Particle Momentum Effects in Vortex Flows, *Journal of Fluid Mechanics*, Vol. 723, pp. 665–691, DOI: 10.1017/jfm.2013.82.
- Blanco-Rodríguez, F. J. and Le Dizès, S. (2016), Elliptic Instability of a Curved Batchelor vortex, *Journal of Fluid Mechanics*, Vol. 804, pp. 224–247, DOI: 10.1017/jfm.2016.533.
- Bodling, A. and Potsdam, M. (2022), Numerical Investigation of Secondary Vortex Structures in a Rotor Wake, *Journal of the American Helicopter Society*, Vol. 67, No. 4, pp. 1–18, DOI: 10.4050/JAHS.67.042007.
- Bodling, A., Schwarz, C., Wolf, C. C., and Gardner, A. D. (2023), Numerical and Experimental Assessment of Parameters Influencing the Development of Secondary Vortex Structures in Rotor Wakes, Vertical Flight Society's 79th Annual Forum & Technology Display, West Palm Beach, FL, USA, pp. 1–17, DOI: 10.4050/F-0079-2023-17995.
- Bodling, A., Schwarz, C., Wolf, C. C., and Gardner, A. D. (2024), Enhancing Numerical Accuracy in the Prediction of Rotor Wake Vortex Structures, *Physics of Fluids*, Vol. 36, No. 3, p. 037137, DOI: 10.1063/5.0196010.
- Braukmann, J. N. (2021), Combination of Simultaneous Density and Velocity Measurements of Blade Tip Vortices under Cyclic Pitch Conditions, PhD thesis, Leibniz-Universität Hannover.
- Braukmann, J. N., Schwarz, C., Wolf, C., Buron, E., Koch, S., Buske, G., and Gardner, A. (2023), BOS and Hot-Film Analysis of a CH-53G Helicopter Wake in Ground Effect, Vertical Flight Society's 79th Annual Forum & Technology Display, West Palm Beach, FL, USA, pp. 1–15, DOI: 10.4050/F-0079-2023-18181.
- Breitsamter, C. (2011), Wake vortex characteristics of transport aircraft, *Progress in Aerospace Sciences*, Vol. 47, No. 2, pp. 89–134, DOI: 10.1016/j.paerosci.2010.09.002.
- Canivete Cuissa, J. R. and Steiner, O. (2020), Vortices Evolution in the Solar Atmosphere: A Dynamical Equation for the Swirling Strength, *Astronomy & Astrophysics*, Vol. 639, DOI: 10.1051/0004-6361/202038060.
- Caradonna, F. (1999), Performance Measurement and Wake Characteristics of a Model Rotor in Axial Flight, *Journal of the American Helicopter Society*, Vol. 44, No. 2, pp. 101–108, DOI: 10.4050/JAHS.44.101.
- Cerretelli, C. and Williamson, C. H. K. (2003), A New Family of Uniform Vortices Related to Vortex Configurations before Merging, *Journal of Fluid Mechanics*, Vol. 493, pp. 219–229, DOI: 10.1017/S0022112003005536.
- Chaderjian, N. M. and Buning, P. G. (2011), High Resolution Navier-Stokes Simulation of Rotor Wakes, American Helicopter Society 67th Annual Forum, Virginia Beach, VA, USA, pp. 1–18.
- Chen, Q., Zhong, Q., Qi, M., and Wang, X. (2015), Comparison of Vortex Identification Criteria for Planar Velocity Fields in Wall Turbulence, *Physics of Fluids*, Vol. 27, No. 8, p. 085101, DOI: 10.1063/1.4927647.

- 
- Comte, P., Silvestrini, J., and Bégou, P. (1998), Streamwise Vortices in Large-Eddy Simulations of Mixing Layers, *European Journal of Mechanics - B/Fluids*, Vol. 17, No. 4, pp. 615–637, doi: 10.1016/S0997-7546(98)80016-2.
- Crow, S. C. and Bate, E. R. (1976), Lifespan of Trailing Vortices in a Turbulent Atmosphere, *Journal of Aircraft*, Vol. 13, No. 7, pp. 476–482, doi: 10.2514/3.44537.
- Domogalla, V. (2021), Quantification of the Influence of Particle Voids on PIV Measurements via Synthetic-PIV, *New Results in Numerical and Experimental Fluid Mechanics XIII*, Vol. 151, ed. by A. Dillmann, G. Heller, E. Krämer, and C. Wagner, Vol. 151, Springer International Publishing: Cham, pp. 325–334, doi: 10.1007/978-3-030-79561-0\_31.
- Egolf, T. A., Hariharan, N. S., Narducci, R. P., and Reed, E. (2017), AIAA Standardized Hover Simulation: Hover Performance Prediction Status and Outstanding Issues, 55th AIAA Aerospace Sciences Meeting, Grapevine, TX, USA, pp. 1–17, doi: 10.2514/6.2017-1429.
- Freed, A. Y., Won, J., and Lee, S. (2025), Effect of Wingtip Side Edge Shape on Vortex Formation and Aerodynamics Using High-Fidelity Numerical Simulations, AIAA Aviation Forum and Ascend 2025, Las Vegas, NV, USA, doi: 10.2514/6.2025-3702.
- Gajo, F., Heintz, A., and Kessler, M. (2025), A Comparison of Numerical and Experimental Data from Wake Decay in Hovering Rotors, doi: 10.21203/rs.3.rs-7187651/v1, pre-published.
- Gajo, F. and Keßler, M. (2024), Challenges About Detecting and Analysing the Rotor Blade Tip Vortices in Numerical Simulations at Late Wake Ages, 50th European Rotorcraft Forum, Marseille, France.
- Gaydon, M., Raffel, M., Willert, C., Rosengarten, M., and Kompenhans, J. (1997), Hybrid Stereoscopic Particle Image Velocimetry, *Experiments in Fluids*, Vol. 23, No. 4, pp. 331–334, doi: 10.1007/s003480050118.
- Ghimire, H. C. and Bailey, S. C. C. (2017), An Experimental Investigation of Wing-Tip Vortex Decay in Turbulence, *Physics of Fluids*, Vol. 29, No. 3, p. 037108, doi: 10.1063/1.4979133.
- Gibeau, B., Koch, C. R., and Ghaemi, S. (2018), Secondary Instabilities in the Wake of an Elongated Two-Dimensional Body with a Blunt Trailing Edge, *Journal of Fluid Mechanics*, Vol. 846, pp. 578–604, doi: 10.1017/jfm.2018.285.
- Giuni, M. and Green, R. B. (2013), Vortex Formation on Squared and Rounded Tip, *Aerospace Science and Technology*, Vol. 29, No. 1, pp. 191–199, doi: 10.1016/j.ast.2013.03.004.
- Goertler, A. T. (2020), Numerical Investigations of the Blade-Tip Vortex of a Rotor with Axial Inflow, PhD thesis, Leibniz Universität Hannover.
- Green, S. I., ed. (1995), Fluid Vortices, red. by R. Moreau, Vol. 30, Fluid Mechanics and Its Applications, Springer Netherlands: Dordrecht, doi: 10.1007/978-94-011-0249-0.
- Günther, T. and Theisel, H. (2018), The State of the Art in Vortex Extraction, *Computer Graphics Forum*, Vol. 37, No. 6, pp. 149–173, doi: 10.1111/cgf.13319.
- Gupta, B. P. and Loewy, R. G. (1974), Theoretical Analysis of the Aerodynamic Stability of Multiple, Interdigitated Helical Vortices, *AIAA Journal*, Vol. 12, No. 10, pp. 1381–1387, doi: 10.2514/3.49493.
- Haimes, R. and Kenwright, D. (1999), On the Velocity Gradient Tensor and Fluid Feature Extraction, 14th Computational Fluid Dynamics Conference, Norfolk, VA, USA, doi: 10.2514/6.1999-3288.

- Haller, G. (2005), An Objective Definition of a Vortex, *Journal of Fluid Mechanics*, Vol. 525, pp. 1–26, doi: 10.1017/S0022112004002526.
- Hariharan, N. S., Egolf, T. A., and Sankar, L. N. (2014), Simulation of Rotor in Hover: Current State, Challenges and Standardized Evaluation, 52nd Aerospace Sciences Meeting, National Harbor, MD, USA, doi: 10.2514/6.2014-0041.
- Heineck, J. T., Yamauchi, G. K., Wadcock, A. J., Lourenco, L. M., and Abrego, A. (2000), Application of Three-Component PIV to a Hovering Rotor Wake, American Helicopter Society 56th Annual Forum, Fairfax, VA, USA, pp. 375–390.
- Heintz, A., Schwarz, C., Wolf, C. C., and Raffel, M. (2023), Analysis of Configurational Parameters on the Vortex System of a Rotor, 21. STAB - Workshop 2023, Göttingen, Germany, pp. 50–51.
- Heintz, A., Schwarz, C., Wolf, C. C., and Raffel, M. (2025), Configurational Influence on a Vortex System of a Hovering Rotor, *AIAA Journal*, Vol. 63, No. 6, pp. 2412–2427, doi: 10.2514/1.J064640.
- Helmholtz, H. (1858), Über Integrale der hydrodynamischen Gleichungen, welche den Wirbelbewegungen entsprechen. *Journal für die reine und angewandte Mathematik*, Vol. 1858, No. 55, pp. 25–55, doi: 10.1515/crll.1858.55.25.
- Holzäpfel, F. (2005), Aircraft Wake Vortex Evolution and Prediction, Habilitation, TU München.
- Holzäpfel, F., Misaka, T., and Hennemann, I. (2010), Wake-Vortex Topology, Circulation, and Turbulent Exchange Processes, AIAA Atmospheric and Space Environments Conference, Toronto, Canada, doi: 10.2514/6.2010-7992.
- Hunt, J. C. R., Wray, A. A., and Moin, P. (1988), Eddies, Streams, and Convergence Zones in Turbulent Flows, in: *Proceedings of the Summer Program 1988*.
- Jain, R. (2018), Sensitivity Study of High-Fidelity Hover Predictions on the Sikorsky S-76 Rotor, *Journal of Aircraft*, Vol. 55, No. 1, pp. 78–88, doi: 10.2514/1.C034076.
- Jeong, J. and Hussain, F. (1995), On the Identification of a Vortex, *Journal of Fluid Mechanics*, Vol. 285, pp. 69–94, doi: 10.1017/S0022112095000462.
- Kähler, C., Sammler, B., and Kompenhans, J. (2002), Generation and Control of Tracer Particles for Optical Flow Investigations in Air, *Experiments in Fluids*, Vol. 33, No. 6, pp. 736–742, doi: 10.1007/s00348-002-0492-x.
- Kaufmann, W. (1962), Über die Ausbreitung kreiszylindrischer Wirbel in zähen (viskosen) Flüssigkeiten, *Ingenieur-Archiv*, Vol. 31, No. 1, pp. 1–9, doi: 10.1007/BF00538235.
- Keane, R. D. and Adrian, R. J. (1992), Theory of Cross-Correlation Analysis of PIV Images, *Applied Scientific Research*, Vol. 49, No. 3, pp. 191–215, doi: 10.1007/BF00384623.
- Kindler, K., Mulleners, K., Richard, H., and Raffel, M. (2009), A Full-Scale Particle Image Velocimetry Investigation of “Young” Rotor Blade Tip Vortices, American Helicopter Society 65th Annual Forum, Fairfax, VA, USA.
- Kocurek, J. D. and Tangler, J. L. (1977), A Prescribed Wake Lifting Surface Hover Performance Analysis, *Journal of the American Helicopter Society*, Vol. 22, No. 1, pp. 24–35, doi: 10.4050/JAHS.22.24.
- Kuenn, A. D. and Kliment, L. K. (2021), A Brief Survey of Vortex Models, AIAA Scitech 2021 Forum, Virtual Event, doi: 10.2514/6.2021-1328.
- Lamb (1932), *Hydrodynamics*, Vol. 6, Cambridge University Press: Cambridge.

- 
- Landgrebe, A. J. (1971), An Analytical and Experimental Investigation of Helicopter Rotor Hover Performance and Wake Geometry Characteristics, Fort Belvoir, VA: Defense Technical Information Center, DOI: 10.21236/AD0728835.
- LaVision (2023), Product Manual for DaVis 11.0, Manual, LaVision: Göttingen.
- Lazar, E., DeBlauw, B., Glumac, N., Dutton, C., and Elliott, G. (2010), A Practical Approach to PIV Uncertainty Analysis, 27th AIAA Aerodynamic Measurement Technology and Ground Testing Conference, Chicago, IL, USA, DOI: 10.2514/6.2010-4355.
- Leishman, J. G. (2002), Principles of Helicopter Aerodynamics, Cambridge Aerospace Series No. 12, Cambridge University Press: Cambridge.
- Leweke, T., Meunier, P., Laporte, F., and Darracq, D. (2001), Controlled Interaction of Co-Rotating Vortices, 3rd ONERA-DLR Aerospace Symposium (ODAS 2001), Paris, France.
- Leweke, T., Quaranta, H. U., Bolnot, H., Blanco-Rodríguez, F. J., and Dizès, S. L. (2014), Long- and Short-Wave Instabilities in Helical Vortices, *Journal of Physics: Conference Series*, Vol. 524, p. 012154, DOI: 10.1088/1742-6596/524/1/012154.
- Leweke, T., Le Dizès, S., and Williamson, C. H. (2016), Dynamics and Instabilities of Vortex Pairs, *Annual Review of Fluid Mechanics*, Vol. 48, No. 1, pp. 507–541, DOI: 10.1146/annurev-fluid-122414-034558.
- Luckring, J. (2019), The Discovery and Prediction of Vortex Flow Aerodynamics, *The Aeronautical Journal*, Vol. 123, No. 1264, pp. 729–804, DOI: 10.1017/aer.2019.43.
- Lugt, H. J. (1996), Introduction to Vortex Theory, Vortex Flow Press.
- Mach, L. (1896), Über die Sichtbarmachung von Luftstromlinien, *Zeitschrift für Luftschiffahrt und Physik der Atmosphäre*, Vol. 15, No. 6, pp. 129–139.
- Martin, P. B. and Leishman, J. G. (2002), Trailing Vortex Measurements in the Wake of a Hovering Rotor Blade with Various Tip Shapes, 58th Annual Forum of the American Helicopter Society, Montreal, Canada.
- Martin, P. B. (2001), Measurements of the Trailing Vortex Formation, Structure, and Evolution in the Wake of a Hovering Rotor, PhD thesis, University of Maryland, College Park.
- McAlister, K. W. (2004), Rotor Wake Development During the First Revolution, *Journal of the American Helicopter Society*, Vol. 49, No. 4, pp. 371–390, DOI: 10.4050/JAHS.49.371.
- Melander, M. V., Zabusky, N. J., and McWilliams, J. C. (1988), Symmetric Vortex Merger in two Dimensions: Causes and Conditions, *Journal of Fluid Mechanics*, Vol. 195, p. 303, DOI: 10.1017/S0022112088002435.
- Meunier, P. and Leweke, T. (2005), Elliptic Instability of a Co-Rotating Vortex Pair, *Journal of Fluid Mechanics*, Vol. 533, DOI: 10.1017/S0022112005004325.
- Mie, G. (1908), Beiträge zur Optik trüber Medien, speziell kolloidaler Metallösungen, *Annalen der Physik*, Vol. 330, No. 3, pp. 377–445, DOI: 10.1002/andp.19083300302.
- Moore, D. W. and Saffman, P. G. (1971), Structure of a Line Vortex in an Imposed Strain, in: *Aircraft Wake Turbulence and Its Detection*, ed. by J. H. Olsen, A. Goldberg, and M. Rogers, Springer US: Boston, MA, USA, pp. 339–354.
- Mula, S. M., Stephenson, J. H., Tinney, C. E., and Sirohi, J. (2013), Dynamical Characteristics of the Tip Vortex from a Four-Bladed Rotor in Hover, *Experiments in Fluids*, Vol. 54, No. 10, p. 1600, DOI: 10.1007/s00348-013-1600-9.
- Neef, M. R. (2025), High-Resolution Parameter Study of Blade Tip Vortices of a Rotor in Hover, Bachelor Thesis, Georg-August Universität Göttingen.

- Norman, T. R. et al. (2023), Fundamental Test of a Hovering Rotor: Comprehensive Measurements for CFD Validation, Vertical Flight Society's 79th Annual Forum & Technology Display, West Palm Beach, FL, USA, pp. 1–27, DOI: 10.4050/F-0079-2023-17983.
- Nybelen, L. and Paoli, R. (2009), Direct and Large-Eddy Simulations of Merging in Corotating Vortex System, *AIAA Journal*, Vol. 47, No. 1, pp. 157–167, DOI: 10.2514/1.38026.
- Öhrle, C., Schäferlein, U., Keßler, M., and Krämer, E. (2018), Higher-Order Simulations of a Compound Helicopter Using Adaptive Mesh Refinement, American Helicopter Society 74th Annual Forum, Phoenix, AZ, USA, pp. 1–19.
- Oseen, C. W. (1912), Über die Wirbelbewegung in einer reibenden Flüssigkeit, *Arkiv för Matematik, Astronomi och Fysik*, Vol. 7.
- Parthasarathy, S., Cho, Y., and Back, L. (1985), Wide-Field Shadowgraph Flow Visualization of Tip Vortices Generated by a Helicopter Rotor, 18th Fluid Dynamics and Plasmadynamics and Lasers Conference, Cincinnati, OH, USA, DOI: 10.2514/6.1985-1557.
- Potsdam, M. and Jayaraman, B. (2014), UH-60A Rotor Tip Vortex Prediction and Comparison to Full-Scale Wind Tunnel Measurements, American Helicopter Society 70th Annual Forum, Montreal, Canada, pp. 1–21.
- Prandtl, L. (1919), Tragflügeltheorie. II. Mitteilung, *Nachrichten von der Gesellschaft der Wissenschaften zu Göttingen, Mathematisch-Physikalische Klasse*, Vol. 1919, pp. 107–137.
- Quaranta, H. U., Bolnot, H., and Leweke, T. (2015), Long-Wave Instability of a Helical Vortex, *Journal of Fluid Mechanics*, Vol. 780, pp. 687–716, DOI: 10.1017/jfm.2015.479.
- Raffel, M., Richard, H., Agocs, J., Otter, D., Mattner, H., and Göhmann, U. (2001), Experimental Aspects of PIV Applied to a Bo 105 Helicopter in Hover-Flight Condition, 4th International Symposium on Particle Image Velocimetry, Göttingen, Germany.
- Raffel, M., Richard, H., and Meier, G. E. A. (2000), On the Applicability of Background Oriented Optical Tomography for Large Scale Aerodynamic Investigations, *Experiments in Fluids*, Vol. 28, No. 5, pp. 477–481, DOI: 10.1007/s003480050408.
- Raffel, M., Seelhorst, U., Willert, C., Vollmers, H., Bütetfisch, K. A., and Kompenhans, J. (1996), Measurement of Vortical Structures on a Helicopter Rotor Model in a Wind Tunnel by LDV and PIV, 8th International Symposium on Applications of Laser Techniques to Fluid Mechanics, Lisbon, Portugal.
- Raffel, M. and Kompenhans, J. (1993), PIV Measurements of Unsteady Transonic Flow Fields Above a NACA 0012 Airfoil, in: *Fifth International Conference on Laser Anemometry: Advances and Applications*, SPIE: Veldhoven, Netherlands, pp. 527–534.
- Raffel, M., Willert, C. E., Scarano, F., Kähler, C. J., Wereley, S. T., and Kompenhans, J. (2018), Particle Image Velocimetry: A Practical Guide, Springer International Publishing: Cham, DOI: 10.1007/978-3-319-68852-7.
- Ramasamy, M., Heineck, J., Yamauchi, C., Schairer, E., and Norman, T. (2024), Comprehensive Aerodynamic Analysis of PIV Measurements in the NFAC 80- by 120-ft Test Section Towards Understanding HVAB Hovering Rotor Characteristics, Vertical Flight Society's 80th Annual Forum & Technology Display, Montreal, Canada, pp. 1–30, DOI: 10.4050/F-0080-2024-1351.
- Ramasamy, M., Johnson, B., and Leishman, J. G. (2009), Turbulent Tip Vortex Measurements Using Dual-Plane Stereoscopic Particle Image Velocimetry, *AIAA Journal*, Vol. 47, No. 8, pp. 1826–1840, DOI: 10.2514/1.39202.

- 
- Ramasamy, M. and Leishman, J. G. (2006), A Generalized Model for Transitional Blade Tip Vortices, *Journal of the American Helicopter Society*, Vol. 51, No. 1, p. 92, DOI: 10.4050/1.3092881.
- Ramasamy, M. and Leishman, J. G. (2007), A Reynolds Number-Based Blade Tip Vortex Model, *Journal of the American Helicopter Society*, Vol. 52, No. 3, pp. 214–223, DOI: 10.4050/JAHS.52.214.
- Rankine, W. J. M. (1858), *A Manual of Applied Mechanics*, Charles Griffin and Co.: London.
- Reynolds, O. (1883), An Experimental Investigation of the Circumstances Which Determine Whether the Motion of Water Shall Be Direct or Sinuous, and of the Law of Resistance in Parallel Channels, *Philosophical Transactions of the Royal Society of London*, Vol. 174, No. 174, pp. 935–982, DOI: 10.1098/rstl.1883.0029.
- Richard, H., Henning, A., Raffel, M., Willert, C., and Van Der Wall, B. (2006), 2C and 3C PIV Measurements on a Rotor, 13th International Symposium on Applications of Laser Techniques to Fluid Mechanics, Lisbon, Portugal.
- Robinson, S. K. (1990), A Review of Vortex Structures and Associated Coherent Motions in Turbulent Boundary Layers, *Structure of Turbulence and Drag Reduction*, ed. by A. Gyr, Springer Berlin Heidelberg: Berlin, Heidelberg, pp. 23–50, DOI: 10.1007/978-3-642-50971-1\_2.
- Saripalli, K. (1995), Application of Particle Imaging Velocimetry Techniques to Helicopter Rotor Flowfields at McDonnell Douglas Aerospace, 33rd Aerospace Sciences Meeting and Exhibit, Reno, NV, USA, DOI: 10.2514/6.1995-17.
- Scarano, F. and Poelma, C. (2009), Three-Dimensional Vorticity Patterns of Cylinder Wakes, *Experiments in Fluids*, Vol. 47, No. 1, p. 69, DOI: 10.1007/s00348-009-0629-2.
- Schanz, D., Gesemann, S., and Schröder, A. (2016), Shake-The-Box: Lagrangian Particle Tracking at High Particle Image Densities, *Experiments in Fluids*, Vol. 57, No. 5, p. 70, DOI: 10.1007/s00348-016-2157-1.
- Scheimpflug, T. (1904), Improved Method and Apparatus for the Systematic Alteration or Distortion of Plane Pictures and Images by Means of Lenses and Mirrors for Photography and for Other Purposes, pat. 1196 (GB).
- Schlichting, H. and Truckenbrodt, E. (2013), *Grundlagen aus der Strömungstechnik: Aerodynamik des Tragflügels (Teil I)*, 3., Aufl. 2001 [Neuausg.], Aerodynamik des Flugzeuges, Springer Berlin: Berlin.
- Schram, C., Rambaud, P., and Riethmuller, M. L. (2004), Wavelet Based Eddy Structure Eduction from a Backward Facing Step Flow Investigated Using Particle Image Velocimetry, *Experiments in Fluids*, Vol. 36, No. 2, pp. 233–245, DOI: 10.1007/s00348-003-0695-9.
- Schröder, D., Leweke, T., and Stumpf, E. (2023), High-Speed Volumetric Particle Tracking Measurements of Unstable Helical Vortex Pairs, *Experiments in Fluids*, Vol. 64, No. 8, p. 141, DOI: 10.1007/s00348-023-03679-8.
- Schwarz, C. (2020), *Experimental Wake Characterization of Free-Flying Helicopters in Ground Effect*, PhD thesis, Gottfried Wilhelm Leibniz Universität Hannover.
- Schwarz, C., Bodling, A., Wolf, C. C., Brinkema, R., Potsdam, M., and Gardner, A. D. (2022), Development of Secondary Vortex Structures in Rotor Wakes, *Experiments in Fluids*, Vol. 63, No. 1, DOI: 10.1007/s00348-021-03348-8.

- Scully, M. and Sullivan, J. P. (1972), Helicopter Rotor Wake Geometry and Airloads and Development of Laser Doppler Velocimeter for Use in Helicopter Rotor Wakes, Technical Report No. 179, MIT Aerophysics Laboratory.
- Serrano-Aguilera, J. J., García-Ortiz, J. H., Gallardo-Claros, A., Parras, L., and Del Pino, C. (2016), Experimental Characterization of Wingtip Vortices in the Near Field Using Smoke Flow Visualizations, *Experiments in Fluids*, Vol. 57, No. 8, p. 137, DOI: 10.1007/s00348-016-2222-9.
- Soloff, S. M., Adrian, R. J., and Liu, Z.-C. (1997), Distortion Compensation for Generalized Stereoscopic Particle Image Velocimetry, *Measurement Science and Technology*, Vol. 8, No. 12, pp. 1441–1454, DOI: 10.1088/0957-0233/8/12/008.
- Soria, J. (1996), An Investigation of the Near Wake of a Circular Cylinder Using a Video-Based Digital Cross-Correlation Particle Image Velocimetry Technique, *Experimental Thermal and Fluid Science*, Vol. 12, No. 2, pp. 221–233, DOI: 10.1016/0894-1777(95)00086-0.
- Squire, H. B. (1965), The Growth of a Vortex in Turbulent Flow, *Aeronautical Quarterly*, Vol. 16, No. 3, pp. 302–306, DOI: 10.1017/s0001925900003516.
- Stack, J., Caradonna, F. X., and Savas, O. (2005), Flow Visualizations and Extended Thrust Time Histories of Rotor Vortex Wakes in Descent, *Journal of the American Helicopter Society*, Vol. 50, No. 3, p. 279, DOI: 10.4050/1.3092864.
- Tangler, J. L., Wohlfeld, R. M., and Miley, S. J. (1973), An Experimental Investigation of Vortex Stability, Tip Shapes, Compressibility, and Noise for Hovering Model Rotors, NASA Contractor Report, Washington, DC: National Aeronautics and Space Administration.
- Taylor, G. I. (1938), The Spectrum of Turbulence, *Proceedings of the Royal Society of London. Series A - Mathematical and Physical Sciences*, Vol. 164, No. 919, pp. 476–490, DOI: 10.1098/rspa.1938.0032.
- Thompson, M., Leweke, T., and Williamson, C. (2001), The Physical Mechanism of Transition in Bluff Body Wakes, *Journal of Fluids and Structures*, Vol. 15, No. 3–4, pp. 607–616, DOI: 10.1006/jf1s.2000.0369.
- Thomson, W. (1880), Vibrations of a Columnar Vortex, *Proceedings of the Royal Society of Edinburgh*, Vol. 10, pp. 443–456, DOI: 10.1017/S0370164600044151.
- Thurman, C., Boyd, D. D., and Lopes, L. V. (2024), Prediction of Broadband Blade-Wake Back-Scatter Noise from a Hovering Ideally Twisted Rotor Using OVERFLOW2-ANOPP2, AIAA SCITECH 2024 Forum, Orlando, FL, USA, DOI: 10.2514/6.2024-2471.
- Tsai, R. (1987), A Versatile Camera Calibration Technique for High-Accuracy 3D Machine Vision Metrology Using Off-the-Shelf TV Cameras and Lenses, *IEEE Journal on Robotics and Automation*, Vol. 3, No. 4, pp. 323–344, DOI: 10.1109/JRA.1987.1087109.
- Van der Wall, B. G. and Richard, H. (2006), Analysis Methodology for 3C-PIV Data of Rotary Wing Vortices, *Experiments in Fluids*, Vol. 40, No. 5, pp. 798–812, DOI: 10.1007/s00348-006-0117-x.
- Van Ingen, J. (2008), The eN Method for Transition Prediction. Historical Review of Work at TU Delft, 38th Fluid Dynamics Conference and Exhibit, Seattle, WA, USA, DOI: 10.2514/6.2008-3830.
- Vatistas, G. H., Kozel, V., and Mih, W. C. (1991), A Simpler Model for Concentrated Vortices, *Experiments in Fluids*, Vol. 11, No. 1, pp. 73–76, DOI: 10.1007/BF00198434.

- 
- Vatistas, G. H. (2006), Simple Model for Turbulent Tip Vortices, *Journal of Aircraft*, Vol. 43, No. 5, pp. 1577–1579, doi: 10.2514/1.22477.
- Vatistas, G. H., Panagiotakakos, G. D., and Manikis, F. I. (2015), Extension of the n-Vortex Model to Approximate the Effects of Turbulence, *Journal of Aircraft*, Vol. 52, No. 5, pp. 1721–1725, doi: 10.2514/1.C033238.
- Vollmers, H. (2001), Detection of Vortices and Quantitative Evaluation of Their Main Parameters from Experimental Velocity Data, *Measurement Science and Technology*, Vol. 12, No. 8, pp. 1199–1207, doi: 10.1088/0957-0233/12/8/329.
- Wassermann, P. and Kloker, M. (2002), Mechanisms and Passive Control of Crossflow-Vortex-Induced Transition in a Three-Dimensional Boundary Layer, *Journal of Fluid Mechanics*, Vol. 456, pp. 49–84, doi: 10.1017/S0022112001007418.
- Wassermann, P. and Kloker, M. (2003), Transition Mechanisms Induced by Travelling Crossflow Vortices in a Three-Dimensional Boundary Layer, *Journal of Fluid Mechanics*, Vol. 483, pp. 67–89, doi: 10.1017/S0022112003003884.
- Widnall, S. E. (1972), The Stability of a Helical Vortex Filament, *Journal of Fluid Mechanics*, Vol. 54, No. 4, pp. 641–663, doi: 10.1017/S0022112072000928.
- Wieneke, B. (2005), Stereo-PIV Using Self-Calibration on Particle Images, *Experiments in Fluids*, Vol. 39, No. 2, pp. 267–280, doi: 10.1007/s00348-005-0962-z.
- Wieneke, B. (2015), PIV Uncertainty Quantification from Correlation Statistics, *Measurement Science and Technology*, Vol. 26, No. 7, p. 074002, doi: 10.1088/0957-0233/26/7/074002.
- Willert, C. E. (2006), Assessment of Camera Models for Use in Planar Velocimetry Calibration, *Experiments in Fluids*, Vol. 41, No. 1, pp. 135–143, doi: 10.1007/s00348-006-0165-2.
- Williamson, C. H. K. (1988), The Existence of Two Stages in the Transition to Three-Dimensionality of a Cylinder Wake, *The Physics of Fluids*, Vol. 31, No. 11, pp. 3165–3168, doi: 10.1063/1.866925.
- Williamson, C. H. K. (1996), Three-Dimensional Wake Transition, *Journal of Fluid Mechanics*, Vol. 328, pp. 345–407, doi: 10.1017/S0022112096008750.
- Wolf, C. C., Braukmann, J. N., Stauber, W., Schwermer, T., and Raffel, M. (2019a), The Tip Vortex System of a Four-Bladed Rotor in Dynamic Stall Conditions, *Journal of the American Helicopter Society*, Vol. 64, No. 2, pp. 1–14, doi: 10.4050/JAHS.64.022005.
- Wolf, C. C., Weiss, A., Schwarz, C., Braukmann, J., Koch, S., and Raffel, M. (2022), Wake Unsteadiness and Tip Vortex System of Full-Scale Helicopters in Ground Effect, *Journal of the American Helicopter Society*, Vol. 67, No. 1, pp. 1–17, doi: 10.4050/JAHS.67.012010.
- Wolf, C. C. et al. (2019b), Experimental Study of Secondary Vortex Structures in a Rotor Wake, *Experiments in Fluids*, Vol. 60, No. 11, p. 175, doi: 10.1007/s00348-019-2807-1.
- Wolf, C. C. (2014), The Subsonic Near Wake of Bluff Bodies, PhD thesis, RWTH Aachen.
- Zhou, J., Adrian, R. J., Balachandrar, S., and Kendall, T. M. (1999), Mechanisms for Generating Coherent Packets of Hairpin Vortices in Channel Flow, *Journal of Fluid Mechanics*, Vol. 387, pp. 353–396, doi: 10.1017/S002211209900467X.



# Curriculum Vitae

Alexander Heintz,  
born on 13<sup>th</sup> of August 1995 in Minden

## Work Experience

- since 04/2022      **German Aerospace Center (DLR), Göttingen**  
Ph.D. Candidate: Institute of Aerodynamics and Flow Technology  
Topic: *Experimental Parameter Study on Primary and Secondary Vortices in the Wake of a Hovering Rotor*
- 01/2022 – 04/2022      **Technical University of Braunschweig**  
Research Assistant: Institute of Fluid Mechanics
- 01/2021 – 12/2021      **Technical University of Braunschweig**  
Master Thesis: Institute of Fluid Mechanics  
Topic: *Influence of Steps on the Stability of Laminar Boundary Layers*
- 04/2020 – 11/2020      **German Aerospace Center (DLR), Göttingen**  
Student Research Project: Institute of Aeroelasticity  
Topic: *Influence of the Induced Velocity Field on Propeller-Whirl-Flutter*

## Education

- 10/2018 – 01/2022      **Technical University of Braunschweig**  
Master: Aerospace Engineering (with honors)
- 10/2014 – 09/2018      **Technical University of Braunschweig**  
Bachelor: Mechanical Engineering

## Awards

- 2024      **Vertical Flight Society**  
Heinrich Focke Scholarship of the Vertical Flight Foundation
- 2016      **Nomination LehrLeo Awards**  
Category: Best Undergraduate Teaching at TU Braunschweig, as a part of the technical mechanics teaching team (student tutor)